MODELING AND CHARACTERIZATION

OF RF MEMS RESONATORS

by

NAJLA S. KHAN

Presented to the Faculty of the Graduate School of

The University of Texas at Arlington in Partial Fulfillment

of the Requirements

for the Degree of

MASTER OF SCIENCE IN ELECTERICAL ENGINEERING

THE UNIVERSITY OF TEXAS AT ARLINGTON

August 2009

Dedicated to

In memory of my late father Dr. Solaiman Khan

ACKNOWLEDGEMENTS

ABSTRACT

MODELING AND CHARACTERIZATION

OF RF MEMS RESONATORS

Najla Khan, M.S.

The University of Texas at Arlington, 2009

Supervising Professor: Dr. Donald Butler

Over the past decade, a multitude of micro-electro-mechanical (MEMS) devices have been developed and commercialized due to their low power consumption, reduced cost and compact size. In recent years, significant advancements in technology have extended MEMS development towards radio frequency, microwave and millimeter wave applications.

The need for micro-machining and MEMS based systems for RF and microwave applications arises from the inherent limitations of existing RF devices. Motivation for incorporating MEMS based fabrication technologies into microwave and millimeter wave systems can be classified into three main categories: precision, system integration and performance. As frequency increases, the size of RF components decreases. [1] For this reason, it is crucial that the dimensions of the RF components remain in the sub-millimeter range, necessitating high precision fabrication techniques. Such precision is only achievable through the micro-machining methodology. For a complete useful RF application, these components also need to operate properly when integrated with other analog functions such as filters, oscillators or mixers. The micro-machined RF components are fully compatible with complete system integration. Finally, the performance of these devices is also notable. Due to their capability of achieving a high quality factor or Q, reducing insertion loss and increasing

v

bandwidth, RF MEMS devices have gained largely popularity in recent years. Such devices, especially resonators, can also be fabricated to achieve very high Q (in the tens of thousands range) for frequencies up to and beyond 10 MHz. [2]

A key limitation in commercializing RF MEMS devices, such as resonators, is the reliability factor. Reliability requirements of different MEMS devices are specific and unique to the type and purpose of their application. Understanding the reliability of RF devices stems primarily from the knowledge of their failure behavior and mechanisms, which are: stiction, delamination, dampening and mechanical failure over a long period of time. [2] Unfortunately, at the time of this writing, there has not been enough research and development to fully understand these reliability issues.

This research focuses on some of the factors of mechanical failure by investigating the effect of the changes in the elastic properties on the resonant and damping characteristics of the resonator beam. In an attempt to eliminate this mechanical failure, both the linear and non-linear behavior of RF MEMS resonators are investigated and a strategy is developed to improve the performance through both modeling and understanding the complete dynamics of RF MEMS devices. The complete resonator dynamics is investigated with the aid of the Agilent Advanced Systems (ADS) and MathCAD software packages. Furthermore, an amplifier circuit is designed which is integrated with the resonator model via wire bond and then characterized using an Agilent E5071C Series Network Analyzer. This improves the Q-factor (between 100 and 150) and the S_{21} parameter (between 10 dB and 25 dB) of the resonator significantly. Without the amplifier circuit, Q-factor is found to be between 10 and 50 and S_{21} between -40 and -60 dB. Thus, this model is an innovative method of reducing undesired insertion loss, thereby, improving the performance of the resonator model.

TABLE OF CONTENTS

LIST OF ILLUSTRATIONS

x

xi

LIST OF TABLES

xiii

CHAPTER 1

INTRODUCTION

<u>1.1 Micro-Electro-Mechanical Systems (MEMS)</u>

Micro-Electro-Mechanical Systems or MEMS refer to a family of microsensors, actuators, mechanical and electronic components integrated together by virtue of microfabrication. The MEMS devices can both sense and react to changes in their environment via microcircuit control. In recent years, micro power supply, micro relay, micro signal processing units and antennas have also been integrated into the MEMS structures in order to achieve the required sensing and actuating operations. Micro components fabricated using MEMS technology make the system faster, more reliable, cheaper and capable of incorporating more complex functions. [2]

In the early 1990s, MEMS emerged with the development of the integrated circuit (IC) fabrication processes, where sensors, actuators and control functions were co-fabricated using silicon. Since then, MEMS technology has undergone remarkable research progress, funded by both public and private sectors. There has been some notable commercialization of MEMS devices such as micro accelerometers, inkjet printer heads, and micro-mirrors for projection, which do not involve a heavy amount of integrated circuitry for operation. However, these concepts can be easily extended to more complex integrated MEMS devices in a variety of fields including: micro-fluidics, aerospace, biomedicine, chemical analysis, wireless communications, data storage, displays, and optics. [2] [3] [4]

MEMS technology in telecommunications holds great potentials for commercialization. In order to materialize this, thorough research, modeling and testing must be conducted to ensure that the reliability of such devices approaches 99.9% before introducing them commercially.

1

<u>1.2 Radio Frequency MEMS Devices</u>

The radio frequency range lies approximately between 300 MHz and 3.0 GHz. [5] Most of present day wireless communication occurs within this range of radio frequencies. There has been a lot of success in the newer generation Radio frequency (RF) MEMS devices owing to the recent development of microfabrication techniques. The two approaches to silicon-based RF MEMS fabrication are bulk micromachining and surface micromachining. In addition to silicon-based techniques, polymer-based RF MEMS techniques have also been proposed.

One of the earliest implementations of MEMS technology for microwave applications was in the area of surface micromachined actuators for the realization of microwave switches with very high linearity, low DC standby power and low insertion loss. [2] [6] RF MEMS have also been applied to microinductors and variable capacitors, as a replacement for varactor diodes for tuning. [2] [7] Micromachined capacitors have proven to be very compatible with the rest of the circuit, allowing for a complete integrated system. In many communication systems and radars, high Q filters (which use micromachined capacitors and inductors) have been widely employed. These filters can be used for frequencies up to tens of MHz, and can have Q values in the thousands with proper packaging. However, fabrication limitations restrict the extension of micromechanical filters for frequencies above 100 MHz. SAW filters and resonators can bridge this gap and provide high Q devices for frequencies up to 2 GHz. In recent years, there have been developments of innovative micromachined antennas for improving the performance of microstrip transmission lines and phase shifters using the nonlinear dielectric properties of ferroelectric materials such as barium strontium titanate. [2]

Micromachining has proved very useful at higher frequencies where horns and other antennas become so small that fabrication by conventional means is unrealizable. [2] As a result, integration and packaging are vital for any MEMS component. Few RF MEMS devices have reached maturity owing to the fact that the packaging of these devices has not proved to

be 100% reliable in keeping the electronic circuitry functional for long periods of time without being contaminated by the environmental surroundings.

1.3 Radio Frequency MEMS Resonators

Radio frequency (RF) resonators are usually used in analog systems including: filters, mixers, oscillators and duplexers. [1] Due to the fact that mechanical resonators have a much higher quality factor Q than their other electrical counterparts, they have become very important components in communication circuits. MEMS silicon resonators can be a potential alternative to quartz crystals as accurate timing devices in oscillators for modern data and communication applications. RF MEMS resonators have a very small compact size, are compatible with integrated circuits and are very cost effective. The size of integrated MEMS resonators reduces with increasing frequency. However, as the resonators decrease in size, non-linear behavior is exhibited, which needs to be fully analyzed and understood before it can be made useful in applications. [8] [9]The nonlinearities depend on the specific structure and layout of resonators. Such nonlinearities affect the performance of oscillators considerably and hence must be considered for optimal resonator design. For this purpose, it is very important to model the dynamics of the resonator numerically as well as experimentally in order to understand its complete response to frequency and other key parameters. [8]

This thesis investigates both the linear and non-linear behavior of RF MEMS resonators and attempts to improve the performance of these resonators by way of external amplifier circuitry.

Individual contribution to this effort can be summarized as follows:

- Investigation of linear and non-linear behavior of RF MEMS resonators.

- Enhancement of the accuracy of the resonator model by including higher order terms in the stiffness factor and re-deriving the complete model of RF MEMS resonator.

- Design of a MMG30XX amplifier circuit to improve the S_{21} and Q-factor of RF

3

MEMS resonators.

- Characterization of the RF MEMS resonators integrated with the MMG30XX amplifier circuit.

CHAPTER 2

RF MEMS RESONATORS

2.1 Introduction

RF MEMS technology poses a significant potential in the wireless paradigm owing to its versatility in integrating both the electronic (2-D) and the micromechanical (3-D) devices. The RF MEMS devices have a much lower power consumption and wider bandwidth than other RF devices. They can be fabricated in three ways - surface micromachining, bulk micromachining, and LIGA fabrication techniques. [2] [10] [11] [12] The parasitic effects in RF devices, which limit their performance, can be eliminated using MEMS techniques. [13] [14]The high quality factors found in RF devices are worth mentioning. Recent studies have shown that the bulk-etched 1nH inductors exhibited Q's between 6 and 28 at frequencies between 6 and 18 GHz and surface micromachined 2.3-nH inductors exhibited Qs of about 25 at 8.4 GHz. Surface micromachined 2.05-pF varactors exhibited Q's of about 20 at 1 GHz, for a capacitance tuning range of1.5:1 over a 0 to 4V tuning voltage at a self-resonance frequency of 5 GHz. MEMS switches have been shown to have a series resistance less than 1 Ohm, insertion loss less than 0.1 dB at 1 GHz, isolation greater than 40 dB at 1 GHz, third-order intercept point (IP3) greater than +66 dBm, actuation voltage between 3 and 30V, and control current less than 10 uA. Micromachined cavity resonators have shown Qs of 500 at 10 GHz, only 3.8% lower than the unloaded Q obtained from a rectangular cavity of identical dimensions. Microelectromechanical resonators, on their part, have exhibited Qs of 7,450 at 92.5 MHz, while film bulk acoustic resonators (FBARs) have exhibited Qs of over 1,000 at resonance frequencies between 1.5 and 7.5 GHz. The bulk etching technique significantly eliminates the parasitics of transmission lines and improves their performance significantly. In fact, insertion loss improvements of 7 dB at 7 GHz

5

and 20 dB at 20 GHz have been achieved.The Agilent 1,900-MHz FBAR duplexer for Personal Communications Services (PCS) handsets shows a size 5X reduction with respect to its ceramic counterpart at comparable performance. Although the potentials of RF MEMS devices in wireless applications are vast, research is still ongoing to ensure 100 % reliability in performance before they can be widely commercialized. For this purpose, it is vital to develop new models and circuit/system level methodologies in order to test its reliability and cost effectiveness with respect to packaging. [13] [14]

In wireless applications, low power consumption, wide bandwidth, RF component parasitics, fabrication and packaging costs all play a vital role in determining the performance of the devices being commercially utilized. In light of this observation, MEMS was presented as a powerful technology capable of enabling devices to overcome these limitations.

2.2 Brief History of RF MEMS Resonators

Over the past decade, several new fabrication techniques have been developed which significantly made micromechanical systems (MEMS) popular in diverse areas of engineering and science, notably in the microwave and millimeter wave systems. MEMS technology for microwave applications has high potentials of solving some of the most challenging problems of high-frequency technology for wireless communications. Recent developments and needs in the wireless paradigm have made it crucial for devices to be as small and efficient as possible. The drastic need in the reduction in the workable surface area of integrated devices can be realized only by the development of radio frequency (RF) MEMS. [13]

The term RF MEMS refers to the design and fabrication of MEMS for RF integrated circuits. These are quite different from the traditional MEMS devices operating at RF frequencies. RF MEMS devices are used mostly for actuation or adjustment of separate RF devices or components, such as variable capacitors, switches, and filters. Traditional MEMS can be divided into two classes: MEMS actuators and MEMS sensors. Some MEMS devices including the micro sensors, which were the earliest Microsystems due to their ease of

6

fabrication, have widespread applications. Actuators, on the other hand, did not generate adequate energy to be used in the associated systems. However, through RF and microwave systems, this generated energy is sufficient to impact the characteristics of the systems as a whole. [2]

RF MEMS devices can be either passive or active. Passive devices include bulk micromachined transmission lines, filters and couplers, whereas, the active MEMS devices include switches, tuners and variable capacitors. The structures on the wafer surface are developed making use of the electromotive force present in the circuitry. This is how electrostatic attraction, although magnetic, thermal or even gas-based microactuator structures have been developed. [2]

Following the classical review paper by Brown (1998), the RF MEMS development can be categorized as RF extrinsic, RF intrinsic and RF reactive. In RF extrinsic, the MEMS structure lies outside the RF circuit and actuates or controls other devices in the RF circuit. Examples of such devices are tunable microstrip transmission lines and associated phased shifters and arrays. Owing to the ease of fabrication, the microstrip lines have been very widely used to interconnect high-speed circuits and components. In RF intrinsic, the MEMS structure lies inside the RF circuit and has both the actuation and RF-circuit function. Examples of such devices are electrostatic microswitches and comb-type capacitors. [2] [15] They are also flexible, stable and long lasting and can be integrated with the organic thin film transistor very easily. In RF reactive, the MEMS structure lies inside, where it has an RF function coupled with the attenuation. Examples of such devices are capacitive coupled tunable filters and resonators. Microwave and millimeter wave planar filters on thin dielectric membrane show low loss, and are suitable for low-cost, compact, high-performance mm-wave one-chip integrated circuits. One of the earliest silicon-based RF MEMS devices for microwave applications is in the area of surface micromachined actuators for the realization of microwave switches. These possess very high linearity, low DC standby power and low insertion loss. These switches are based on

electrostatic attraction counterbalanced by suitable mechanical forces on the beam to pull the switch into the right position. This switch can be designed to exhibit about a 50Ω impedance across a broad range of frequencies when closed, and nearly an open circuit when there is no connection. Several new switch architectures like the air-bridge structure have also been developed. [2] [16] This structure used very high capacitance variation to achieve the switching action, which mandates high switching voltage requirements.

MEMS technology for RF applications concentrates mostly around the variable capacitors used as tuners, instead of the counterpart varactor diodes. In this case, using the appropriate fabrication MEMS technique, a lateral or a parallel plate capacitance variation can be made. The capacitance variation in the parallel plate version is over 3 : 1 which is very suitable for wide-band tuning of monolithic voltage-controlled oscillators (VCOs). The low-frequency mechanical resonance of the structure often creates a limitation to their range. [2]

Silicon micromachining has been a key factor for the vast progress of MEMS over the past decade. Silicon has been used to fabricate structures including clamped beams, membranes, cantilevers, grooves, orifices, springs, gears, and suspensions, which enable a variety of sensors to be developed. Bulk micromachining was commonly used for this purpose but has been replaced by surface micromachining because of the potential possibility of integrating the machined device with microelectronics in the latter process. [2] Another fabrication technique called LIGA (a German acronym for Lithographie, Galvanoformung, Abformung) has become very popular in recent years for microwave antennas because of its ability to etch very thick metal structures. [2] [3]

2.3 Key Parameters of RF Circuit Models

The RF MEMS circuits for wireless applications are designed based on the theory of RF and microwave electronics as well as the novelty of RF MEMS devices. The performance of such devices is therefore greatly influenced by the physical and practical aspects related to RF circuit design.

8

2.3.1 Physical Aspects of RF Circuit Design

In most cases, the measured test results vary from the simulation results considerably. Some of the common known causes of such disparity are: [13]

- The high frequency operation creates a complex non-linear behavior of RF components.

- The coupling paths in the circuit layout have not been considered.

- Unwanted energy storage might occur owing to the fact that the ratio of the transverse dimensions of transmission lines to wavelength is large enough not to be negligible.

- The packaging of the circuit itself behaves as an energy storage cavity by absorbing some of the energy propagating through it.

- The DC bias source may cause unwanted leaks into the circuit owing to the fact that it is not properly decoupled from the circuit.

- Impedance mismatch among interconnected circuits causes large voltage standing wave ratios (VSWR) to occur, resulting in inefficient power transfer and undesired ripples in the frequency response.

Some of the above mentioned aspects are discussed further in the next few sections.

2.3.1.1 Skin Effect

Skin effect is one of the most fundamental and dominant physical phenomena arising in the high frequency circuit models at the RF or microwave range. In a conductor adjacent to a propagating field, such as a transmission line or the inside walls of a metallic cavity, the propagating field penetrates through the metal conductor surface to a certain depth before it becomes zero owing to the fact that the resistance of the conductor is actually non zero. [13] [17] The field usually accumulates near the surface, causing unwanted energy dissipation as it propagates near the surface. This depth of penetration is dependent on frequency

In fact, skin depth can be defined as the distance it takes for the field to decay exponentially to e[-1]= 0.368, or 36.8% of its value at the air-conductor interface, and is given by equation (2.1) [13] [17]:

$$\delta = \frac{1}{\sqrt{f\pi\mu\sigma}}$$

(2.1)

where   δ = skin depth

f = the signal frequency,

μ = the permeability of the medium surrounding the conductor, and

σ = the conductivity of the metal making up the conductor.

Therefore, the skin depth is inversely proportional to the square root of the frequency and the conductivity.

Choosing a conductor metal with high conductivity and ensuring that the minimum conductor thickness should at least be equal to, or greater than four skin depths at the lowest frequency of operation can considerably minimize this skin effect. [13]

2.3.1.2 Transmission Line on Thin Substrate

Microstrip line models are accurate only when dealing with microstrip lines of substrates with thickness in the hundreds of microns. When the substrate thickness is just a few microns, these conventional models fail. Several models have been developed to address this issue. The two most commonly used models are the thin film microstrip line model and the coplanar waveguide line model. [13] [18] [19]

2.3.1.2.1 Thin-Film Microstrip Line Model

The development of silicon RF ICs has invoked the need for thin-film microstrip lines. However, in this case, the loss properties of the line are decoupled from those of the silicon wafer, circumventing its poor microwave properties. In order to address this issue and derive a better thin film microstrip model, Schneider and Heinrich have developed a theory based on quasi-

10

TEM approximations owing to the small dimensions relative to wavelength of these lines. Figure 2.1 shows the cross sectional views of conventional, thiin-film microstrip lines and the equivalent distributed circuit model.
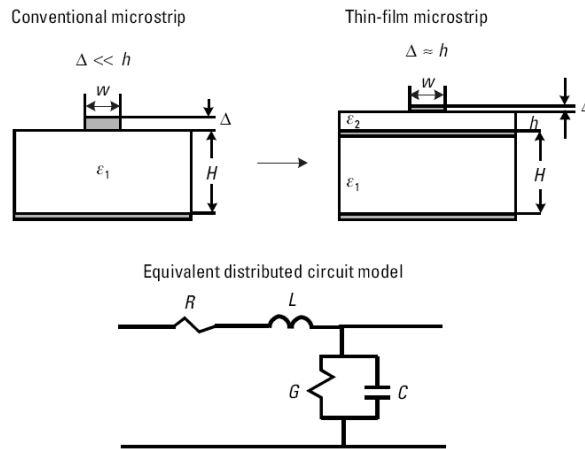
Figure 2.1 The cross sections of conventional and thin-film microstrip lines and the equivalent distributed circuit model. [13]

The microstrip line is analyzed as if it were suspended in air (i.e., as a TEM line), and then the effect of the substrate is taken into account by adjusting the air-filled-derived values of the propagation constant and characteristic impedance by an effective dielectric constant obtained by performing a static analysis. [13] [19] [20]

2.3.1.2.2 Coplanar Waveguide Line Model

The coplanar waveguide (CPW) transmission line has been used widely in the development of RF MEMS. [13] [21] [22] In this model, both series and parallel (shunt) active and passive components, as well as high circuit density have been considered. In addition, the width of its traces can be extended to enable matching component lead widths without changing the characteristic impedance. [13] [18] [23] Figure 2.2 shows a typical coplanar waveguide line model.

11
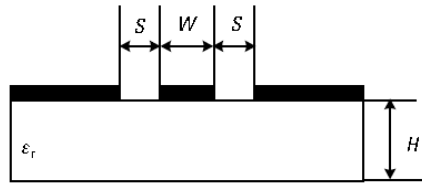
Figure 2.2 The CPW transmission line configuration. [13]

2.3.1.3 Self Resonant Frequency

In the presence of an ac field, an isolated metallic conductor exhibits surface resistance and internal inductance associated with the skin effect. The complete model of the isolated conductor includes both the dc resistance and the external inductance. This causes undesired parasitic effects in high frequencies beyond the resonant frequency. Usually, a capacitance is connected in series with the conductor to compensate for these effects. However, at sufficiently high frequencies, the inductive reactance of the conductor may reach values that can compensate and overcome the capacitive reactance, resulting in a combination of inductive and the capacitive behavior. This can cause adverse effects, especially in broadband matching network applications. [13]

2.3.1.4 Quality Factor

Radio frequency and microwave circuits process information-carrying signals characterized by an incoming power level and a frequency spectrum. However, when the signal passes through a passive circuit, such as an impedance matching network, or a bandpass filter, undesired power loss occurs due to its reactive elements. This is where the quality factor comes into the picture because it characterizes this power loss. The quality factor Q, defined as [13] [24]:

$$Q = 2\pi \times \frac{\text{maximum instantaneous energy stored in the circuit}}{\text{energy dissipated per cycle}}$$

(2.2)

In practice, the concept of Q is employed to characterize both resonant, or tuned circuits, and individual components. In the case of tuned circuits, such as a series RLC network, Q can be defined as [13] [24]:

12

$$Q_{\text{Tuned Circuit}} = \frac{f_0}{B}$$

(2.3)

where f_0 is the resonance frequency and B is the bandwidth of the circuit.

In the case of single elements, the Q is obtained by forming a resonant circuit with an ideal lossless reactance at the frequency in equation [17]. Therefore, the Q of a capacitor with a shunt parasitic conductance G representing its losses, would be that of a tuned circuit using that capacitor and parallel conductance, with an ideal lossless inductor connected in parallel. [13] [25] It is defined by [13]:

$$Q_{\text{Capacitor}} = \frac{\omega_0 C}{G}$$

(2.4)

Similarly, for an inductor with series parasitic resistance R, Q is given by equation (2.5) [13]

$$Q_{\text{Inductor}} = \frac{\omega_0 L}{R}$$

(2.5)

In passive components, the quality factor is used to characterize the signal power loss in the component. Thus, in the context of matching networks or filters, for example, the higher the Q of the constituent passive elements, the lower the insertion loss of the circuit. [13]

2.3.1.5 S-Parameters

S-parameters (scattering parameters) define the complete small signal characteristics of a device excluding the noise. It is based on the relationship between incoming (incident) and outgoing (reflected) waves, typically in a 2-port network terminated with 50Ω matching impedances. [26] The four S-parameters in a 2-port network are defined as follows [26]:

- *Input Reflection Coefficient*: S_{11} = Ratio of reflected power to incoming power at port 1.

- *Forward Transmission Coefficient*: S_{21} = Ratio of outgoing power at port 2 to incoming power at port 1.

13

- *Reverse Transmission Coefficient*: S_{12} = Ratio of outgoing power at port1 to incoming power at port 2.

- *Output Reflection Coefficient*: S_{22} = Ratio of reflected power to incoming power at port 2.

Port 2 is not fed with any power and is terminated with the characteristic impedance Z_0, typically 50Ω. In many cases such as in transistors, a third port is used as the common ground while the 2-ports are applied. [26]

S_{21} provides an idea of the gain of the device directed from input to output. Typically, matched devices provide $|S_{21}| > 1$ and passive devices provide $|S_{21}| < 1$

S_{12} represents how much energy is transferred from device output back to input.

S_{11} represents how much energy is reflected at the input.

S_{22} represents how much energy is reflected at the output. [26]

The *Rollet's* criterion for stability shows the relationship between S-parameters and stability as shown below [5] [26] [27]:

$$\Delta := S_{11} \cdot S_{22} - S_{12} \cdot S_{21} \tag{2.6}$$

$$k := \frac{1 - \left(|S_{11}|\right)^2 - \left(|S_{22}|\right)^2 + \left(|\Delta|\right)^2}{2\,|S_{12} \cdot S_{21}|} \tag{2.7}$$

where, k >1 and Δ <1 for unconditional stability. [5] [26]

2.3.1.6 Moding (Packaging)

The proper operation of RF and microwave circuits and systems is critically dependent upon the clean environment provided by their containing package. [13] [14] [28] [29] In fact, packaging is considered an enabler for the commercialization of MEMS for at least three reasons. [13]

- Due to the sensitive nature of their moving structures, MEMS must be protected against

extraneous environmental influences, such as various forms of air contamination and moisture. [13]

- Due to their small size, it is vital that the devices are protected to withstand handling as they are integrated with other systems. [13]

- Since by their very nature RF and microwave circuits and systems are susceptible to EM coupling and moding, they must be electrically isolated. [13]

Moding or packaging refers to the resonant cavity-like behavior of metal structures (Figure 2.3) enclosing high-frequency circuits, which can trap the energy being processed by these and thus contribute an effective transmission loss extrinsic to the circuit.
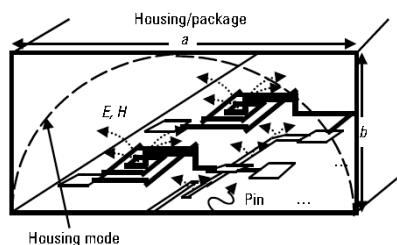
Figure 2.3 The electromagnetic environment of packaged high-frequency circuit. [13]

There has been ongoing research related to the resonant mode suppression/damping. Some of the noteworthy solutions to this issue have been proposed by Williams [13] [18], who suggested fixing a dielectric substrate coated with a resistive film to the upper wall of the package cavity, and Mezzanotte et al. [13] [29], who suggested placing damping/absorbing layers, not only on the upper wall, but also on the side walls. [13]

2.3.2 Practical Aspects of RF Circuit Design

2.3.2.1 DC Biasing

DC biasing refers to setting the active components at their appropriate dc operating point by introducing a dc power source in the circuit, without inhibiting the performance. A voltage source usually shows some finite impedance at the output when ideally it should exhibit an output impedance of zero. So, it must be ensured that at the frequency of operation, the voltage source node appear as a short circuit. To avoid this, proper biasing of the circuit is

15

required.   Capacitor decoupling is usually used for such proper biasing.   This involves connecting as many capacitors as necessary in parallel with the dc supply node, such that low output impedance is ensured throughout the required frequency bandwidth. [13]

2.3.2.2 Inductor Decoupling Effect

The effect of the inductive components of RF circuit should also be considered. The fact that the windings in inductors are adjacent to each other poses a major issue at RF frequencies or higher. A slight voltage drop across these adjacent turns gives rise to parasitic distributed capacitance. The combination of the parasitic shunt capacitance C_s and the series resistance R_s represent the composite effects of distributed capacitance C_d and resistance R_d in the inductor coil. The equivalent circuit of the inductor is shown in Figure 2.4
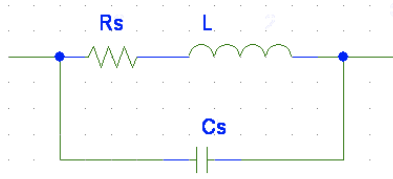
Figure 2.4 The equivalent circuit of inductor.

The reactance of the inductors is affected by the presence of the distributed capacitance C_d. As the frequency increases beyond the self-resonant frequency of the circuit, the distributed capacitance becomes very dominant. The inductor reactance starts decreasing and finally a phase shift of 90 degrees occurs in the voltage and the inductor starts behaving like a capacitor.

Inductors have been fabricated using square, octagonal and circular spirals and their performance investigated. In many cases, it was found that the circular or octagonal spirals exhibit about 10% lower resistance than the square spiral inductor for the same inductance. Research is still in progress to develop micromachined inductors with very high Q and better performance at high frequencies. [5] [26] [30]

16

2.3.2.3 Impedance Mismatch Effects

RF and microwave systems comprise of a cascade or chain connection of building blocks, with each building block performing a signal processing function. As the signal being processed propagates down the chain and reaches the input of the next building block, it is important that there is no loss of information and has minimum reflection. Thus, the input and output reflection coefficients are usually specified in the system design. The input and output reflection coefficients are expressed in terms of return loss or voltage standing wave ratio (VSWR), which is the ratio between maximum (V_{max}) and minimum (V_{min}) voltage amplitudes in the interconnecting transmission line. VSWR is given by the set of equations given in 2.8 [13] [31]:

$$\rho = \frac{Z_0 - Z_L}{Z_0 + Z_L}$$

$$\text{Return loss}(\text{dB}) = -20 \times \log|\rho|$$

$$VSWR = \frac{V_{max}}{V_{min}} = \frac{1 + |\rho|}{1 - |\rho|}$$

(2.8)

This return loss of a building block is desired to be as large as possible so that the signal power is transferred completely with minimum reflections. Large return loss implies a low input reflection coefficient. Reflections, if not moderated properly, can lead to destructive interference with a new incoming signal, thus artificially modulating the input signal to subsequent building blocks, resulting in amplitude ripples at their output. A large reflection coefficient also implies a large ratio of maximum to minimum voltage, which in turn, may imply a large maximum voltage amplitude. In the context of RF MEMS, inadvertently large voltage amplitudes may be undesirable in order to limit the phenomenon of hot switching. In this phenomenon, a force bias may be generated on an electrostatically actuated system due to the applied ac voltage being

17

mechanically rectified to the point of inducing a bias force (voltage) greater than the pull-in force (voltage). [13]

<u>2.4 Types of RF MEMS Devices</u>

Some of the common RF MEMS devices used mostly for the communications applications are high-Q vibrating resonators, High-Q tunable capacitors, medium-Q inductors and switches.

2.4.1 High-Q Vibrating Micromechanical Resonators

Vibrating micromechanical resonators can achieve very high Q's in the tens of thousands with frequencies in the UHF range. The three most common MEMS resonators used in wireless communications are clamped-clamped [13] [32] (Figure 2.5), free-free [13] [33] and contour-mode disc resonators.[13] [34]
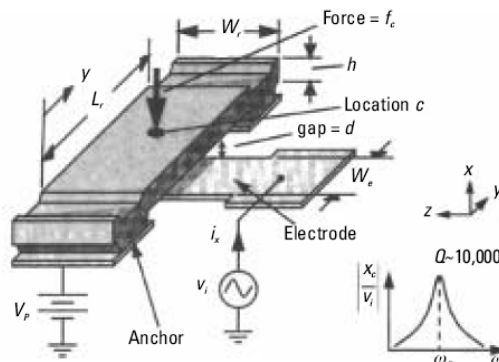
Figure 2.5 The perspective schematic view of a clamped-clamped beam MEMS resonator under a typical bias and excitation configuration. [13] [35]

The clamped-clamped resonators can operate with frequencies around 8 MHz and attain large stiffness-to-mass ratios. This is very important in communication applications because large stiffness enables large dynamic range and power handling. [13] [34] However, these kinds of resonators have considerable anchor losses due to the energy dissipation to the substrate through the anchor, limiting the achievable Q at higher UHF frequencies. Using the free-free resonator, which works in frequencies up to 92 MHz, can significantly reduce this anchor loss. In this free-free resonator structure, the beam is suspended via four torsional

beams, each of which is anchored to the substrate with rigid contact anchors. The beams are a quarter-wavelength long, which causes high acoustic impedance at their point of attachment to the resonator beam. As a result, very little acoustic energy can propagate through the support beams to the anchors/substrate, attributing to the higher Q (about 1 order higher than clamped-clamped resonators). [13] [34]

However, beyond the 92 MHz frequencies, both the free-free and the clamped-clamped resonators drastically reduce in their dimensions. These very small sizes cause a lot of inconsistent, non-linear behavior, which is unfavorable in wireless communications. The contour-mode disk resonators, on the other hand, can work with frequencies up to 156 MHz and attain a Q of 9,400 at relatively large dimensions, were proposed as a means of achieving high frequencies at relatively large dimensions. [13] [34]

2.4.2 High-Q Tunable Capacitors

Tunable micromechanical capacitors (Figure 2.6) consist of metal plates that can be electrostatically moved with respect to one another, which allows voltage control of the capacitance between the two plates. These capacitors can achieve a Q value as high as 300. Integrating these MEMS capacitors with medium-Q inductors can enhance the performance of low noise VCOs considerably. In fact, if the inductors used in conjunction with these capacitors can be made to attain a high Q value of 300, they can be used in tunable RF preselect filters, which would significantly minimize the complexity of multi-band transceivers. [2] [36] [37]
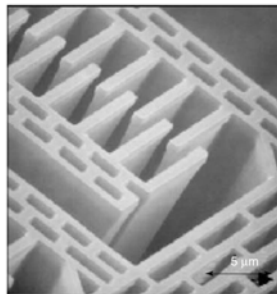
Figure 2.6 The scanning electron micrograph image of a tunable capacitor. [2] [38]

19

2.4.3 Medium-Q Micromechanical Inductors

Inductors with Q > 20 (Figure 2.7) are mostly used in conjunction with high-Q MEMS capacitors in communication circuits. However, the parasitic series resistance and substrate losses in inductors, restricts the Q to be about 7. MEMS inductors, on the other hand, can attain Q's as high as 30 at 1 GHz. Using the MEMS technologies, the metal turns in the inductors can be made thicker, reducing the series resistance. This also increases the gap between the substrate and the inductor, reducing substrate losses. MEMS inductors with Q of 30, when integrated with high-Q MEMS capacitors are adequate to implement low noise VCOs exhibiting considerably low power consumption. [2] [36] [37] [38]
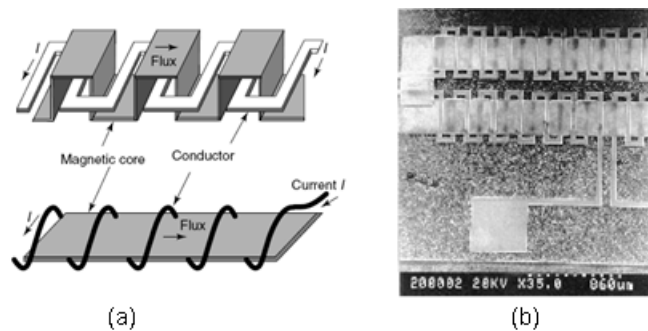
Figure 2.7 Typical micromachined multi-level meander inductor. (a) The schematic diagram [2] [39], and (b) the scanning electron micrograph [2] [40] of the fabricated toroidal-meander inductor.

2.4.4 Micromechanical Switches

Micromechanical switches (Figure 2.8) have the same structure as clamped-clamped beam resonators but they operate in a binary manner. When the beam is up, the switch is open and the beam is pulled down using electrostatic force; subsequently the switch is closed. Because of their metal construction, MEMS switches can attain very high Qs and have low insertion losses. Their behavior is more consistent and linear than their FET counterparts. They can be widely used in antenna switching, switchable filters and phase array antenna applications, provided their reliability can be further improved. [2] [36] [41]

20
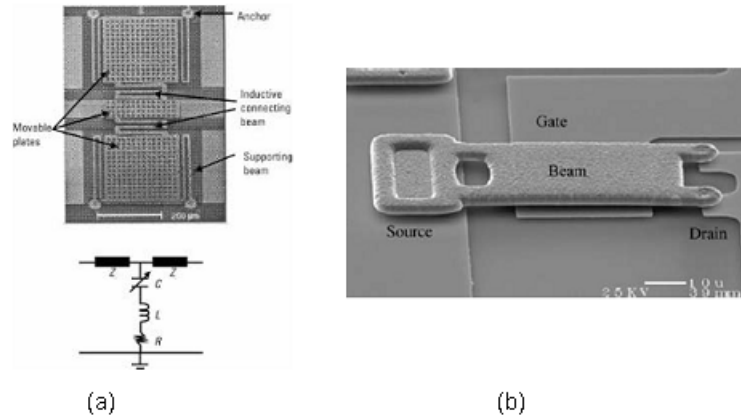
Figure 2.8 Examples of MEMS switches. (a) The resonant MEMS switch [13] [42], and
(b) the scanning electron microscope photograph of a MEMS switch,
showing the source, gate and drain concept. [13] [43]
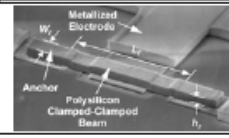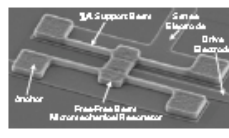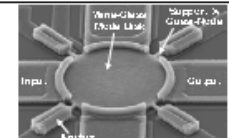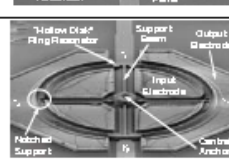
2.5 Motivation of RF MEMS Resonators

Currently, RF resonators are built using expensive and large discrete on-chip integrated or CMOS components. The on-chip integrated parts have low-Q LC circuits and are rather expensive owing to the large surface area needed for the integration. Another inherent disadvantage of the CMOS circuit is their low Q value and rather high power consumption. Integrated MEMS resonators are extremely favorable in such RF circuitry because they not only have high Q values and low power consumption but their size actually reduces with increasing frequency! [1] These MEMS resonators can also be scaled to vibrate over a very wide frequency range from 1 KHz to over 1 GHz, making them very ideal for highly stable oscillator and low loss filtering functions of common transceiver frequencies. [36]

Table 2.1 shows the comparison of vibrating RF MEMS devices for various wireless applications. The clamped-clamped beam resonators can theoretically achieve on-chip Q's of about 8000 for oscillators and filtering functions in ether HF range. However, depending on the specific structure of such resonators, the anchor losses can limit the achievable Q at higher VHF frequencies, limiting the practical range to be less than100 MHz. However, more balanced

21

structures like free-free beam or contour-mode disk resonators can significantly reduce such anchor losses and can operate well into the GHz spectrum. [36] [44]

Table 2.1 The comparison of RF MEMS devices used for communications. [45]

Device	Photo	Performance	Applications	Research Issues
CC-Beam Resonator [17]		Demo'ed: $Q \sim 8,000$ @ 10MHz (vac) $Q \sim 50$ @ 10MHz (air) $Q \sim 300$ @ 70MHz (anchor diss.) Q drop w/ freq. limits freq. range Series Resistance, $R_x \sim 5\text{-}5,000\Omega$	Reference Oscillator HF-VHF Filter HF-VHF Mixer-Filter (arrays of the above)	power handling thermal/aging stability impedance vacuum packaging
FF-Beam Resonator [6]		Demo'ed: $Q \sim 20,000$ from 10-200 MHz $Q \sim 2,000$ @ 90 MHz (air) No drop in Q with freq. Freq. Range: >1GHz; unlimited w/ scaling and use of higher modes Series Resistance, $R_x \sim 5\text{-}5,000\Omega$	Reference Oscillator HF-UHF Filter HF-UHF Mixer-Filter Ka-Band? (arrays of above)	freq. extension power handling thermal/aging stability impedance vacuum packaging
Wine-Glass Disk Res. [21]		Demo'ed: $Q \sim 156,000$ @ 60 MHz (vac) $Q \sim 8,000$ @ 98 MHz (air) Perimeter support design nulls anchor loss to allow extremely high Q Freq. Range: >1GHz; unlimited w/ scaling Series Resistance, $R_x \sim 5\text{-}5,000\Omega$	Reference Oscillator HF-UHF Filter HF-UHF Mixer-Filter (arrays of the above)	freq. extension power handling thermal/aging stability impedance
Contour-Mode Disk Res. [11]		Demo'ed: $Q \sim 11,555$ @ 1.5 GHz (vac) $Q \sim 10,100$ @ 1.5 GHz (air) Balanced design and material mismatching anchor-disk design nulls anchor loss Freq. Range: >1GHz; unlimited w/ scaling and use of higher modes Series Resistance, $R_x \sim 50\text{-}50,000\Omega$	RF Local Oscillator VHF-S-Band Filter VHF-S-Band Mixler Ka-Band? RF Channel-Select (arrays of above)	thermal/aging stability impedance Xmit power handling
Hollow Disk Ring Res. [12]		Demo'ed: $Q \sim 14,600$ @ 1.2 GHz (vac) $\lambda/4$ support design nulls anchor loss Freq. Range: >1GHz; unlimited w/ scaling and use of higher modes Series Resistance, $R_x \sim 50\text{-}5,000\Omega$	RF Local Oscillator UHF-S-Band Filter UHF-S-Band Mixler Ka-Band? RF Channel-Select (arrays of above)	thermal/aging stability impedance Xmit power handling

RF MEMS circuits can play a significant key role in removing board level packaging requirements that currently restrain the size of communication transceivers. The integration of micromechanical and transistor circuits creates powerful alternative transceiver architectures with substantial performance gains with considerably low cost and power consumption. To commercially implement such architectures, further advancements in device frequency, linearity and manufacturability must be made. [36] This has been a key incentive for recent ongoing research some of which will be discussed in Chapter 3.

CHAPTER 3

CURRENT RELATED WORK ON RF MEMS RESONATORS

3.1 RF MEMS Resonator for CMOS Back-End-Of-line Integration

Several recent studies have been explored in the integration of RF MEMS with CMOS backend process flows, one of the notable ones being stated in article [1]. In this design, the RF MEMS resonator has a fixed-fixed beam using the surface micromachining fabrication technique. The fundamental resonant frequency is given by equation 3.1 [1][46]:

$$f_r = \frac{1}{2\pi}\sqrt{\frac{K_r}{m_r}} = 1.03\sqrt{\frac{E}{\rho}}\frac{h}{L_r^2}$$

(3.1)

where K_r = beam stiffness

m_r = mass of the beam

E = Young's modulus

ρ = beam material density

h = thickness of the beam

L_r = length of the beam

For the fabrication of this resonator, a 6000 Å silicon dioxide (TEOS) isolation layer was first deposited. Then a chromium/platinum thin film is deposited on top of this isolation layer to form the electrode, anchor and metal conductors using standard lift-off processing. Organic Polymethylglutarimide (PMGI) is spin coated over the metallization according to the thickness required for the critical air-gap height (850 - 1000 Å) between the resonator beam and the drive electrode. The beam anchor was defined by patterning vias over the conductors. Using plasma-enhanced chemical vapor deposition (PECVD), the silicon oxynitride (SiON) was deposited on top of the sputtered bilayer alpha titanium nitride (TaN). The SiON was used for its low stress

23

and low temperature property. The beam was then patterned using multi-step dry plasma etch process. In the final step, the fabricated layers undergo hours of oxygen-based plasma ashing to remove the sacrificial PMGI layer. Figure 3.1 shows the scanning electron micrograph (SEM) and the schematic view with different layers of an 11.3 MHz MEMS fixed-fixed resonator of length 24.2 µm. [1] [47] [48]

<p style="text-align:center">(a)   (b)</p>
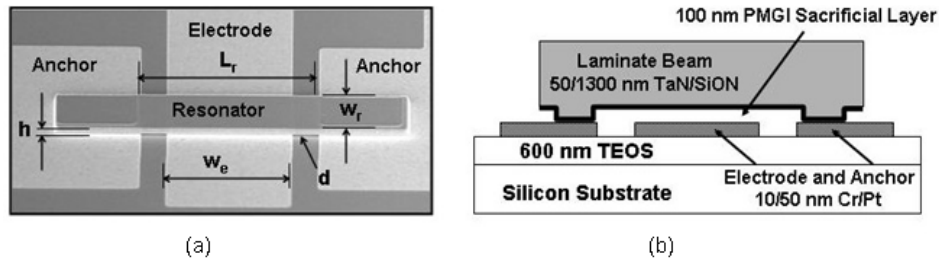
Figure 3.1 The MEMS fixed-fixed resonator. (a) The scanning electron micrograph (SEM) top view of an 11.3 MHz resonator of length 24.2 µm, and (b) the schematic cross section of the resonator with typical process thickness layers indicated. [1]

Once the resonators have been fabricated, the beam breakdown (electrical or mechanical pull down) was measured by performing DC characterizations using an Agilent 4156B SPA. The beam capacitance values were also measured using an Agilent 4284A LCR meter. A vacuum chamber with a base pressure of 10m-Torr was custom-built to perform the RF characterizations. Both input and output RF signals were provided and measured by an Agilent 8753ES Vector Network Analyzer. The RF transmission spectrum (S_{21}) was used to determine resonance frequency and Q of the device. Figure 3.2 shows the RF response (S_{21}) of a MEM resonator of length = 24.2 µm, width = 12.1 µm, and electrode width = 13.8 µm at a vacuum level of 20 mTorr over a range of frequencies. [1]

24
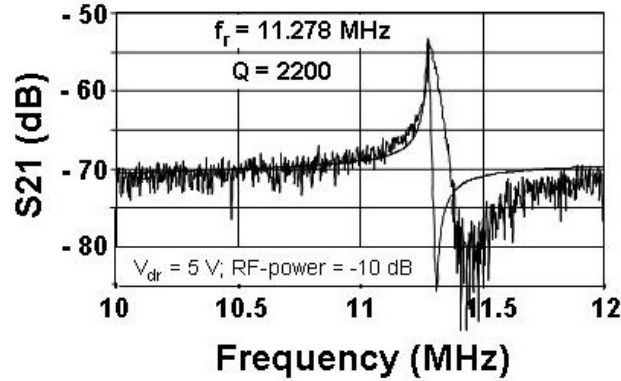
Figure 3.2 The resonant frequency of MEMS resonator of length = 24.2μm, width = 12.1 μm, and electrode width = 13.8 μm measured at 20 mTorr. [1]

A lumped element electrical model of the MEMS resonator based on a force-voltage analogy was also simulated using the Advanced Design System (ADS) software package. The model was represented in terms of series L-C-R components including the circuit parasitic elements (bond pad capacitance C_p and substrate resistance R_p) as shown in Figure 3.3. The formulas represent the relationship between mechanical and electrical elements of the model. The electromechanical coupling coefficient η is dependent on the air gap d between the electrode and the anchor. [1]

$$C_0 = (\varepsilon_0 W_{el} W_r)/d$$
$$C_r = \eta^2/K_r$$
$$L_r = m_r/\eta^2$$
$$R_r = (K_r m_r)^{1/2}/(Q\eta^2)$$
$$\eta = (C_0 V_{dr})/d$$
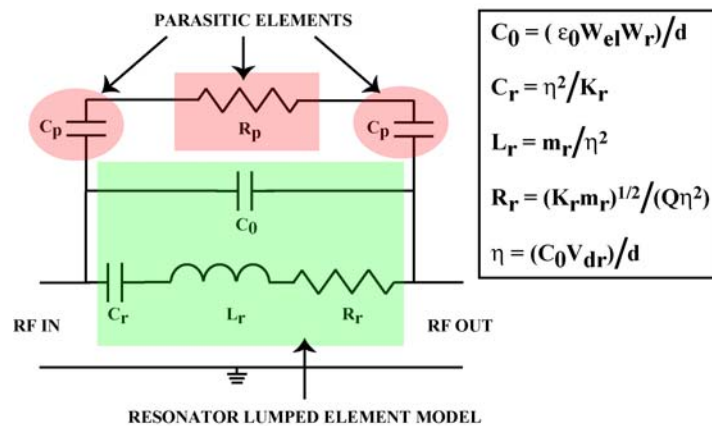
Figure 3.3 The lumped element schematic model of the MEMS resonator. [1]

The resonant frequency, stiffness factor, and the mass of the resonator were given by the set of equations given in 3.2 [1].

25

$$f_r = \frac{1}{2\pi}\sqrt{\frac{K_r}{m_r}}$$

$$K_r = K_m - K_e = 16EW_r(\frac{h}{L_r})^3 - \frac{C_0 V_{dr}^2}{d^2}$$

$$m_r = 0.38\rho h L_r W_r$$

$$(3.2)$$

The simulations and the characterizations showed that the frequency decreases with increasing

drive voltage (V_{dr}) representing the "spring softening" of the device [1] as shown in Figure 3.4.
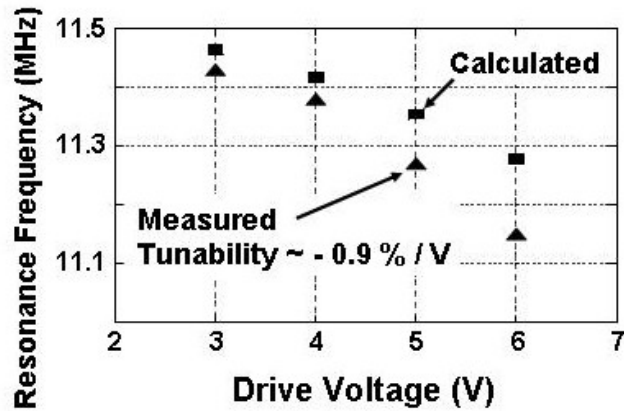
Figure 3.4 The spring softening effect. The change of resonant frequency with varying bias voltage. [1]

This paper demonstrated an RF MEM fixed-fixed beam resonator model compatible with the low temperature CMOS back-end process, using a surface micromachining technique in a cost effective manner.

3.2 Modeling the Dynamics of a MEMS Resonator

Nonlinearities found in MEMS silicon resonators have also been widely studied in recent years to understand the resonator response more accurately. One such case study is described in article [8]. In order to ensure that the resonators have enough stored energy for a considerably large signal to noise ratio, the resonators are driven very close to non-linear regimes. [8] [9] The non-linear behavior is very dominant as the size of the resonators decrease. The presence of the nonlinearities is relevant for oscillator performance and is vital in

26

optimizing resonator designs in the future. In order to determine the influence of resonator nonlinearities on the performance of oscillators, the dynamic behavior of resonators has to be understood. For this purpose, a heuristic approach for modeling the dynamics in a clamped–clamped beam resonator was proposed. [8] [49] Figure 3.5 shows characteristic vibration and actuation model of a clamped–clamped beam resonator. These kinds of resonators are often known as flexural resonators owing to their characteristic out-of-plane vibrations. [8]

(a)

(b)
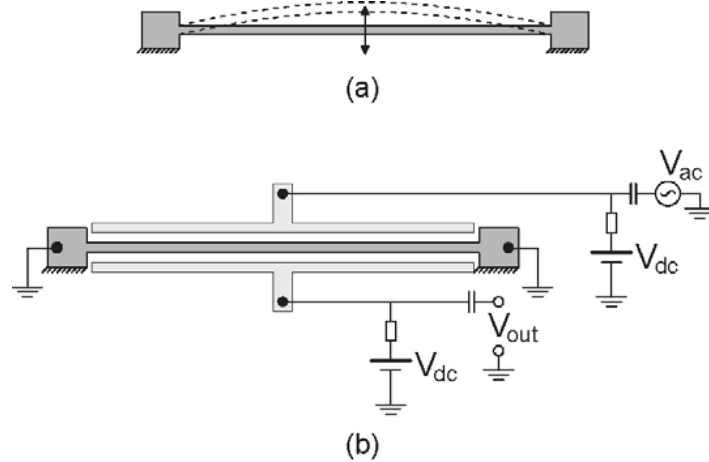
Figure 3.5 The schematic layout of a clamped–clamped beam resonator. (a) The characteristic shape of the vibrating beam and (b) the actuation of the beam using dc and ac voltage sources. [8]

In this paper, the resonators are fabricated using silicon-on-insulator (SOI) wafers. The fabrication process flow is shown in Figure 3.6.

(a)   (b)

(c)   (d)
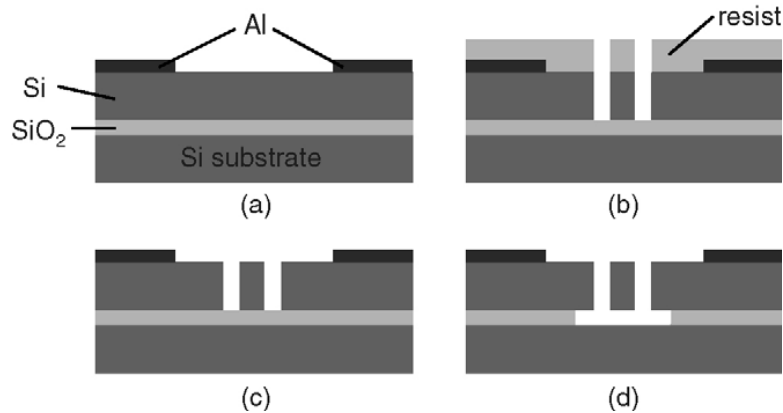
Figure 3.6 The fabrication process flow of the resonator. (a) The Al bond pads defined, (b) the DRIE of top Si layer, (c) the removal of the resist, and (d) the HF wet etching of SiO_2. [8]

27

Initially, the aluminum bond pads are defined on the wafer surface. Next, a layer of photo resist is deposited on top of the wafer. Using lithography, the resonator layout is defined. Then, deep reactive ion etching (DRIE) is performed, which enables the resonator layout to be etched into the 1.4 µm thick SOI layer down to the buried oxide layer. Finally, isotropic etching of the buried oxide layer is performed using an HF wet etch solution. This removes the resist and releases the resonator from the substrate. As shown in Figure 3.7, six aluminum bond pads can be designed using this fabrication technique. [8]
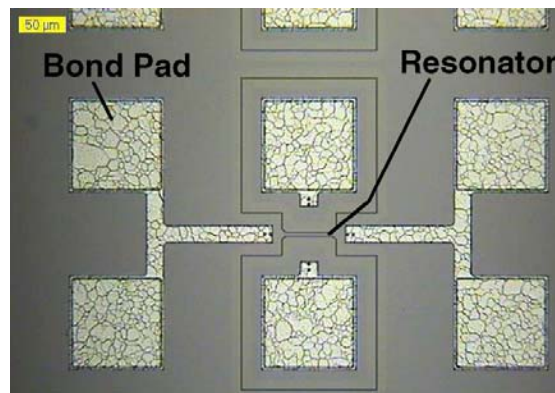
Figure 3.7 The clamped–clamped beam resonator with length = 44µm, width =4µm; and thickness = 1.4µm. [8]

For the characterization, the outer four bond pads are connected to 'ground', such that the beam itself is grounded. The middle two bond pads are used for actuation and measurement purposes. The MEMS resonators are placed in a vacuum (pressure p = 3.45×10^{-4} Torr) chamber throughout the experiments. By increasing and decreasing the excitation frequency in steps of 250 Hz around the fundamental frequency of the resonator, the steady-state dynamic behavior of the resonators can be investigated. Using this data, an amplitude vs. frequency plot was constructed. [8] An example of a typical amplitude–frequency curve for the clamped–clamped beam is shown in Figure 3.8.
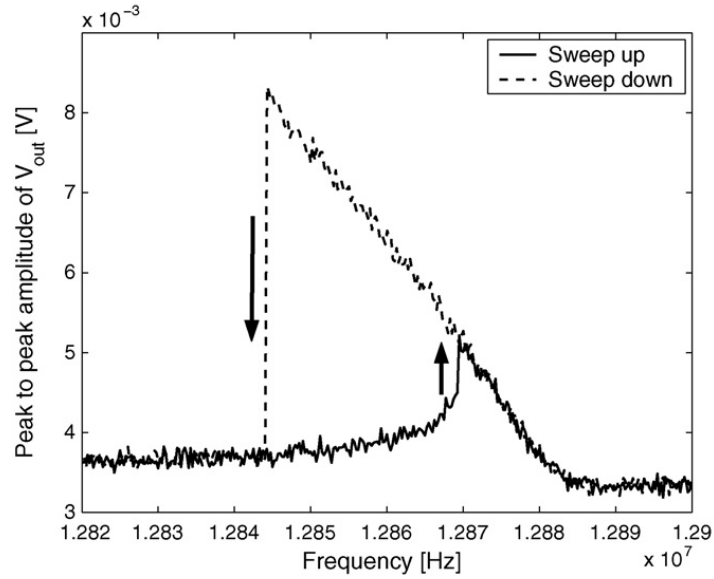
Figure 3.8 The amplitude–frequency curve of a clamped-clamped resonator. [8]

The excitation is given by a dc bias voltage of V_{dc} = 70 V and an ac excitation amplitude of V_{ac} = 139 mV. From Fig 3.8, it can be inferred that even though the resonant frequency of the resonator is about 12.875 MHz, the resonant peak tends to bend to the left (towards lower frequencies) owing to the presence of the nonlinearities in the circuit. The frequency hysteresis is the fact that the sudden jumps in the response (shown by the arrows in Figure 3.8) occur at different frequencies. This is caused by the softening non-linear effect of the resonator, which is investigated in this paper. [8] [50]

The dynamic behavior of the flexural displacement x of the beam resonator is given by [8]:

$$m\ddot{x} + b\dot{x} + k(x)x = F_{e}(x),$$
(3.3)

where m, b and $k(x)$ are the effective (lumped) mass, damping and non-linear stiffness of the system, respectively. The $\dot{x}$ and $\ddot{x}$ denote the first and second time derivative of x, respectively.

The electrostatic force $Fe(x,t)$ is given by [8]:

$$F_{e}(x, t) = \frac{1}{2}\frac{C_0 d_0}{(d_0 - x)^2}V_1^2(t) - \frac{1}{2}\frac{C_0 d_0}{(d_0 + x)^2}V_2^2,$$
(3.4)

29

where C_0 is the capacitance over the gap when $x = 0$ and d_0 is the corresponding initial gap width. $V_1(t)$ and V_2 denote the applied voltages on the electrodes and are defined as [8]:

$$V_1(t) = V_{dc} + V_{ac} \sin(2\pi ft), \qquad V_2 = V_{dc},$$
(3.5)

where V_{dc} is the so-called bias voltage, and V_{ac} and f are the amplitude and frequency of the ac voltage, respectively. The capacitance on the readout side for an arbitrary x is given by [8]:

$$C(x) = C_0 d_0/(d_0 + x).$$
(3.6)

The Taylor expansion of the electrostatic force in x is given by [8]:

$$
F_e(x, t) = \frac{1}{2} \frac{C_0}{d_0} V_{dc}^2 \left(4\frac{x}{d_0} + 8\frac{x^3}{d_0^3} + \text{h.o.t.} \right)
$$
$$
+ \frac{1}{2} \frac{C_0}{d_0} (2 V_{dc} V_{ac} \sin(2\pi ft) + V_{ac}^2 \sin^2(2\pi ft))
$$
$$
\times \left(1 + 2\frac{x}{d_0} + 3\frac{x^2}{d_0^2} + 4\frac{x^3}{d_0^3} + \text{h.o.t.} \right)
$$
(3.7)

The non-linearity in spring stiffness occurs due to both the softening effect of the silicon material (higher-order elastic effects) and the hardening geometric non-linearities (mid-plane stretching of the clamped–clamped beam). The stiffness factor including the higher order nonlinear terms is given by [8] [9] [50] [51] [52] [53]:

$$k(x) = k_0 + k_1 x + k_2 x^2 + k_3 x^3 + k_4 x^4$$
(3.8)

where k_0 is the stiffness parameter in the linear part of the spring force and k_1, k_2, k_3 and k_4 denote the stiffness parameters in the nonlinear portion. This approach can be used for the stiffness function extended to any arbitrary order. Depending on the specific layout of the clamped–clamped silicon beam resonator, k_1 to k_4 may become positive or negative, resulting in hardening or softening behavior, respectively. The terms k_1 and k_2 are directly related to the softening spring stiffness of the resonator beam. The terms k_3 and k_4 have not yet been explored for the modeling of the non-linear behavior of the resonators. [8]

30

An electrical circuit model is used for the actuation and detection of the beam motion as shown in Figure 3.9.
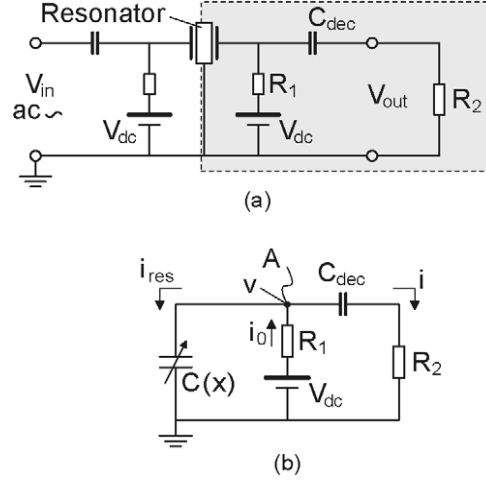
Figure 3.9 The electrical circuit schematic for the clamped–clamped beam resonator model. (a) The output voltage V_{out} measurement, and (b) the output circuit. [8]

An additional decoupling capacitor C_{dec} is used for the dc coupling; $C(x)$ denotes the variable resonator capacitance. The differential equations with the two unknowns v and i for this electrical circuit are determined by node analysis. By using $V_{out} = iR_2$, two coupled differential equations for current i and voltage v are obtained as follows [8]:

$$C(x)\frac{dv}{dt} = -\left(\frac{1}{R_1} + \frac{\partial C(x)}{\partial x}\dot{x}\right)v - i + \frac{V_{dc}}{R_1},$$

$$C_{dec}\left(\frac{dv}{dt} - R_2\frac{di}{dt}\right) = i,$$

$$(3.9)$$

By setting the electrostatic and the mechanical models of the resonator to be equal to each other (ignoring the higher order terms), the following equation is derived [8]:

$$m\ddot{x} + b\dot{x} + \left(k_0 - 2\frac{C_0}{d_0^2}V_{dc}^2\right)x = \frac{C_0}{d_0}V_{dc}V_{ac}\sin(2\pi ft)$$

$$(3.10)$$

The modified stiffness factor becomes [8] $k_{0,e} = k_0 - 2(C_0/d_0^2)V_{dc}^2$ (3.11)

and the electromechanical coupling coefficient is given by [8]: $\eta = (C_0/d_0)V_{dc}$. (3.12)

31

Using the equations 3.9 through 3.12, the equation 3.3 can be redefined as [8]:

$$m\ddot{x} + b\dot{x} + k_{0,e}x = \eta V_{\mathrm{ac}} \sin(2\pi ft).$$

(3.13)

By using the electromechanical coupling coefficient, the relationship between the electrical current and the mechanical velocity can be defined as [8] [54]: $i_m = \eta \dot{x}$. (3.14)

This results in the following equation [8]:

$$\frac{m}{\eta^2}\frac{di_m}{dt} + \frac{b}{\eta^2}i_m + \frac{k_{0,e}}{\eta^2}\int i_m\, dt = V_{\mathrm{ac}} \sin(2\pi ft)$$

(3.15)

This equation 3.15 can be simplified further to represent a harmonically excited RLC circuit model of a resonator as given by equation 3.16 [8].

$$L_m\frac{di_m}{dt} + R_m i_m + \frac{1}{C_m}\int i_m\, dt = V_{\mathrm{ac}} \sin(2\pi ft)$$

(3.16)

where inductance L_m , resistance R_m and capacitance C_m are given by [8] [54]:

$$L_m = \frac{m}{\eta^2}, \quad R_m = \frac{b}{\eta^2} = \frac{\sqrt{k_{0,e}m}}{\eta^2 Q} \quad \text{and} \quad C_m = \frac{\eta^2}{k_{0,e}}$$

(3.17)

The linear quality factor Q is defined by [8]: $Q = \sqrt{k_{0,m}m}/b$ (3.18)

The above heuristic approach was analyzed only for a linear case. In order to understand the total behavior of the clamped-clamped resonator, a complete numerical approach was established using the software package AUTO. Here, the resonator is modeled by defining the state column $x = [x \quad \dot{x} \quad v \quad i]^T = [x_1 \quad x_2 \quad x_3 \quad x_4]^T$ (3.19)

In equation 3.19, x_1 , x_2 , x_3 , x_4 represent the displacement, velocity, voltage and current of the actuated resonator beam. [8]

In this way, using $x = f(x, t)$, the total model was established in matrix form as shown in equation 3.20. [8]

$$f(x,t) = \begin{bmatrix} x_2 \\ \dfrac{1}{m}\left(-bx_2 - k(x_1) + \dfrac{1}{2}\dfrac{C_0 d_0}{(d_0-x_1)^2}V_1^2(t) - \dfrac{1}{2}\dfrac{C_0 d_0}{(d_0+x_1)^2}V_2^2\right) \\ -\dfrac{d_0+x_1}{C_0 d_0}\left\{\left(\dfrac{1}{R_1}-\dfrac{C_0 d_0}{(d_0+x_1)^2}x_2\right)x_3 + x_4 - \dfrac{V_{dc}}{R_1}\right\} \\ -\dfrac{d_0+x_1}{C_0 d_0 R_2}\left\{\left(\dfrac{1}{R_1}-\dfrac{C_0 d_0}{(d_0+x_1)^2}x_2\right)x_3 + \left(1+\dfrac{C_0 d_0}{(d_0+x_1)C_{dec}}\right)x_4 - \dfrac{V_{dc}}{R_1}\right\} \end{bmatrix}.$$

(3.20)

The numerical and experimental results were compared and analyzed. For all the experiments, the dc bias was kept constant at 70 V and the ac bias varied between 20 and 349 mV. Figure 3.10 shows the typical response of the output voltage with varying frequency obtained from the experiments for dc bias voltage V_{dc} = 70 V and ac bias voltage V_{ac} = 20mV. [8]
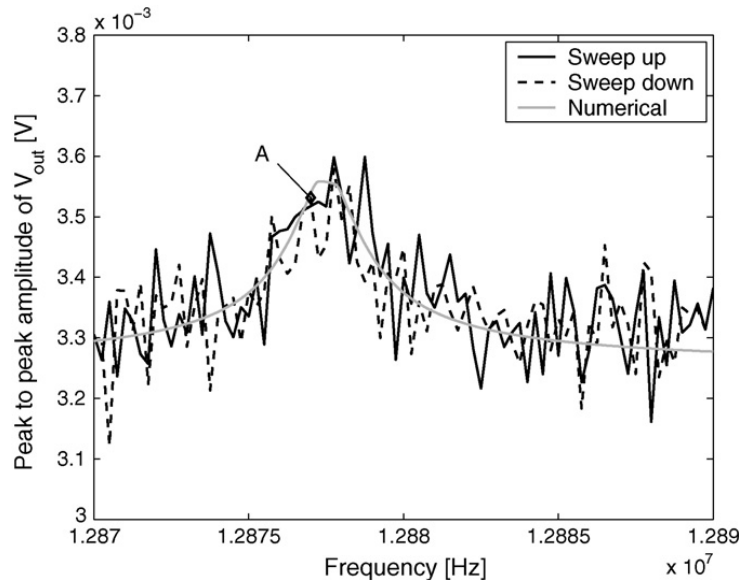
Figure 3.10 The amplitude–frequency curve with V_{dc} =70 V and V_{ac} =20 mV. [8]

The resonant frequency was given by [8]:

$$f_{0,e} = (1/2\pi)\sqrt{k_{0,e}/m}$$

(3.21)

The value $f_{0,e}$ matched very closely with the measured value of 12.875 MHz . The softening effect was further investigated throughout this paper. Table 3.1 shows the numerical parameter values of the total resonator model found after fine tuning the m, k_0 and b values. [8]

33

Table 3.1 The numerical parameter values of the total model for V_{dc} = 70 V and V_{ac} = 20 mV. [8]

Parameter	Value	Unit
m	2.273×10^{-13}	kg
k_0	1.505×10^3	N/m
b	3.083×10^{-9}	N s/m
Q	6.000×10^3	–
f_0	12.949×10^6	Hz
$f_{0,e}$	12.878×10^6	Hz
d_0	0.330×10^{-6}	m
C_0	0.185×10^{-15}	F
R_1	1.0×10^6	Ω
R_2	50.0	Ω
C_{bias}	0.082×10^{-6}	F
ρ	2.330×10^3	kg/m^3

The model of the clamped–clamped beam resonator described in this paper establishes a good starting point for understanding and predicting the dynamic non-linear behavior of RF MEMS resonators. For future study, this model should be further improved and extended to include higher order non-linear stiffness terms to establish the total optimized model of the resonator.

3.3 Performance Analysis of RF MEMS Resonators

In this paper [55], a strategy for the performance analysis of RF MEMS resonators was discussed. For an optimum CMOS–MEMS resonant system, large signal transduction capability, high structure robustness and high level of tuning of its electrical parameters (i.e., its resonance frequency) are required. These parameters are directly related to the physical characteristics of the resonator (dimensions and physical properties) through the following key parameters: motional resistance R_m, collapsing voltage V_{col} and the dependence of the resonant frequency with the applied biasing voltage (i.e., frequency tuning) [55].

3.3.1 Motional Resistance

The motional resistance R_m is given by [55] [56]:

$$R_m = \frac{k_m}{2 \cdot \pi \cdot f_{res}} \cdot \frac{s^4}{\varepsilon^2 \cdot A^2 \cdot V_{dc}^2 \cdot Q}$$

(3.22)

In equation 3.22,

k_m = the mechanic elastic constant of the structure,

f_{res} = the resonance frequency of the resonator,

s = the distance from the resonator to the electrodes,

ε = the dielectric constant of the medium,

A = the coupling area between the resonator and the electrode ($A = L_{ct}$),

V_{dc} = the applied dc voltage to the resonator, and

Q = the quality factor of the resonator.

This motional resistance (R_m) is directly related to the signal losses and hence, gives a good estimate of the efficiency of the coupling in the capacitive coupled resonators. R_m is a key parameter in RF MEMS applications, especially when a 50 Ω impedance matching is required. When the MEMS resonator is used as a frequency reference for local oscillators, a low value of this motional resistance reduces the required negative resistance of the amplifier to ensure oscillation. This in turn reduces the required oscillator bias current. [55] [56] [57]

3.3.2 Collapse Voltage

The collapse voltage V_{col}, also known as the breakdown, pull-down or vertical snap-in voltage is given by [55] :

$$V_{col} = \sqrt{\frac{c \cdot E \cdot t^3 \cdot sv^3}{\varepsilon \cdot L^4}}$$

(3.23)

where   E = the Young modulus of the material,

t = the thickness of the layer,

sv = the distance to the substrate,

L = the length of structure, and

c = numeric value that depends on the design structure of the resonator

A typical value of c is 11.9 for a clamped-clamped resonator and 0.28 for a cantilever. [55] [58]

35

Replacing *t* with resonator width *w* and *sv* with the resonator gap *s*, the collapse voltage is transformed into the lateral collapse voltage (resonator against drive electrode). This pull down voltage gives the estimate of the maximum dc voltage that the resonator can withstand without vaporizing or causing stiction between the resonator and the substrate.

3.3.3 Frequency Tuning

The phenomenon that the resonant frequency changes with varying applied bias DC voltages is known as the softening effect. [55] [59] This effect is very dominant in electrostatically driven and capacitively transduced resonators. It is directly related to the stiffness factor, which is the key parameter in modifying the resonant frequency of a two-port oscillator. [55] [60] The resonant frequency is related to the stiffness factor and the mechanical elastic constant by [55]:

$$f_{\mathrm{res}} = f_0 \left(1 - 2 \cdot \frac{k_e}{k_m} \right)^{1/2} \approx f_0 \cdot \left(1 - \frac{k_e}{k_m} \right)$$

(3.24)

where f_{res} = actual (modified) resonant frequency of the resonator

f_0 = natural resonant frequency of the resonator

k_e = stiffness factor of the resonator

k_m = mechanical elastic constant of the resonator.

For small bending or vibrations of the resonator, the electrical elastic constant is defined as [55]:

$$k_e = \frac{\varepsilon \cdot L_c \cdot t}{s^3} \cdot V_{\mathrm{dc}}^2$$

(3.25)

Using the equations 3.24 and 3.25, the normalized frequency tuning can be defined as [55]:

$$\mathrm{FT} \equiv \left| \frac{1}{f_0} \cdot \frac{\partial f_{\mathrm{res}}}{\partial \left(V_{\mathrm{dc}}^2 \right)} \right| = \frac{1}{k_m} \cdot \frac{\varepsilon \cdot L_c \cdot t}{s^3}$$

(3.26)

Hence, the actual (modified) resonant frequency of the resonator can be defined in terms of this frequency tuning and the dc bias voltage as shown in equation 3.27 [55]:

36

$$f_{\text{res}} = f_0 \cdot \left(1 - \text{FT} \cdot V_{\text{dc}}^2\right)$$

(3.27)

It can be very useful to take advantage of the non-linear spring softening effect in a variety of RF applications, including fine-tuning the resonant frequency in MEMS devices, which helps to compensate for the fabrication process vibrations and temperature variations for oscillation applications. [55] [61]

3.3.4 Expressions for Clamped-Clamped Beams

For clamped-clamped resonators, the mechanical elastic constant and the fundamental resonant frequency can be defined as [55] [62]:

$$f_0 = 1.03 \cdot \sqrt{\frac{E}{\rho}} \cdot \frac{W}{L^2}$$

$$k_m = \frac{16 \cdot E \cdot t \cdot W^3}{L^3}$$

(3.28)

Using equation 3.28, the expressions for motional resistance R_m, collapse voltage V_{col} and bridge frequency tuning $\text{FT}_{\text{bridge}}$ of the resonator can be redefined as [55]:

$$R_m = 2.48 \cdot \sqrt{E \cdot \rho} \cdot \frac{1}{\varepsilon^2 \cdot V_{\text{dc}}^2 \cdot Q} \cdot \frac{W^2 \cdot s^4}{L_c^2 \cdot L \cdot t}$$

$$V_{\text{col}} = \sqrt{\frac{11.9 \cdot E \cdot t^3 \cdot sv^3}{\varepsilon \cdot L^4}}$$

$$\text{FT}_{\text{bridge}} = \frac{1}{k_m} \cdot \frac{\varepsilon \cdot L_c \cdot t}{s^3} = \frac{\varepsilon \cdot L_c \cdot L^3}{16 \cdot s^3 \cdot E \cdot W^3}$$

(3.29)

3.3.5 Definition of Figures of Merit

The overall figure of merit of an RF MEMS resonator can be defined in terms of motional resistance R_m, the collapse voltage V_{col} and the frequency tuning FT for comparative analysis as shown in equations 3.30 and 3.31 [55]

$$\text{FOM} = V_{\text{col}} \cdot \text{FT} / R_m$$

(3.30)

$$\text{FOM} \propto \frac{1}{E \cdot \sqrt{\rho}} \cdot \frac{\sqrt{t^5 \cdot sv^3}}{s^7}$$

<div align="right">(3.31)</div>

In the relationship shown in 3.31,

E = the Young modulus of the material

t = the thickness of the layer

sv = the distance to the substrate

s = resonator gap

ρ = resistivity of the material

This figure of merit (FOM) promotes robust resonators with high capability and low motional resistance. It provides a good measure to compare the different layers in any CMOS technology so that the most optimal layer for the appropriate technology can be chosen as the preferred fabrication process of the MEMS resonator. It can also be applied to any resonator topology other than the clamped-clamped beam resonator. [55]

For the RF MEMS analysis in this paper, several clamped–clamped resonators in the VHF frequency range using the CMOS commercial technologies, AMS and UMC, were fabricated and characterized. The electrical characterization of the fabricated resonators was performed using a network analyzer (Agilent 5100) and Cascode Microtech Infinity GSGSG probes under atmospheric pressure. The S_{21} parameters were extracted and analyzed. [55]

Figure 3.11 shows the resonator frequency response (magnitude and phase) for different biasing voltages for an applied input power of −10 dBm. From this figure, it can be seen that the resonator has a peak magnitude of about 7 dB and a clear resonance and phase shift of nearly 85° for an applied DC voltage of 80 V without using any amplification circuitry. A quality factor Q = 42 was achieved, which is higher than most other similar resonators without on-chip circuitry fabricated with AMS technology. [55]
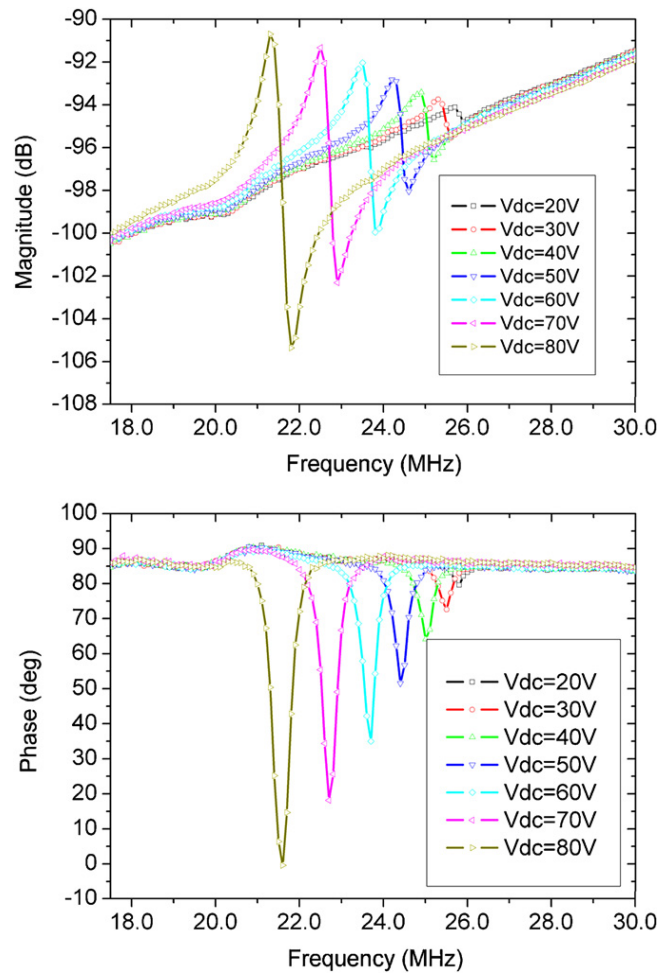
Figure 3.11 The S$_{21}$ measurement. (a) The magnitude, and (b) the phase plots for different applied dc voltage. [55]

39

CHAPTER 4

RESEARCH METHODOLOGY

4.1 Introduction

The research was divided into two components – the linear model and the non-linear model for the clamped – clamped Al_2O_3 RF MEMS resonators. For the fabrication process, the methodology discussed in section 3.1 was implemented. In order to predict the characterization results of the fabrication resonators, the design was first simulated using the Advanced Design System (ADS). Once this was completed, an attempt was made to analyze both the linear and non-linear behavior by constructing the complete solution of the mechanical behavior of the resonator using the software tool MathCAD. Finally, an amplifier circuitry was integrated with the existing resonator model to improve the performance of the resonators.

4.2 ADS Simulation and Characterization of the Resonator Model

As the first phase in my research, the fabricated Al_2O_3 resonator devices were characterized for pull-down (or collapse) voltage and resonance. Meanwhile, a basic linear model of the RF MEMS resonator was simulated using the Advanced Design System (ADS) tool in order to predict the resonant frequency as well as the S_{21} of the device.

4.2.1 Characterization

With the aid of the probing station (Micromanipulator Model: 8060-US8-V0-1-A) and the Agilent E3620A power supply, dc characterizations of the resonators were performed. These measurements gave an estimate for the electrical break-down or collapse voltage of the resonator beams. Figure 4.1 shows the block diagram of the experimental setup and the probing station used for the dc characterization.

40
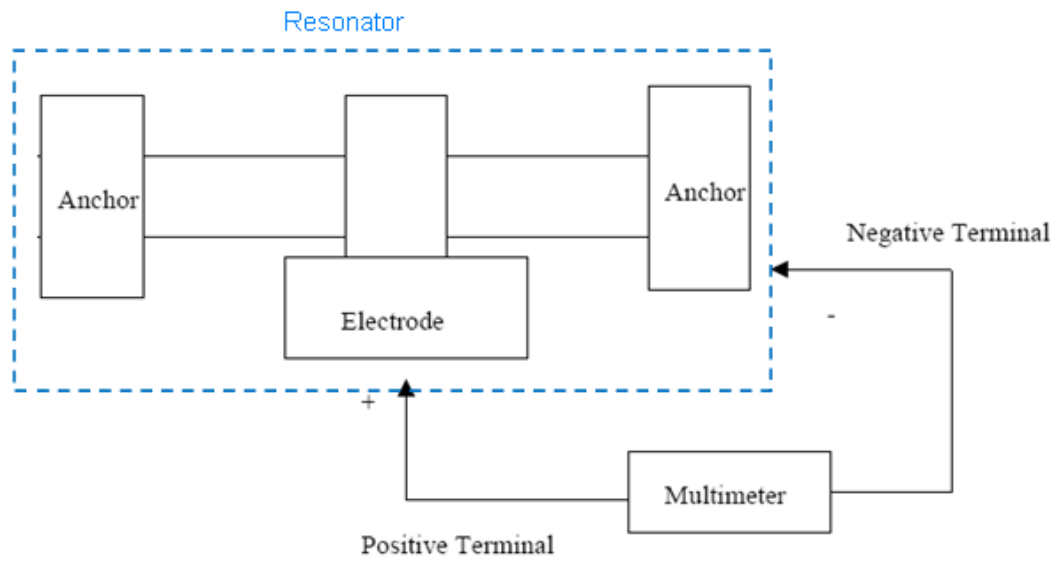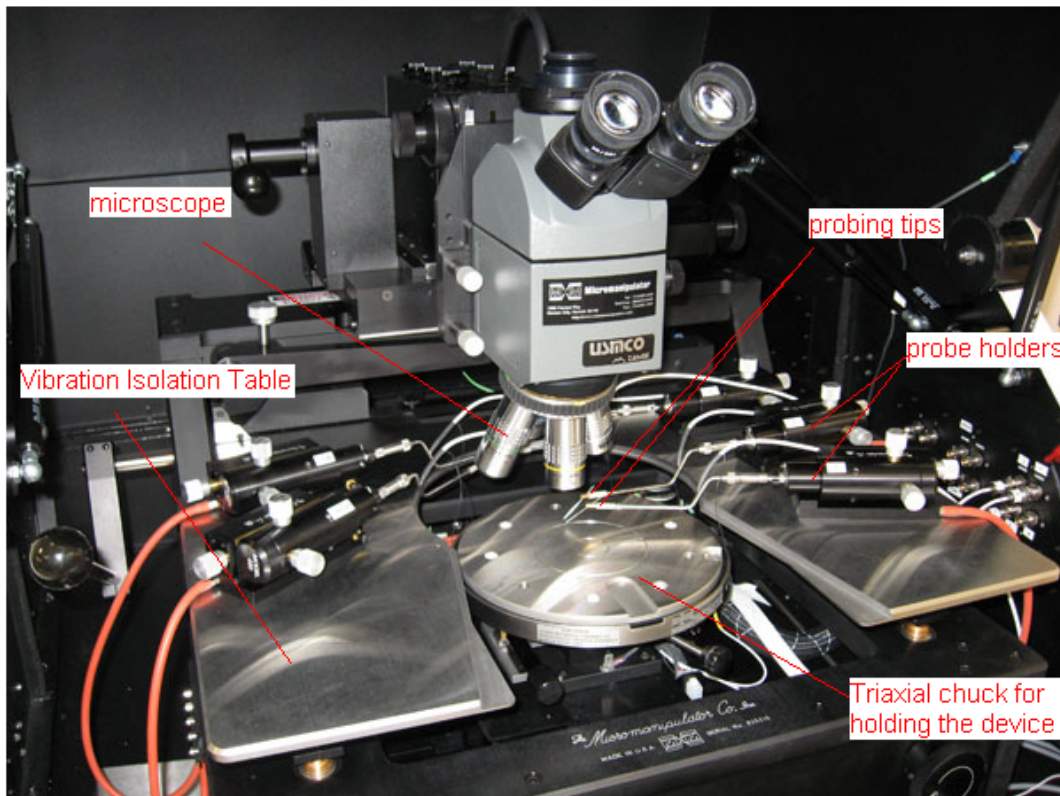
Figure 4.1 The dc characterization. (a) The block diagram of the experimental setup and (b) the probing station [63] used for the dc characterization.

Table 4.1 The dc measurements for 2 MHz, 5 MHz and 10 MHz resonators.

Type of Resonators	Resistance between 2 anchors (Ω)	Resistance between anchor and electrode (Ω)	Pull Down Voltage Vpd (V)
2 40 80	57.8	-	10.5
2 50 60	130	∞	11.6
2 30 80	56.8	∞	10.03
5 40 80	61.3	∞	15.74
5 50 60	63.7	∞	15.2
5 40 70	64.5	∞	19.1
10 40 80	71.8	∞	27.1
10 50 60	140.1	∞	27.8
10 30 60	118.2	∞	12.3

From Table 4.1, it can be inferred that isolation of the resonators have been maintained as required since the resistance between the anchor and electrode is measured to be infinite (open circuit). The isolation was used to separate the working from the non- working devices. Once the functional resonator devices were identified, their positions were recorded using the available resonator map. Table 4.2 shows the typical pull down voltages for 2 MHz, 5 MHz and 10 MHz resonators. Figure 4.2 is the graphical representation of Table 4.2 and gives an idea of how the pull-down voltages vary with resonant frequencies which is helpful to know for fabrication and characterization purposes.

Table 4.2 Typical pull down voltages for 2 MHz, 5 MHz and 10 MHz resonators.

Resonant Frequency f (MHz)	Pull Down Voltage Vpd (V)
2	11.6
5	16.7
10	27.8
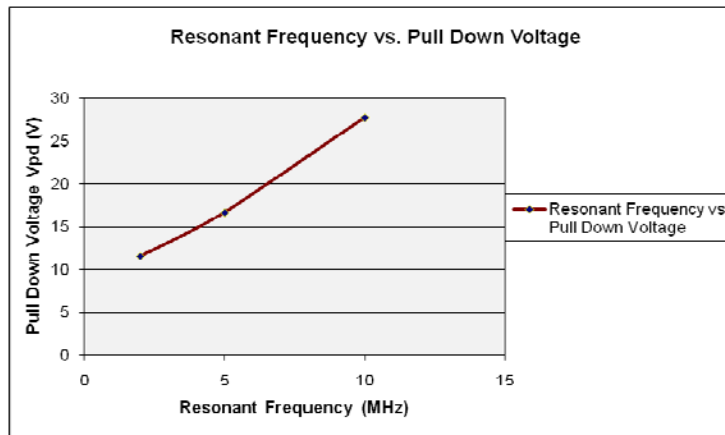
Figure 4.2 The graphical representation of Table 4.2.The pull-down voltages for various resonant frequencies.

In general, the pull-down voltages for 2 MHz resonators ranged between 10V and 11.6 V, for 5 MHz resonators between 15 V and 19 V, and the 10 MHz resonators between 12 and 27 V. These measurements were important to estimate the maximum allowable bias voltage that can be used for the RF resonance measurements

After the dc characterizations, the resonator die was attached to a 50 Ω transmission line circuit board using bonding glue. One of the identified resonators was then wire bonded to the short and long transmission line of the circuit board using the West Bond Model 7476E-79 Wedge Wire Bonder. Once the wire bonding was completed successfully, the SubMiniature Version A (SMA) connectors (or tabs) were carefully soldered to the short and long transmission lines of the bonded circuit board. The SMA tabs are semi-precision, subminiature devices that provide repeatable electrical performance up to 12.4 GHz with a flexible cable. These connectors will later be used as the RF input and output terminals. To ensure that the bonding was still intact after soldering, the isolation was tested for that particular resonator. Figure 4.3 shows the West Bond Wedge Wire Bonding equipment set up and the resonator circuit board including the SMA tabs.
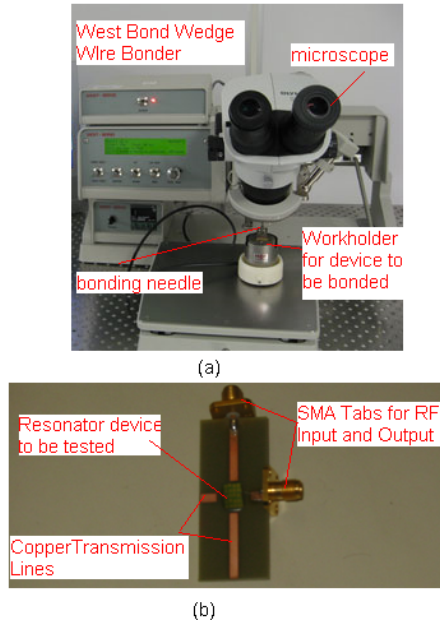
Figure 4.3 (a) The West Bond Wedge wire bonding equipment set up [63], and (b) the circuit board with the attached resonator die and the SMA tabs. [64]

43

The resonator was now ready for the RF resonance characterization using the E5071C Series Network Analyzer. The network analyzer was first calibrated for the specific frequency range desired. Then the resonator circuit board was put inside a custom built vacuum chamber and attached to the analyzer using a suitable coaxial cable via the SMA tabs. Port 1 was used as RF input and port 2 as the RF output. It was also verified that the bias voltage supplied did not exceed the pull down voltages measured earlier. Figure 4.4 shows the RF characterization set up and a typical RF response of a 2 MHz resonator.
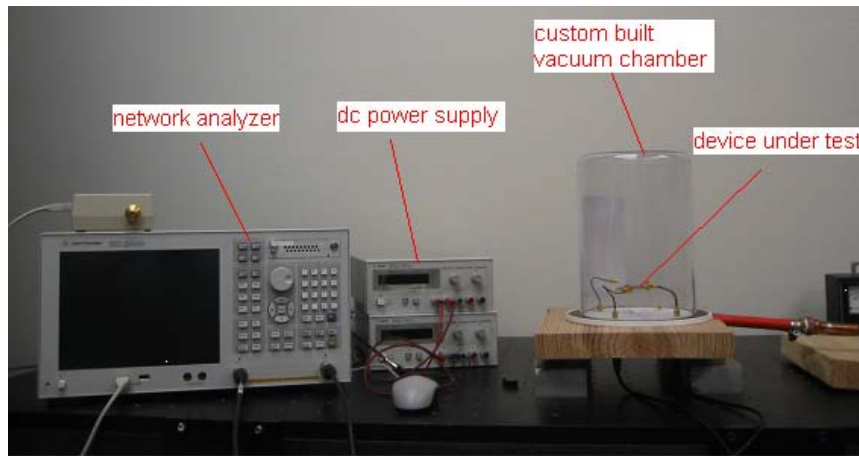
(a)
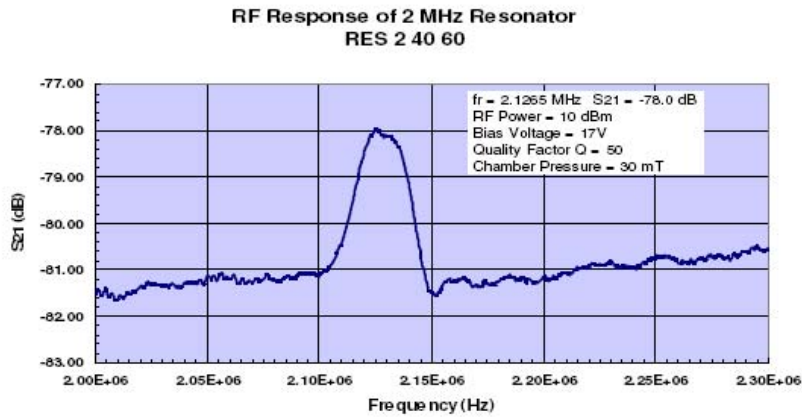
(b)

Figure 4.4 (a) The RF characterization set up, and (b) the typical RF response (S_{21}) of a 2 MHz resonator. [64]

From Figure 4.4 (b), it can be inferred that the resonant frequency of oscillation occurs at about 2.2 MHz, the S_{21} for the device is about -78 dB and the Q-factor was about 50. Typical values of S_{21} and Q-factor obtained for 2 MHz, 5 MHz, 10 MHz and 25 MHz resonators were between -40 and -70 dB and 7 and 50, respectively. These values found were lower than desired. It should be noted that the higher frequency resonators showed inferior results than the 2 MHz resonators. The dc and RF characterizations pertained to the linear behavior of the resonator model. All experiments were conducted in the Microsensor lab of the UT-Arlington Nanofabrication facility.

4.2.2 ADS Simulation

The resonator circuit model was set up using the methodology and equations described in Section 3.1. The required parameter values such as the length, width and the air gap of the resonator beam were based on the techniques used for fabricating the Al_2O_3 resonator devices. Figure 4.5 shows the ADS schematic of the resonator model including the equations used.
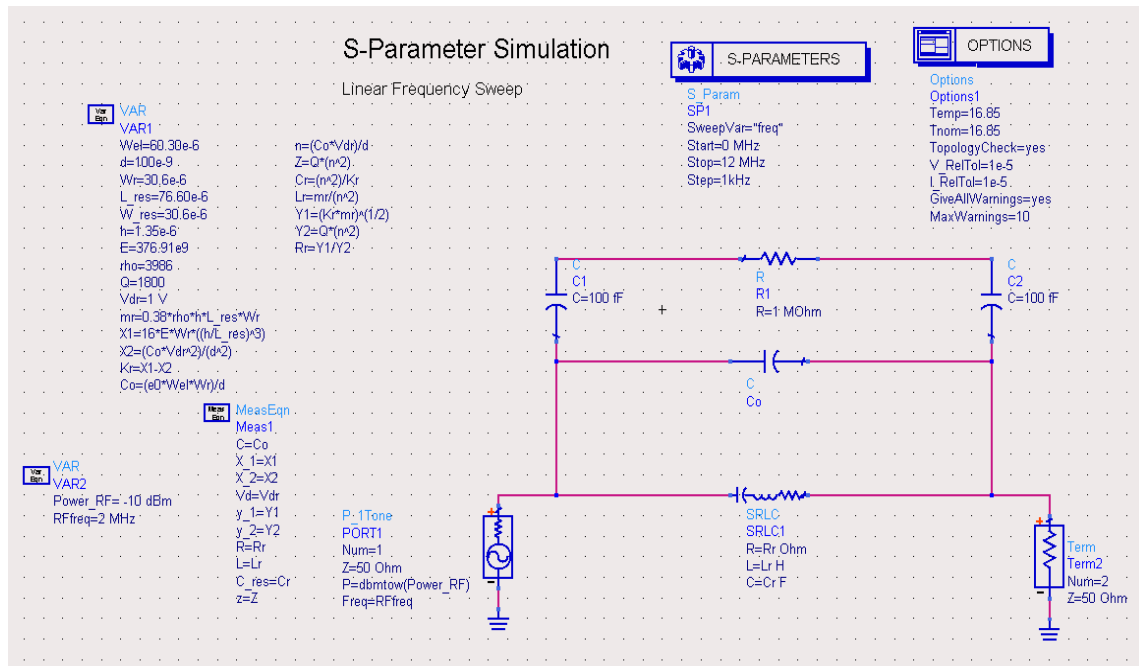
Figure 4.5 The ADS schematic of the resonator model.

The resonator circuit model shown in Figure 4.5 were simulated for various dc bias voltages ranging from 0 V to 10 V. Figure 4.6 shows the RF response of a 2 MHz resonator

model simulated at the bias voltages of 1 V, 4 V, 5 V and 7 V. The resonant frequency occurs at about 2.29 MHZ, which is very close to the experimentally measured value of 2.2 MHz. Similar simulations were performed for other frequency resonators as well. Figure 4.7 shows the RF response of a 10 MHz resonator. The resonant frequency in this case occurred at 13.85 MHz, which matched very closely to the theoretical value of 13.6 MHz, as well as the experimentally measured value of 13.71 MHz.
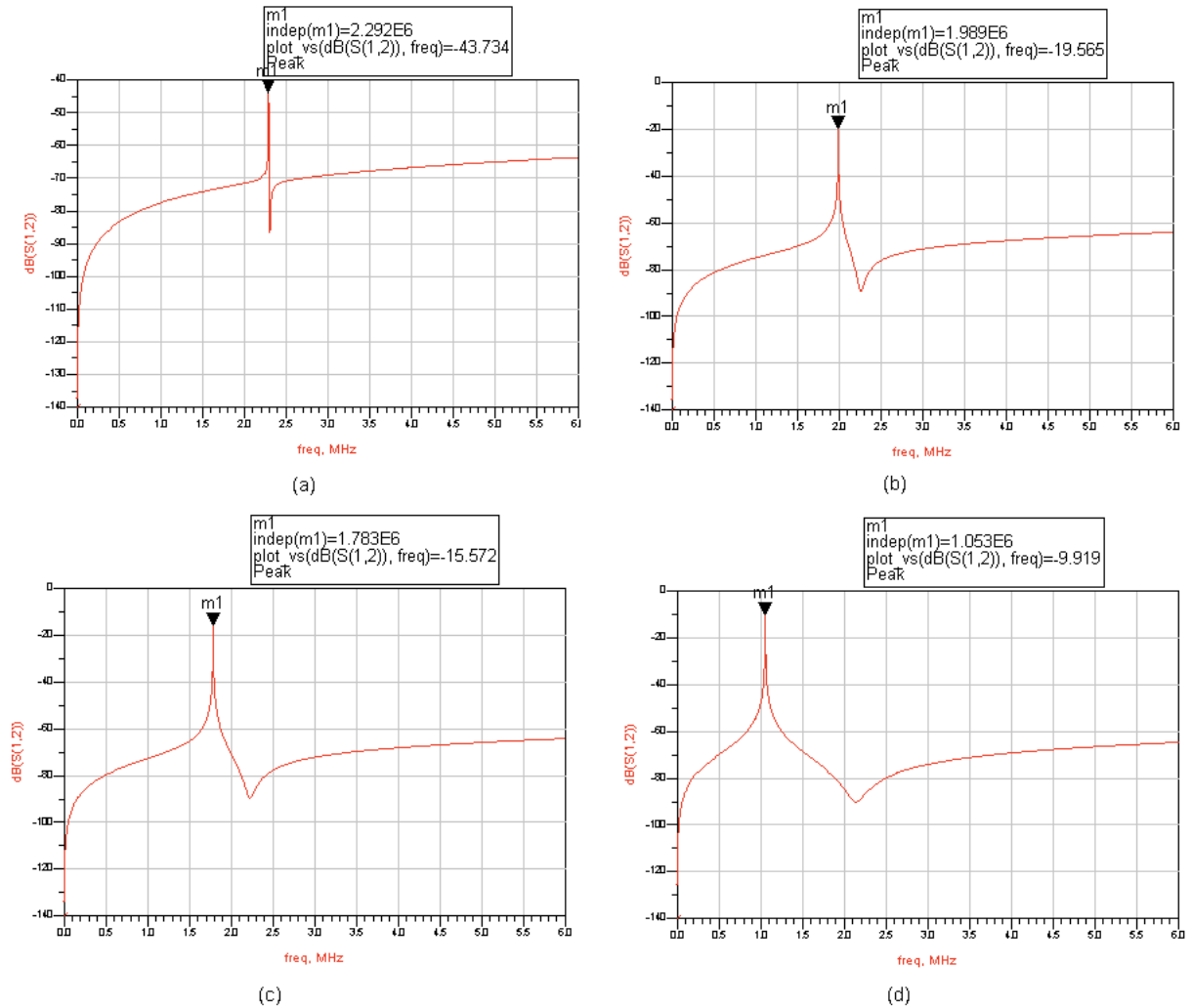
Figure 4.6 The simulated RF response (S_{21}) of a 2 MHz resonator for varying dc bias voltages. (a) V_{dc} = 1 V, (b) V_{dc} = 4 V, (c) V_{dc} = 5 V, and (d) V_{dc} = 7 V.

(a)   (b)
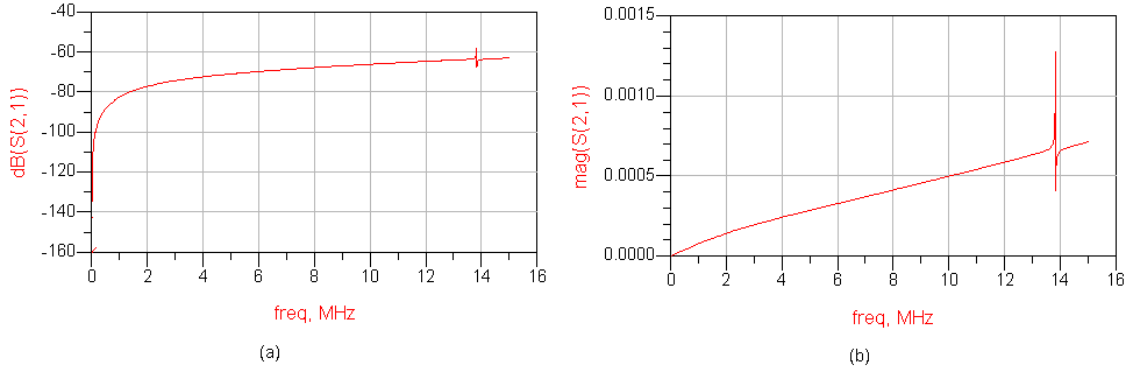
Figure 4.7 The simulated RF response of a 10 MHz resonator.
(a) in decibel scale, and (b) in magnitude.

Next, the non-linear softening behavior of the resonator was tested. From Figure 4.6,

the resonant frequencies at the different bias voltages were extracted and expressed in both

tabular (Table 4.3) and graphical (Figure 4.8) represenation for a 2 MHz resonator.

Table 4.3 The shift in resonant frequency with varying bias voltage for a 2 MHz resonator.

Voltage Bias (V)	Resonant Frequency (MHz)
7	1.053
5	1.78
4	1.989
1	2.29
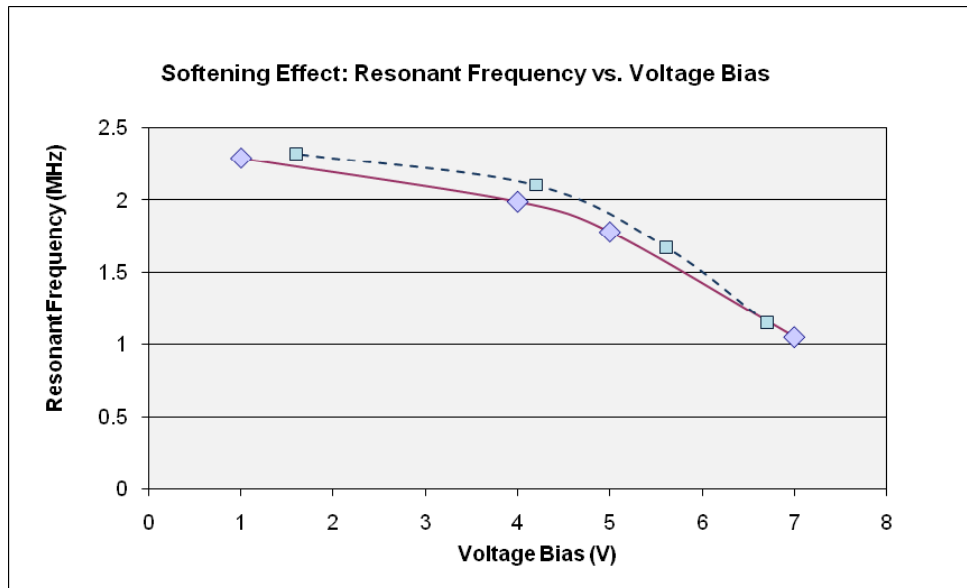
Figure 4.8 The response of resonant frequency with varying bias voltage.for
a 2 MHz resonator. (The solid line denotes the simulated results and the
dotted line denotes the experimental results).

47

From Table 4.3 and Figure 4.8, it can be seen that there is a gradual non-linear decrease of resonant frequency with increasing bias voltage. This demonstrates the softening effect of the resonator model.

<div align="center">4.3 Stiffness Factor and Total Model Derivation</div>

In the mechanical models of the clamped-clamped resonator discussed in Sec 3.1 and 3.2, the stiffness factor was assumed to be constant and did not include any higher order non-linear terms. In order to improve accuracy, the stiffness coefficient terms up to the 5th order were included in the mechanical resonator model derivation. The complete model was constructed similar to the numerical analysis described in Section 3.2 but was modified to represent the model (Figure 4.5) discussed in Section 4.2. The entire derivation is provided in Appendix A.

<div align="center">4.4 MathCAD Calculations</div>

MathCAD is a powerful tool to compute numerical models. Therefore, MathCAD code was written using the complete derived model shown in Appendix A. The simulations from this code were used to predict both the linear and non-linear behavior of the resonator.

4.4.1 Code without Loop

Using this MathCAD code, the response of the resonator was simulated at a specific frequency and had to be run each time the frequency was changed. The simulations were run for different bias voltage and frequencies. This code is provided in Appendix B.

4.4.2 Code with Loop

Since the MathCAD simulations can become rather tedious, the code was optimized using a for-loop block so that the simulations could be run over a specific frequency sweep. This enabled a single simulation to be run instead of several simulations as in the previous case (Section 4.4.1) over a given frequency sweep. However, the downside of this method is the fact that one simulation requires a longer run time since the code was more complex and required more computer memory usage at any given time. This code is provided in Appendix B.

A clean prominent resonance occurred at around 11.65 MHZ when both the dc and ac bias voltages are set to 1 V as shown in Figure 4.9 (a). However, there were some traces of non-linear harmonics at other bias voltages especially at higher dc bias voltages. Figure 4.9 (b) shows an example of such harmonics in the current response of the resonator model at dc bias voltage of 30V and ac bias voltage of 0.2 V. From the current amplitude results in Figure 4.9, the S_{21} parameters were calculated at varying bias voltages to order to determine the feasibility of the code.
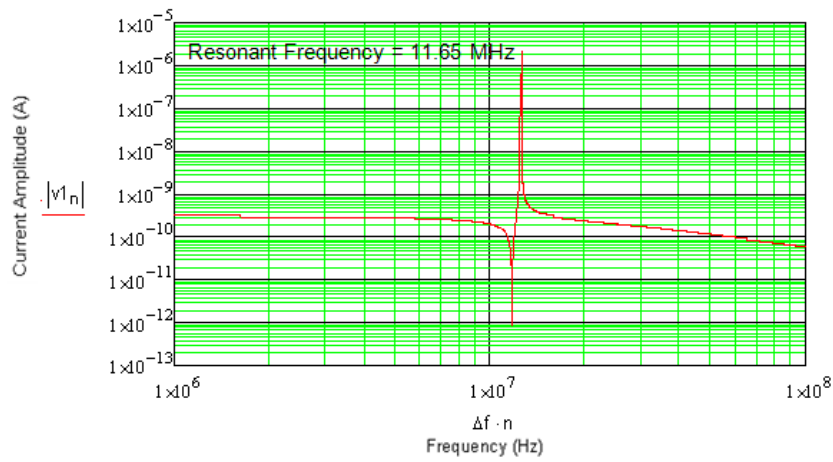
(a)
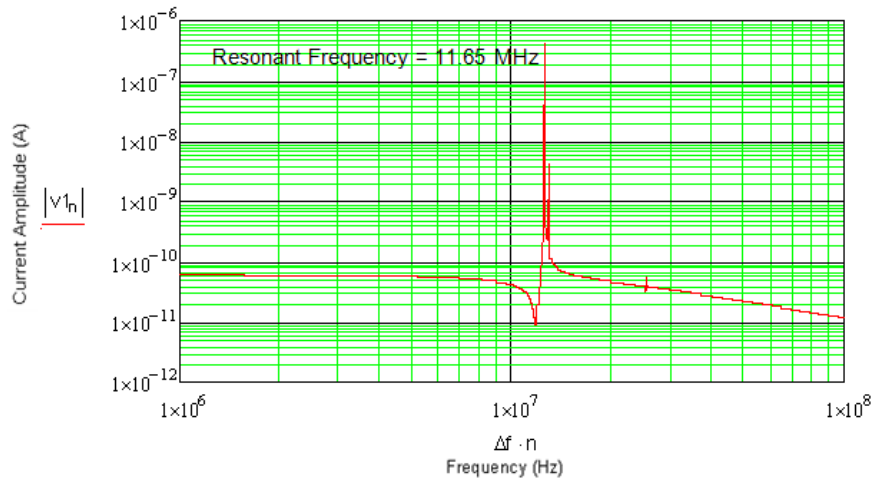
(b)

Figure 4.9 The current response of the total resonator model. (a) The clean response at V_{dc} =1 V and V_{ac} = 1 V , and (b) the response showing traces of harmonics with V_{dc} = 30V and V_{ac} = 0.2 V.

In order to find the S_{21} values from the current amplitude response, the resonator can be modeled in the following way:
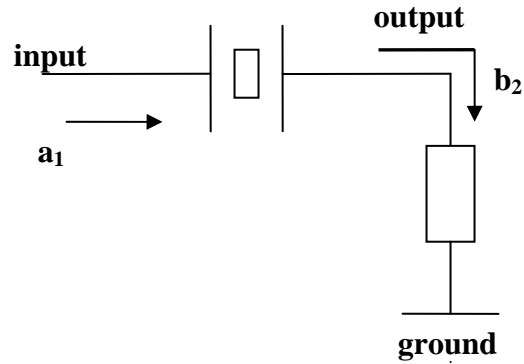
Figure 4.10 The model to extract S_{21} from the simulated current response.

$$a_1 = \frac{v_{ac}}{\sqrt{z_0}}$$

$$b_2 = i\sqrt{z_0}$$

$$S_{21} = \frac{b_2}{a_1} = \frac{i \cdot z_0}{v_{ac}}$$

$$S_{21\_db} = 10 \cdot \log(S_{21})$$

(4.1)

As shown in Figure 4.10, a_1 is the incident signal and b_2 is the reflected signal. Using the set of equations in 4.1, the S_{21} values for different ac and dc bias values were found. The S_{21} was about -38 dB for all bias voltages. This value was quite similar to the experimental value of -40 dB, which verified that this complete numerical model was valid. The model was simulated for different dc and ac bias voltages. The current amplitude showed a linear relationship with varying ac voltage where as though the current amplitude did vary that much with varying dc voltage, it showed a somewhat nonlinear relationship.

Figure 4.11 shows the linear relationship between current amplitude and ac voltage when the dc bias was kept constant at 1 V.

On the other hand, Figure 4.12 shows the non-linear relationship between current amplitude and dc voltage when the ac bias was kept constant at 1 V.
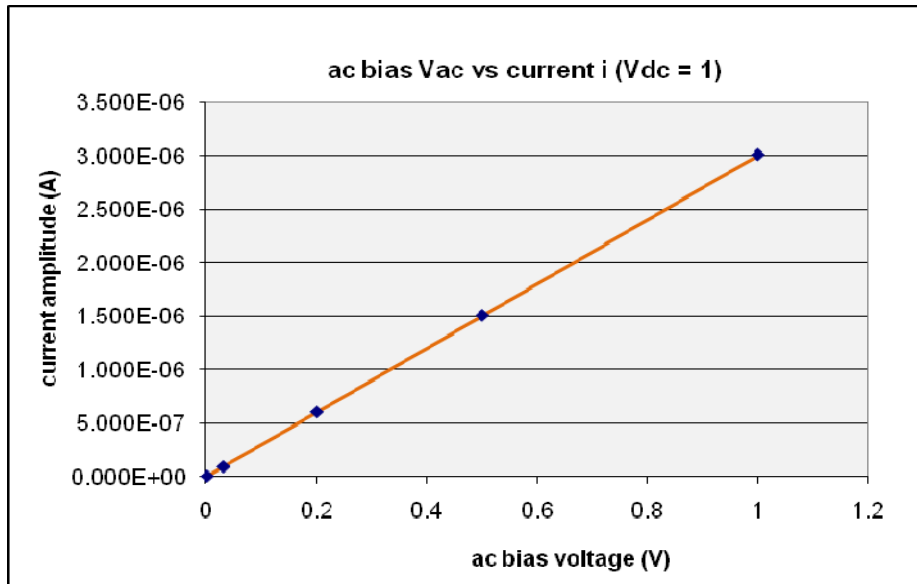
Figure 4.11 The current response with varying ac voltage when the dc bias was kept constant at 1 V.
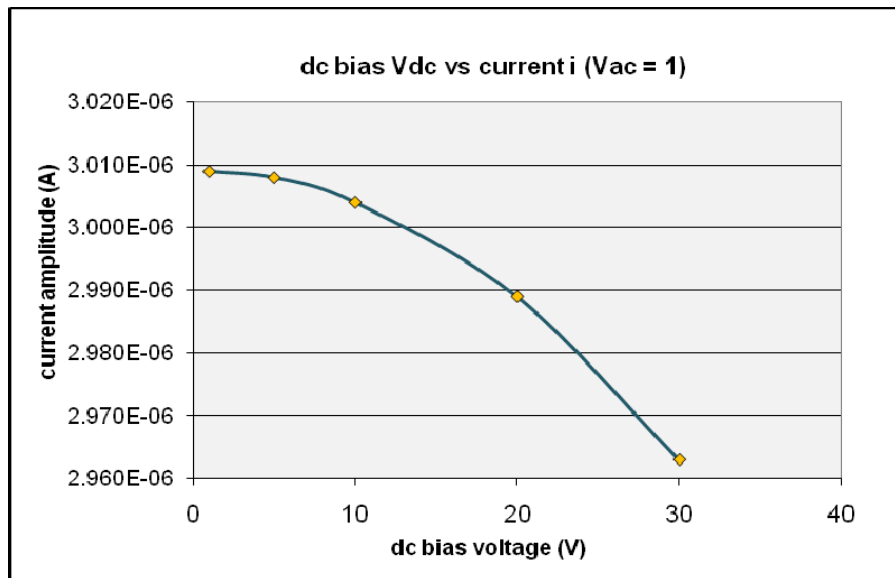
Figure 4.12 The current response with varying dc voltage when the ac bias was kept constant at 1 V.

All the data obtained for varying ac and dc bias voltages are provided in Appendix C. The exact interpretation from this data would benefit from further future thorough research, testing and simulations of the resonator model.

<u>4.5 Adding an Amplifier to Improve the RF Response S_{21} and Quality factor</u>

An RF amplifier is used to convert a low-power radio-frequency signal into a larger signal of significant power, typically for driving the antenna of a transmitter. In many cases, it is optimized for high efficiency, high 1 dB compression point, moderate return loss on the input and output, good gain, and good heat dissipation. [5]. It also improves the Q-factor of the device by eliminating some of the loading effects of the components.

Therefore, in order to improve the forward gain (S_{21}) and the quality factor of the fabricated device, an amplifier was attached to the resonator device. The amplifier circuit was built using the MMG30XX PCB board. The MMG30XX circuit was first set up independently for the ohm test measurement as described in the RF amplifier datasheet. After ensuring that the ohm test results matched with those in the data sheet [65], the resonator was attached to the board and wire bonded to the Input and output terminals of the board.

Figures 4.13, 4.14 and 4.15 show the RF response S_{21} of the amplifier circuit (without the resonator) at RF Power of -10 dBm, 0 dBm and +10 dBm.
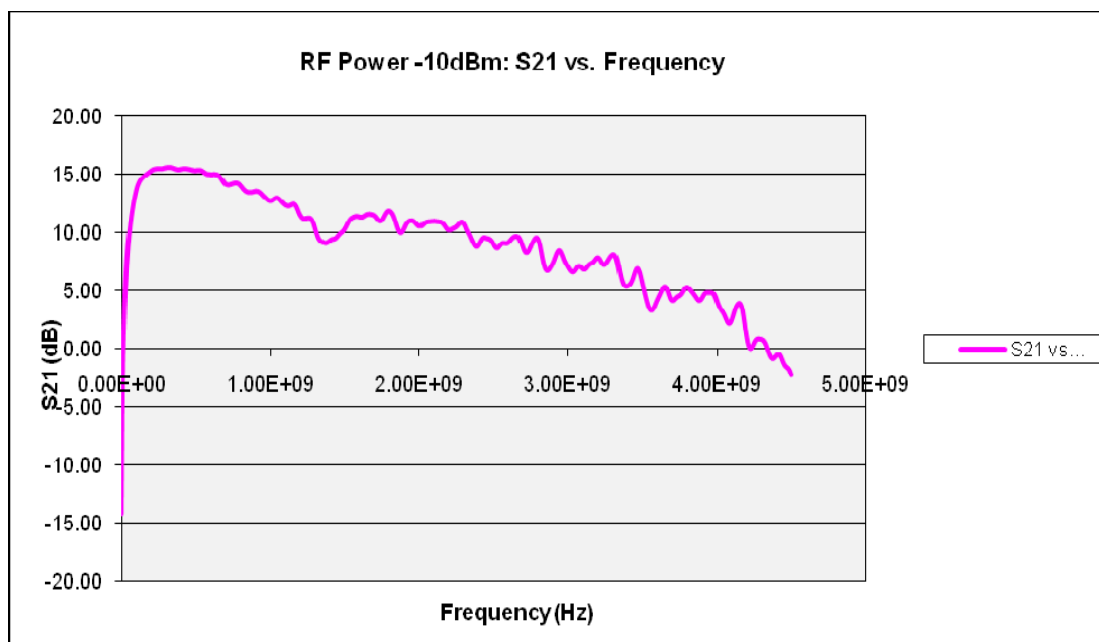
Figure 4.13 The S_{21} response of the MMG30XX amplifier circuit (without the resonator) at RF Power of -10 dBm.

52
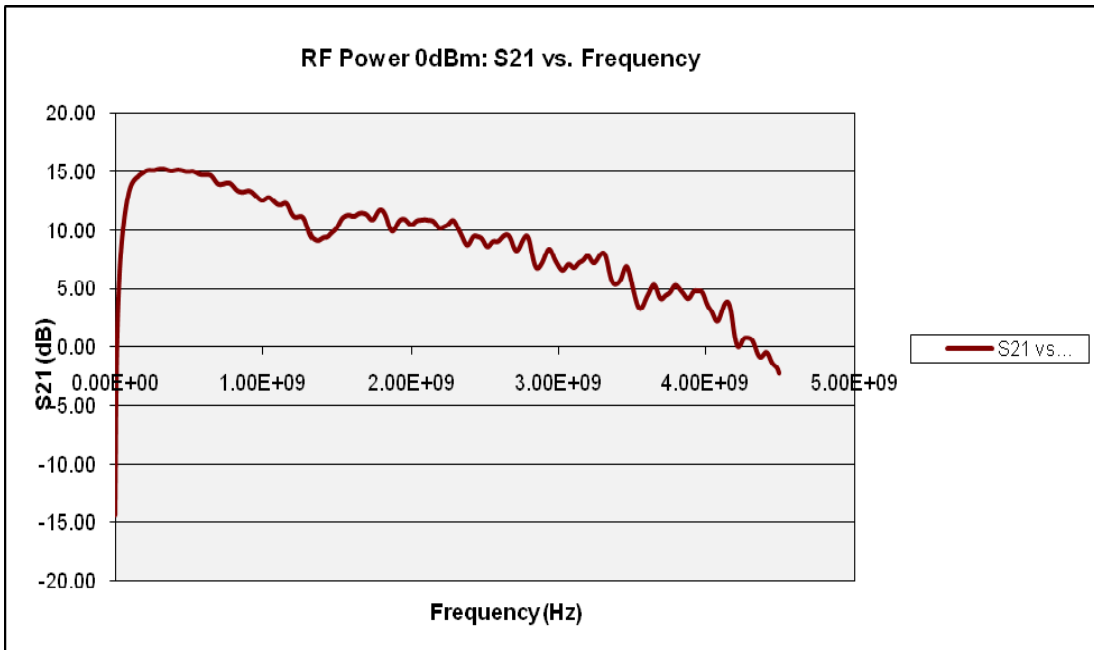
Figure 4.14 The S_{21} response of the MMG30XX amplifier circuit (without the resonator) at RF Power of 0 dBm.
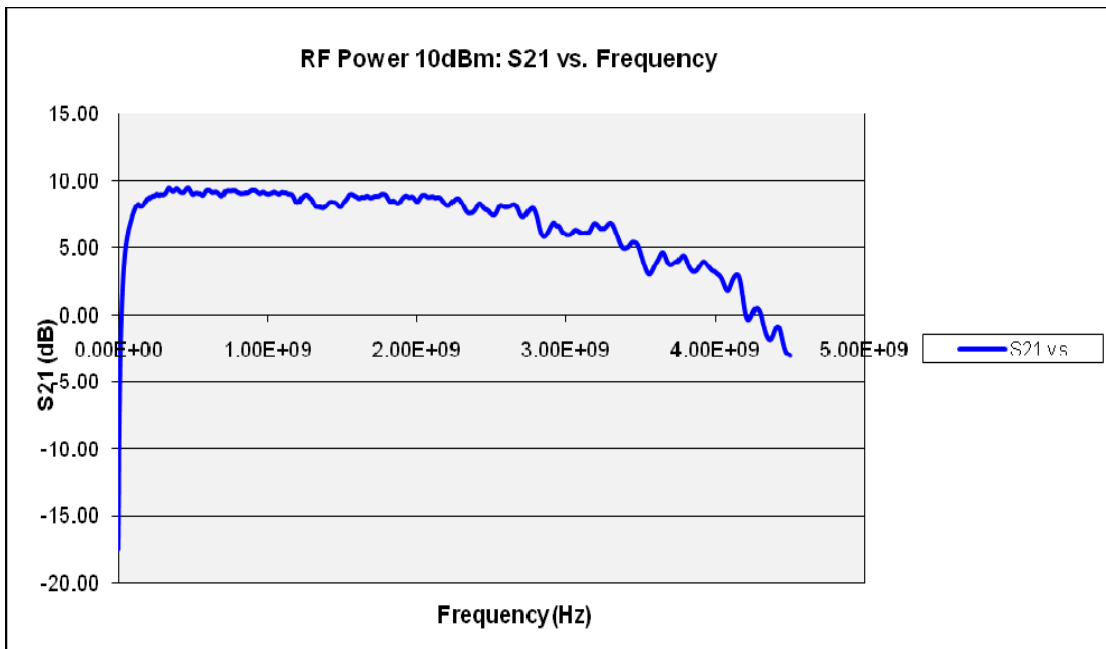
Figure 4.15 The S_{21} response of the MMG30XX amplifier circuit (without the resonator) at RF Power of +10dBm.

The S_{21} has a significant high value of +15 dB at an RF Power of 0dBm and slightly more than +15 dB for an RF Power of -10 dBm, and around +10 dB for an RF Power of +10dBm. These S_{21} values of the amplifier closely matched with the datasheet values which verified that the circuit was built correctly. Figure 4.16 shows the S_{21}, S_{11} and S_{22} responses of the amplifier obtained from the datasheet.
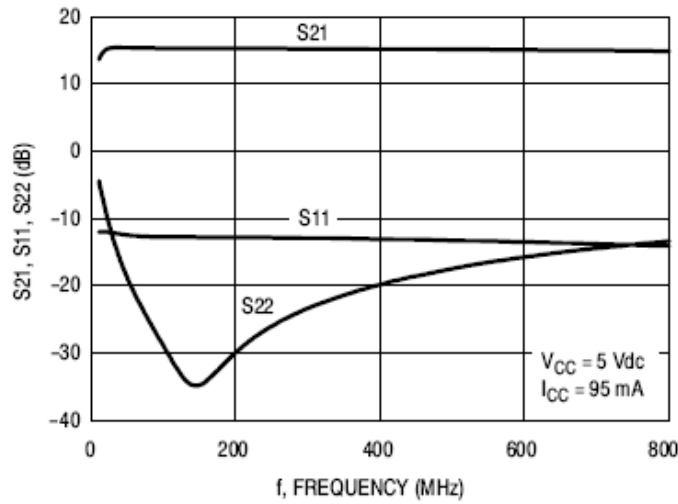
Figure 4.16 The S_{21}, S_{11} and S_{22} responses of the amplifier obtained from the datasheet. [65]

With microelectronic devices, any small electrostatic charge flow can cause malfunctioning of the components. Therefore, it was vital to wear the grounding strap while handling the board and soldering any components to the board to eliminate any such electrostatic leakage that might damage the RF amplifier as well as the resonator.

4.5.1 ADS Simulation after Adding a Basic Single Stage BJT Amplifier

Before building the amplifier circuit, the concept was implemented in ADS to ensure that the resonant frequency can be achieved when an amplifier is used with the resonator model (Figure 4.5 from Sec 4.2). A basic single stage bipolar junction transistor circuit was used as the amplifier stage as shown in Figure 4.17 (a). The S_{21} response obtained by simulating this model (with 10 MHz resonator) is shown in Figure 4.17 (b).
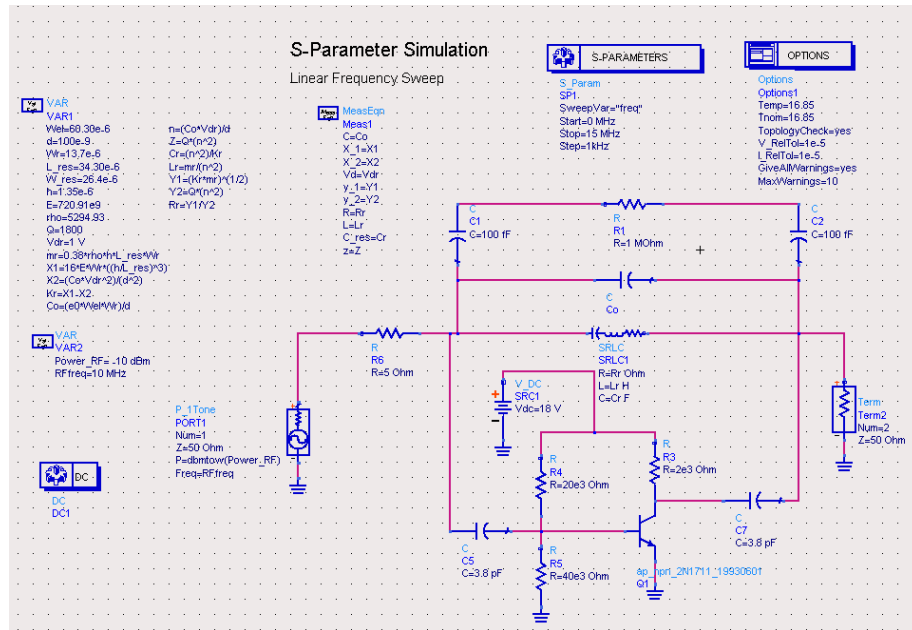
(a)
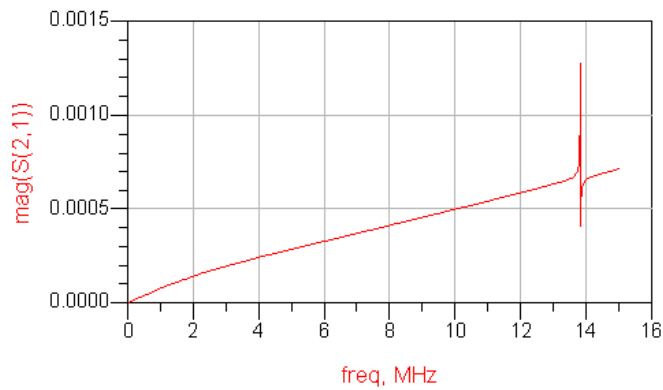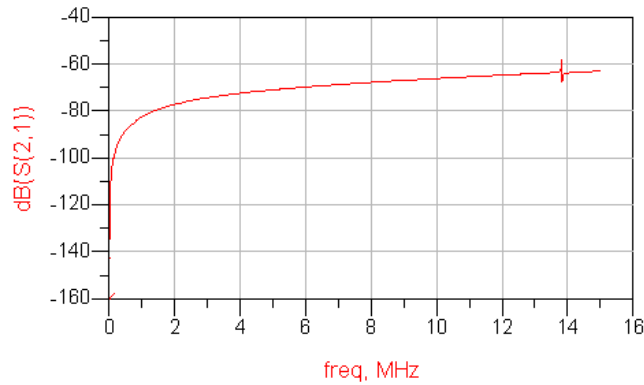
(b)

Figure 4.17 The modified resonator model with the BJT amplifier stage. (a) The circuit schematic, and (b) the simulated S_{21} response of the 10 MHz) resonator in ADS.

55

As predicted, the resonant frequency occurred at around the same frequency as before. From Figure 4.17 (b), it can be inferred that the resonant frequency of a 10 MHZ resonator to be around 13.9 MHz, which is very close to the previous results obtained in Section 4.2.

4.5.2 MMG30XX Circuit Board with Resonator

The MMG30XX amplifier circuit board was built using the heterojunction bipolar transistor MMG3015NT1, four capacitors and an inductor. The values of the capacitors and inductor were extracted from the amplifier datasheet. These RF components were soldered to the board before the resonator die was attached to the board. The resonator die was glued to the PCB board similar to what was described in Section 4.2. The resonator to be characterized was tested using the same methodology as before. The selected resonator was then wire bonded to the RF input and output terminals of the amplifier circuit board. Figure 4.18 shows the MMG30XX PCB without any components and with the built amplifier circuit.
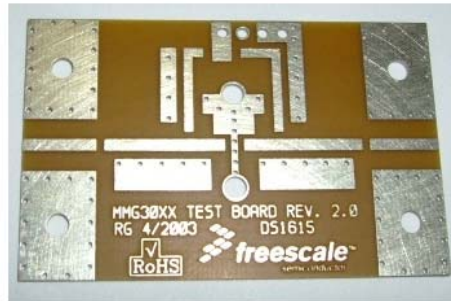
(a)
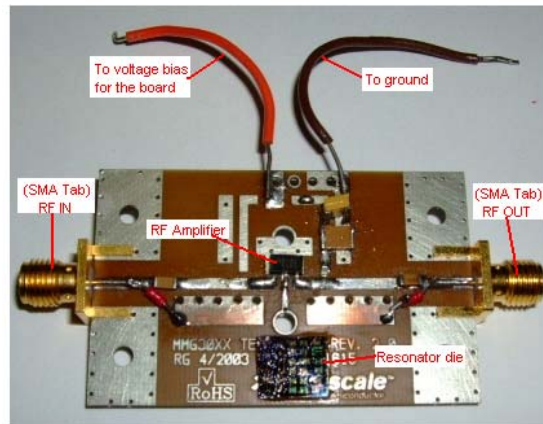
(b)

Figure 4.18 The MMG30XX PCB board. (a) without any components, and (b) with the built amplifier circuit including the RF components and the resonator.

4.5.3 Simulations from the Network Analyzer

After the pull down or collapse voltages were measured using the probing station, the circuit model described in the last section (Section 4.5.2) was characterized using the Agilent Network Analyzer, similar to what was described in Section 4.2.. The measurement results showed much improved S_{21} and Q-factor values, which implied that the loading of the components and also the insertion loss were reduced considerably.

4.5.3.1 Improved S_{21} Response of the Resonator Model

Figure 4.19 shows the S_{21} response of a 10 MHz resonator model with the amplifier circuitry. It can be seen that there is a prominent resonant frequency occurring at around 6.15 MHz, which is very close to the measured value (between 4.6 and 6 MHz) of the resonator without the amplifier circuitry. The remarkable aspect in this case is the improved value for the S_{21} parameter. In this case, the S_{21} values ranged between positive 10 and 25 dB, which is a significant improvement to the typical low measured values ranging from -40 to -60 dB for the resonators without the amplifier circuit. Since S_{21} is a measure of the output power to the input power, a higher value of S_{21} implies a much better gain of the device, indicating better performance. The Q-factor was also measured and found to be around 153, which is much improved over the Q's found in these resonators. Resonators (without amplifier circuitry) usually showed a very low Q between 7 and 50. Higher Q implies there is less insertion loss, again leading to better performance.
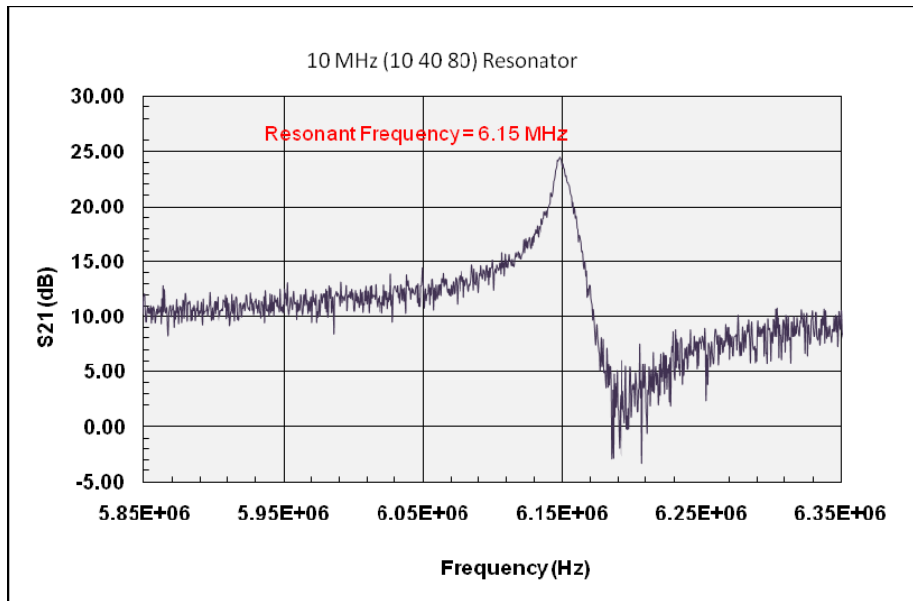
Figure 4.19 The S_{21} response of a 10 MHz resonator model with the amplifier circuit.

Figure 4.20 shows the S_{21} behavior of a similar 10 MHz resonator (when the amplifier circuitry is not present). The resonance occurred around the same value (6.37 MHZ) but was not very significant. The S_{21} value here is about -60 dB. The Q-factor in this case was found to be around 15. Both the values of S_{21} and Q are very low, because of the increased loading of the resonator without the amplifier.
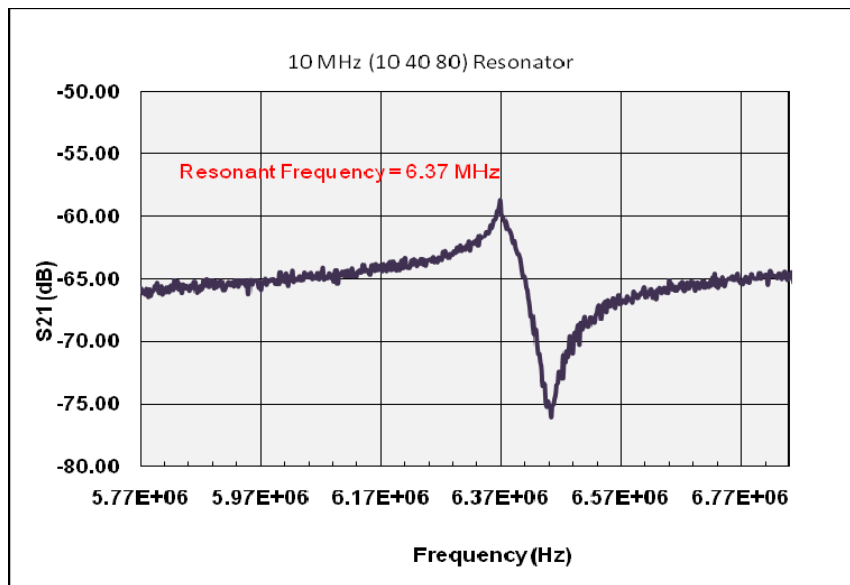
Figure 4.20 The S_{21} response of a 10 MHz resonator (when the amplifier is off).

58

4.5.3.2 Softening Effect of the Resonator Model

       Table 4.4 shows the resonant frequency values obtained by varying the bias voltage. The graphical representation of this table is shown in Figure 4.21. The resonant frequency decreases with increasing bias voltage, demonstrating the softening effect of the resonator model. The shape of the graph is slightly different from what was seen before (Figure 4.8 in Section 4.2). This could have been caused by the additional non-linearities formed due to the RF components in the amplifier circuit. However, this aspect should be investigated further so that the softening effect can be utilized for frequency tuning of the resonator.

Table 4.4 The resonant frequency values with varying bias voltage.

Voltage Bias (V)	Resonant Frequency (MHz)
5.55	6.15
4.35	6.24
3.15	6.33
2.25	6.44
1.28	6.62
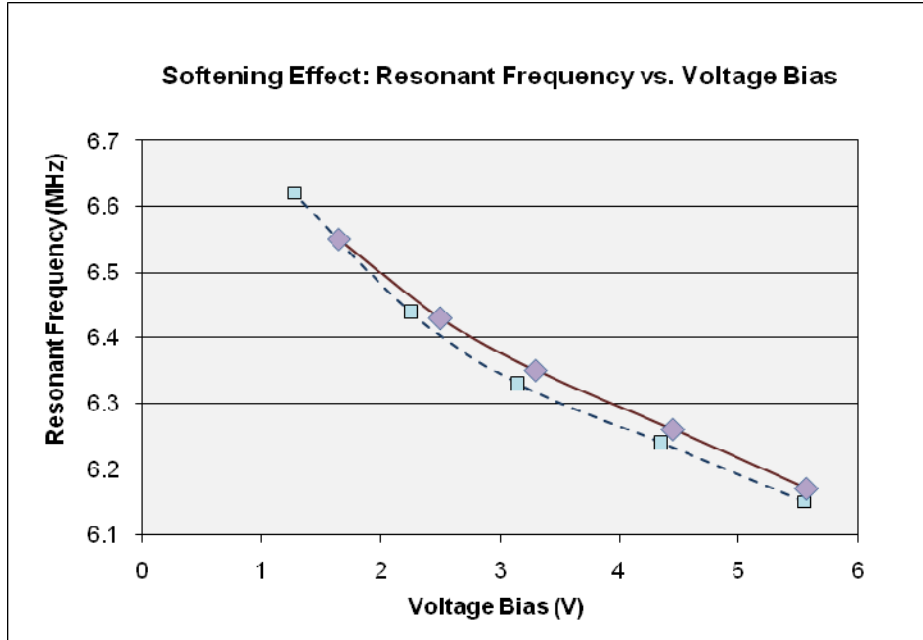
Figure 4.21 The softening effect. The resonant frequency response with varying bias voltage. (The solid line denotes the simulated results and the dotted line denotes the experimental results).

For the low frequency resonators, typical softening behavior resembles the one shown in Figure 4.8 in Section 4.2 However, for the higher frequency resonators (10 MHZ and above), the softening behavior looked similar to the one shown in Figure 4.21.

In general, the resonant frequency should decrease with increasing bias voltage to demonstrate the spring softening effect. The results from my characterization illustrate this clearly as can be seen in Figure 4.18. The spring softening effect occurs because the overall spring stiffness coefficient of the device decreases with the increasing bias voltage. This decrease is initiated when the resonator exhibits a restoring force equal but opposite to the direction of the electrostatic force from the bias voltage. [1]

This spring softening behavior can be exploited as a frequency tuning capability in several applications. The dc voltage tunability of a MEMS resonator can be used in tunable MEMS filters and mixers, in fine-tuning the frequency of the MEMS that compensates for the manufacturing or fabrication variations, and also to introduce ambient/operating temperature compensation on resonators for oscillation applications. [1] [8]

CHAPTER 5

SUMMARY AND CONCLUSION

5.1 Analysis and Discussion

In this thesis, the various factors related to mechanical failure were investigated. Constructing a complete solution of the resonator model helped to understand the linear as well as the non-linear model. The non-linear softening was directly related to the stiffness factor. The even powers of the stiffness coefficient contributed to the stiffness factor where as the odd powers of stiffness coefficient had little effect on the stiffness factor, and could be assumed to be zero. This also implies that the mechanical stiffness function is symmetric about x = 0. [1] [8] The decrease in the overall spring constant of the device is caused by the restoring force that is equal but opposite to direction of the force from the electrostatic field of the drive bias voltage. Using the MMG30XX amplifier circuitry in conjunction with the resonator has shown significant improvement in the performance of the resonator, which in turn improves the reliability of the RF MEMS devices.

The initial ADS model of resonator described in Section 4.2 showed that the simulated results from the circuit resonator model matched closely with the experimental values. The spring softening response was also very significant with varying dc bias voltage as shown in Figure 4.8. The equations and parameter values used for this model were extracted from the articles discussed in Sections 3.1 and 3.2. The S_{21} value for this model was about -43 dB, which fell in the typical measured S_{21} range (-60 to -40) shown by earlier experiments.

In order to achieve a more accurate representation of the resonator, a mechanical model was numerically derived (shown in Appendix A) and implemented using MathCAD as discussed in Sections 4.3 and 4.4. The results from the MathCAD simulations show traces of non-linear harmonics arising with increasing dc bias voltage. These non-linear harmonics might

have been initiated by the circuit parasitic elements that arise from the RF components (inductors and capacitors) when operating at high frequencies. A very prominent resonance with no harmonics was observed when the bias voltages were kept at 1 V. The S_{21} value was found to be about -38.5 dB, which was close to the ADS simulation results in Section 4.2 as well as the experimentally measured values (usually between -70 and -40 dB). This numerical model can be further tweaked to provide better results that will yield an adequate estimate of the performance of fabricated devices. In fact, this method can be extended to other types of MEMS resonator models, and is not limited to just the clamped-clamped resonator model.

Section 4.5 focused on the improvement of the resonator model performance in terms of RF response S_{21} and quality factor. The MMG30XX amplifier circuit demonstrated a high S_{21} response of about positive 15 dB at 0 dBm RF power, which matched with the datasheet values and provided an attractive solution to improve the S_{21} and Q-factor of the resonator. The circuit model, built by integrating this amplifier circuit with the resonator, indeed demonstrated a considerable improvement in both parameters. The S_{21} ranged from positive 15 dB to 25 dB and the Q-factor was found to be about 150. In typical experiments without the amplifier circuit, the S_{21} was always in the negative decibel region and the Q-factor was between 7 and 50. The S_{21} values extracted from this model exhibited a huge improvement from the earlier measured values. On the other hand, the Q-factor, though much improved, was not as high as desired. However, this method certainly presents a novel way of improving these performance criteria holding the great potential for further thorough research.

CAD simulations using software tools like Agilent ADS (Advanced Design Simulator), Cadence Virtuoso Spectre or Microwave Office allow all relevant impact and device parameters, including the bias, element values, frequencies, stimuli power and temperature to be swept, tuned and optimized. Even though the optimization routines are very effective to get the maximum performance out of any design, most of the gradient optimization techniques are suitable and accurate if the characteristics are monotone. However, in reality, this is not usually

the case and this is the reason why in many cases the simulation results may not accurately match the measured parameter values. As a simple example, it has been seen in many cases that the S-parameters extracted from the ADS simulation may not match the ones measured using an Agilent network analyzer. Therefore, despite the availability of design software tools, a professional designer should be required to have thorough knowledge of circuit design practices. Often this knowledge is acquired via industry experience rather than solely studying the theory. It is vital that the designer understand the various trade-offs between the many parameters such as gain, noise, power consumption, and stability in order to design the amplifier circuit specific to the desired application. [26]

5.2 Conclusion

This paper illustrated some strategies for modeling the complete dynamics of an RF MEMS resonator and discusses some prospective ways of improving the performance of such devices without affecting the functionality of the underlying RF components. Integration of the amplifier circuitry with the resonator model holds a lot of future potential and should be thoroughly investigated to test for long-term reliability. Detailed analysis of the non-linear softening behavior should also be further performed to investigate the possibilities of further utilizing this behavior in the frequency tuning of RF devices and other RF applications.

Though some aspects of the mechanical behavior of the RF MEMS resonator were investigated in this paper, there are many other aspects that were not analyzed. Thus, the yearnings for better and improved RF MEMS resonator designs continue to pave the groundwork for further future research.

APPENDIX A

DERIVATION FOR THE COMPLETE MECHANICAL MODEL OF
THE CLAMPED-CLAMPED RESONATOR

Derivation for the complete mechanical model of the clamped-clamped Resonator
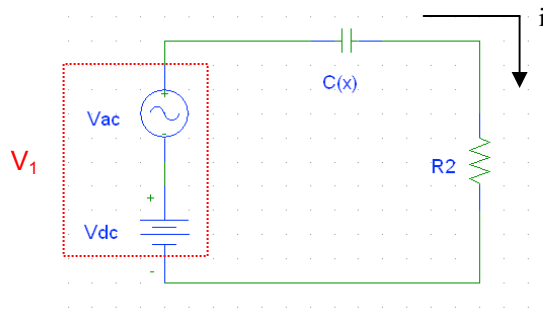
$$V_1 = V_{dc} + V_{ac} \cdot \sin\omega t \qquad ---1$$

$$C(x) = \frac{C_0 \cdot d_0}{d_0 + x} \qquad ---2$$

$$\frac{\delta C(x)}{\delta x} = \frac{-C_0 \cdot d_0}{(d_0 + x)^2} \qquad ---3$$

$$\frac{dC(x)}{dt} = \frac{\delta C(x)}{\delta x} \cdot \overset{-}{x} \qquad ---5^4$$

$$V_{res} = V_1 - R_2 \cdot i$$

$$i = C(x) \cdot \frac{dV_1}{dt} + V_{res} \cdot \frac{dC(x)}{dt} \qquad ---6$$

$$\text{or, } i = C(x) \cdot \left(\frac{dv_1}{dt} - R_2 \cdot \frac{di}{dt} \right) + V_{res} \cdot \frac{\delta C(x)}{\delta x} \cdot \frac{dx}{dt}$$

$$\text{or, } i = C(x) \cdot \frac{dv_1}{dt} - C(x) \cdot R_2 \cdot \frac{di}{dt} + V_{res} \cdot \frac{\delta C(x)}{\delta x} \cdot \frac{dx}{dt}$$

$$\text{or, } \frac{di}{dt} = \frac{C(x)}{C(x) \cdot R_2} \cdot \frac{dV_1}{dt} + \frac{V_{res}}{C(x) \cdot R_2} \cdot \frac{\delta C(x)}{\delta x} \cdot \frac{dx}{dt} - \frac{i}{C(x) \cdot R_2} \qquad ---7$$

From equation 1, we know that, $\quad V_1 = V_{dc} + V_{ac} \cdot \sin\omega t$

$$\text{Therefore, } \frac{dV_1}{dt} = \omega \cdot V_{ac} \cdot \cos\omega t \qquad ---8$$

65

Using equations 1,2,3,5 and 8 in equation 7, we get,

$$\frac{di}{dt} = \frac{1}{R_2} \cdot \omega \cdot V_{ac} \cdot \cos\omega t + \frac{V_1 - R_2 \cdot i}{C(x) \cdot R_2} \cdot \frac{-C_0 \cdot d_0}{\left(d_0 + x\right)^2} \cdot \overline{x} - \frac{i}{C(x) \cdot R_2}$$

$$\text{or,} \ \frac{di}{dt} = \frac{1}{R_2} \cdot \omega V_{ac} \cdot \cos\omega t + \frac{V_{dc} + V_{ac} \cdot \sin\omega t - R_2 \cdot i}{\left(\dfrac{C_0 \cdot d_0}{d_0 + x}\right) \cdot R_2} \cdot \frac{-C_0 \cdot d_0}{\left(d_0 + x\right)^2} \cdot \overline{x} - \frac{i}{\left(\dfrac{C_0 \cdot d_0}{d_0 + x}\right) \cdot R_2}$$

$$\text{or,} \ \frac{di}{dt} = \frac{1}{R_2} \cdot \omega \cdot V_{ac} \cdot \cos\omega wt + \frac{V_{dc} \cdot \left(d_0 + x\right) + V_{ac} \cdot \sin\omega t - R_2 \cdot i}{C_0 \cdot d_0 \cdot R_2} \cdot \frac{-C_0 \cdot d_0}{\left(d_0 + x\right)^2} \cdot \overline{x} - \frac{i \cdot \left(d_0 + x\right)}{C_0 \cdot d_0 \cdot R_2}$$

$$\text{or,} \ \frac{di}{dt} = \frac{1}{R_2}\left[\omega \cdot V_{ac}\cos\omega t - \frac{\left(V_{dc} + V_{ac}\sin\omega t - R_2 \cdot i\right) \cdot \overline{x}}{d_0 + x} - \frac{\left(d_0 + x\right)}{c_0 \cdot d_0} \cdot i \right] \qquad ---9$$

The dynamic behavior of the flexural displacement of a beam resonaror is given by:

$$m \cdot \overline{\overline{x}} + b \cdot \overline{x} + k(x) \cdot x = F_e(x) \qquad ---10$$

Therefore, $\overline{\overline{x}} = \dfrac{1}{m} \cdot \left(F_e(x) - b \cdot \overline{x} - k(x) \cdot x\right) \qquad ---11$

Electrostatic force F(x,t) is given by:

$$F_e(x,t) = \frac{1}{2} \cdot \frac{C_0 \cdot d_0}{\left(d_0 - x\right)^2} \cdot V_1(t)^2 - \frac{1}{2} \cdot \frac{C_0 \cdot d_0}{\left(d_0 + x\right)^2} \cdot V_2^{\ 2} \qquad ---12$$

where C_0 is the gap capacitance when x = 0,

d_0 is the corresponding initial gap width

$V_1(t)$ and V_2 denote the applied voltages on the electrodes.

66

From equation 1, we already know that $V_1(t) = V_{dc} + V_{ac}\sin\omega t$

$$V_2 = V_{dc} \qquad ---13$$

where V_{dc} is the dc bias voltage

V_{ac} is the amplitude of the ac bias voltage

$\omega = 2\cdot\pi\cdot f$ where f is the frequency of the ac voltage

Capacitance on the readout side for an arbitrary x is given by equation 2.

Substituting the expressions of V_1 and V_2 from equations 1 and 13 into equation 12,

$$F_e(x,t) = \frac{1}{2}\cdot\frac{C_0\cdot d_0}{(d_0 - x)^2}\cdot(V_{dc} + V_{ac}\cdot\sin\omega t)^2 - \frac{1}{2}\cdot\frac{C_0\cdot d_0}{(d_0 + x)^2}\cdot V_{dc}^2$$

$$\text{or, } F_e(x,t) = \frac{1}{2}\cdot\frac{C_0\cdot d_0}{(d_0 - x)^2}\cdot\left(V_{dc}^2 + V_{ac}^2\cdot\sin\omega t^2 + 2\cdot V_{dc}\cdot V_{ac}\cdot\sin\omega t\right) - \frac{1}{2}\cdot\frac{C_0\cdot d_0}{(d_0 + x)^2}\cdot V_{dc}^2$$

$$\text{or, } F_e(x,t) = \frac{1}{2}\cdot\frac{C_0\cdot d_0}{d_0^2\cdot\left(1 - \dfrac{x}{d_0}\right)^2}\cdot\left(V_{dc}^2 + V_{ac}^2\cdot\sin\omega t^2 + 2\cdot V_{dc}\cdot V_{ac}\cdot\sin\omega t\right) - \frac{1}{2}\cdot\frac{C_0\cdot d_0}{d_0^2\cdot\left(1 + \dfrac{x}{d_0}\right)^2}\cdot V_{dc}^2$$

$$\text{or, } \frac{1}{2}\cdot\frac{C_0}{d_0\cdot\left(1 - \dfrac{x}{d_0}\right)^2}\cdot V_{dc}^2 + \frac{1}{2}\cdot\frac{C_0}{d_0\cdot\left(1 - \dfrac{x}{d_0}\right)^2}\cdot\left(V_{ac}^2\cdot\sin\omega t^2 + 2\cdot V_{dc}\cdot V_{ac}\cdot\sin\omega t\right) - \frac{1}{2}\cdot\frac{C_0}{d_0\cdot\left(1 + \dfrac{x}{d_0}\right)^2}\cdot V_{dc}^2$$

$$\text{or, } \frac{1}{2}\cdot\frac{C_0}{d_0}\cdot V_{dc}^2\cdot\left(\frac{1}{\left(1 - \dfrac{x}{d_0}\right)^2} - \frac{1}{\left(1 + \dfrac{x}{d_0}\right)^2}\right) + \frac{1}{2}\cdot\frac{C_0}{d_0}\cdot\frac{1}{\left(1 - \dfrac{x}{d_0}\right)^2}\cdot\left(V_{ac}^2\cdot\sin\omega t^2 + 2\cdot V_{dc}\cdot V_{ac}\cdot\sin\omega t\right)$$

$$---14$$

Taylor Series Expansion is defined by:

$$f(x) = f(a) = \left[f^{(1)}(a)(x-a) + \frac{f^{(2)}(a)}{2!} \cdot (x-a)^2 + \frac{f^{(3)}(a)}{3!} \cdot (x-a)^3 + ...\ \frac{f^{(n)}(a)}{n!} \cdot (x-a)^n \right]$$

$$---15$$

Taylor Expansion of $\dfrac{1}{\left(1 + \dfrac{x}{d_0}\right)^2}$:

$$\frac{1}{\left(1 + \dfrac{x}{d_0}\right)^2} = \frac{1}{(1+y)^2} = \frac{1}{(1+a)^2} + 2 \cdot \frac{(y-a)}{(1+a)^3} + \frac{6}{2!} \cdot \frac{(y-a)^2}{(1+a)^4} + \frac{24}{3!} \cdot \frac{(y-a)^3}{(1+a)^5} + \frac{120}{4!} \cdot \frac{(y-a)^4}{(1+a)^6} + \frac{720}{5!} \cdot \frac{(y-a)^5}{(1+a)^7}$$

or, $\dfrac{1}{(1+y)^2} = \dfrac{1}{(1+a)^2} - 2 \cdot \dfrac{(y-a)}{(1+a)^3} + \dfrac{6}{2!} \cdot \dfrac{(y-a)^2}{(1+a)^4} - \dfrac{24}{3!} \cdot \dfrac{(y-a)^3}{(1+a)^5} + \dfrac{120}{4!} \cdot \dfrac{(y-a)^4}{(1+a)^6} - \dfrac{720}{5!} \cdot \dfrac{(y-a)^5}{(1+a)^7}$

When a = 0,

$$\frac{1}{(1+y)^2} = 1 - 2y + 3 \cdot y^2 - 4 \cdot y^3 + 5 \cdot y^4 - 6 \cdot y^{5.} + ...$$

Therefore

$$\frac{1}{\left(1 + \dfrac{x}{d_0}\right)^2} = 1 - 2 \cdot \frac{x}{d_0} + 3 \cdot \frac{x^2}{d_0^2} - 4 \cdot \frac{x^3}{d_0^3} + \frac{5 \cdot x^4}{d_0^4} - 6 \cdot \frac{x^5}{d_0^5} + ...$$

$$---17$$

Using the expressions in (16) and (17), we get,

$$\frac{1}{\left(1 - \dfrac{x}{d_0}\right)^2} - \frac{1}{\left(1 + \dfrac{x}{d_0}\right)^2} = 1 + 2 \cdot \frac{x}{d_0} + 3 \cdot \frac{x^2}{d_0^2} + 4 \cdot \frac{x^3}{d_0^3} + \frac{5 \cdot x^4}{d_0^4} + 6 \cdot \frac{x^5}{d_0^5} + ...$$

$$- \left(1 - 2 \cdot \frac{x}{d_0} + 3 \cdot \frac{x^2}{d_0^2} - 4 \cdot \frac{x^3}{d_0^3} + \frac{5 \cdot x^4}{d_0^4} - 6 \cdot \frac{x^5}{d_0^5} + ... \right)$$

68

Therefore, $\dfrac{1}{\left(1 - \dfrac{x}{d_0}\right)^2} - \dfrac{1}{\left(1 + \dfrac{x}{d_0}\right)^2} = 4\cdot\dfrac{x}{d_0} + \dfrac{8\cdot x^3}{d_0^3} + \dfrac{12\cdot x^3}{d_0^5} + ...$ $\quad\quad - - - 18$

Substituting (16) and (18) into (14), we get,

$$F_e(x,t) = \frac{1}{2}\cdot\frac{C_0}{d_0}\cdot V_{dc}^2\cdot\left(4\cdot\frac{x}{d_0} + \frac{8\cdot x^3}{d_0^3} + \frac{12\cdot x^3}{d_0^5}\right) + ...$$

$$... + \frac{1}{2}\cdot\frac{C_0}{d_0}\cdot\left(V_{ac}^2\cdot\sin\omega t^2 + 2\cdot V_{dc}\cdot V_{ac}\cdot\sin\omega t\right)\cdot\left(1 + 2\cdot\frac{x}{d_0} + 3\cdot\frac{x^2}{d_0^2} + 4\cdot\frac{x^3}{d_0^3} + \frac{5\cdot x^4}{d_0^4} + 6\cdot\frac{x^5}{d_0^5} + ...\right)$$

$$- - - 19$$

Rearranging (19) and taking terms upto the 5th order,

$$F_e(x,t) = 2\cdot\frac{C_0}{d_0^2}\cdot V_{dc}^2 + 4\cdot\frac{C_0}{d_0^4}\cdot V_{dc}^2\cdot x^3 + 6\cdot\frac{C_0}{d_0^6}\cdot V_{dc}^2\cdot x^5 + \frac{C_0}{d_0}\left(\frac{1}{2}\cdot V_{ac}^2\cdot\sin\omega t^2 + 2\cdot V_{dc}\cdot V_{ac}\cdot\sin\omega t\right)$$

$$... + 2\cdot\frac{C_0\cdot x}{d_0^2}\cdot\left(\frac{1}{2}\cdot V_{ac}^2\cdot\sin\omega t^2 + V_{dc}\cdot V_{ac}\cdot\sin\omega t\right)$$

$$... + 3\cdot\frac{C_0\cdot x^2}{d_0^3}\cdot\left(\frac{1}{2}\cdot V_{ac}^2\cdot\sin\omega t^2 + V_{dc}\cdot V_{ac}\cdot\sin\omega t\right)$$

$$... + 4\cdot\frac{C_0\cdot x^3}{d_0^4}\cdot\left(\frac{1}{2}\cdot V_{ac}^2\cdot\sin\omega t^2 + V_{dc}\cdot V_{ac}\cdot\sin\omega t\right)$$

$$... + 5\cdot\frac{C_0\cdot x^4}{d_0^5}\cdot\left(\frac{1}{2}\cdot V_{ac}^2\cdot\sin\omega t^2 + V_{dc}\cdot V_{ac}\cdot\sin\omega t\right)$$

$$... + 6\cdot\frac{C_0\cdot x^5}{d_0^6}\cdot\left(\frac{1}{2}\cdot V_{ac}^2\cdot\sin\omega t^2 + V_{dc}\cdot V_{ac}\cdot\sin\omega t\right) \quad\quad - - - 20$$

Mechanical stiffness function k(x) is defined by:

$$k(x) = k_0 + k_1 \cdot x + k_2 \cdot x^2 + k_3 \cdot x^3 + k_4 \cdot x^4 + \ldots \qquad ---21$$

Substituting (21) into the expression in (10), we get,

$$m \cdot \overset{=}{x} + b \cdot \overset{-}{x} + \left(k_0 + k_1 \cdot x + k_2 \cdot x^2 + k_3 \cdot x^3 + k_4 \cdot x^4 + \ldots \right) \cdot x = F_e(x) \qquad ---22$$

Now, substituting the expression for $F_e(x, t)$ from (20) into (22), we get,

$$m \cdot \overset{=}{x} + b \cdot \overset{-}{x} + \left(k_0 + k_1 \cdot x + k_2 \cdot x^2 + k_3 \cdot x^3 + k_4 \cdot x^4 + \ldots \right) \cdot x$$

$$\ldots = 2 \cdot \frac{C_0}{d_0^2} \cdot V_{dc}^2 + 4 \cdot \frac{C_0}{d_0^4} \cdot V_{dc}^2 \cdot x^3 + 6 \cdot \frac{C_0}{d_0^6} \cdot V_{dc}^2 \cdot x^5 + \frac{C_0}{d_0} \left(\frac{1}{2} \cdot V_{ac}^2 \cdot \sin\omega t^2 + 2 \cdot V_{dc} \cdot V_{ac} \cdot \sin\omega t \right)$$

$$\ldots + 2 \cdot \frac{C_0 \cdot x}{d_0^2} \cdot \left(\frac{1}{2} \cdot V_{ac}^2 \cdot \sin\omega t^2 + V_{dc} \cdot V_{ac} \cdot \sin\omega t \right)$$

$$\ldots + 3 \cdot \frac{C_0 \cdot x^2}{d_0^3} \cdot \left(\frac{1}{2} \cdot V_{ac}^2 \cdot \sin\omega t^2 + V_{dc} \cdot V_{ac} \cdot \sin\omega t \right)$$

$$\ldots + 4 \cdot \frac{C_0 \cdot x^3}{d_0^4} \cdot \left(\frac{1}{2} \cdot V_{ac}^2 \cdot \sin\omega t^2 + V_{dc} \cdot V_{ac} \cdot \sin\omega t \right)$$

$$\ldots + 5 \cdot \frac{C_0 \cdot x^4}{d_0^5} \cdot \left(\frac{1}{2} \cdot V_{ac}^2 \cdot \sin\omega t^2 + V_{dc} \cdot V_{ac} \cdot \sin\omega t \right)$$

$$\ldots + 6 \cdot \frac{C_0 \cdot x^5}{d_0^6} \cdot \left(\frac{1}{2} \cdot V_{ac}^2 \cdot \sin\omega t^2 + V_{dc} \cdot V_{ac} \cdot \sin\omega t \right)$$

$$---23$$

Comparing and rearranging terms containing up to 5th order in (23),

$$m \cdot \ddot{x} + b \cdot \dot{x} + x \cdot \left[k_0 - 2 \cdot \frac{C_0}{d_0^2} \cdot V_{dc}^2 - 2 \cdot \frac{C_0 \cdot x}{d_0^2} \cdot \left(\frac{1}{2} \cdot V_{ac}^2 \cdot \sin \omega t^2 + V_{dc} \cdot V_{ac} \cdot \sin \omega t \right) \right]$$

$$\ldots + x^2 \left[k_1 - 3 \cdot \frac{C_0}{d_0^3} \cdot \left(\frac{1}{2} \cdot V_{ac}^2 \cdot \sin \omega t^2 + V_{dc} \cdot V_{ac} \cdot \sin \omega t \right) \right]$$

$$\ldots + x^3 \cdot \left[k_2 - 4 \cdot \frac{C_0}{d_0^4} \cdot V_{dc}^2 - 4 \cdot \frac{C_0 \cdot x^3}{d_0^4} \cdot \left(\frac{1}{2} \cdot V_{ac}^2 \cdot \sin \omega t^2 + V_{dc} \cdot V_{ac} \cdot \sin \omega t \right) \right]$$

$$\ldots + x^4 \cdot \left[k_3 - 5 \cdot \frac{C_0}{d_0^5} \cdot \left(\frac{1}{2} \cdot V_{ac}^2 \cdot \sin \omega t^2 + V_{dc} \cdot V_{ac} \cdot \sin \omega t \right) \right]$$

$$\ldots + x^5 \cdot \left[k_4 - 6 \cdot \frac{C_0}{d_0^6} \cdot V_{dc}^2 - 6 \cdot \frac{C_0 \cdot x^5}{d_0^6} \cdot \left(\frac{1}{2} \cdot V_{ac}^2 \cdot \sin \omega t^2 + V_{dc} \cdot V_{ac} \cdot \sin \omega t \right) \right]$$

$$\ldots = \frac{C_0}{d_0} \left(\frac{1}{2} \cdot V_{ac}^2 \cdot \sin \omega t^2 + V_{dc} \cdot V_{ac} \cdot \sin \omega t \right) = \frac{C_0}{d_0} \cdot V_{dc} \left(\frac{1}{2} \cdot \frac{V_{ac}^2}{V_{dc}} \cdot \sin \omega t^2 + V_{ac} \cdot \sin \omega t \right)$$

$$- - -24$$

Therefore, from (24) the **modified stiffness factor** $K_e(x)$ is:

$$K_e(x) = k_0 - 2 \cdot \frac{C_0}{d_0^2} \cdot V_{dc}^2 - 2 \cdot \frac{C_0 \cdot x}{d_0^2} \cdot \left(\frac{1}{2} \cdot V_{ac}^2 \cdot \sin \omega t^2 + V_{dc} \cdot V_{ac} \cdot \sin \omega t \right)$$

$$\ldots + \left[k_1 - 3 \cdot \frac{C_0}{d_0^3} \cdot \left(\frac{1}{2} \cdot V_{ac}^2 \cdot \sin \omega t^2 + V_{dc} \cdot V_{ac} \cdot \sin \omega t \right) \right]$$

$$\ldots + \left[k_2 - 4 \cdot \frac{C_0}{d_0^4} \cdot V_{dc}^2 - 4 \cdot \frac{C_0 \cdot x^3}{d_0^4} \cdot \left(\frac{1}{2} \cdot V_{ac}^2 \cdot \sin \omega t^2 + V_{dc} \cdot V_{ac} \cdot \sin \omega t \right) \right]$$

$$\ldots + \left[k_3 - 5 \cdot \frac{C_0}{d_0^5} \cdot \left(\frac{1}{2} \cdot V_{ac}^2 \cdot \sin \omega t^2 + V_{dc} \cdot V_{ac} \cdot \sin \omega t \right) \right]$$

$$\ldots + \left[k_4 - 6 \cdot \frac{C_0}{d_0^6} \cdot V_{dc}^2 - 6 \cdot \frac{C_0 \cdot x^5}{d_0^6} \cdot \left(\frac{1}{2} \cdot V_{ac}^2 \cdot \sin \omega t^2 + V_{dc} \cdot V_{ac} \cdot \sin \omega t \right) \right]$$

$$- - -25$$

For the complete numerical model, the following variables will be used:

Displacement $\quad x = x_1 \qquad ---26$

Velocity $\qquad \bar{x} = x_2 \qquad ---27$

Current $\qquad i = x_3 \qquad ---28$

Using equations (9),(11) and (27), the complete model can be represented in matrix format:

$$
f(x,t) = \begin{bmatrix} (27) \\ (11) \\ (9) \end{bmatrix} = \begin{bmatrix} x_2 \\ \dfrac{1}{m} \cdot \left(F_e(x,t) - b \cdot \bar{x} - k(x,t) \cdot x \right) \\ \dfrac{1}{R_2}\left[\omega \cdot V_{ac} \cos \omega t - \dfrac{\left(V_{dc} + V_{ac}\sin \omega t - R_2 \cdot i\right) \cdot \bar{x}}{d_0 + x} - \dfrac{\left(d_0 + x\right)}{c_0 \cdot d_0} \cdot i \right] \end{bmatrix}
$$

The terms $F_e(x,t)$ and $k(x,t)$ are used instead of $F_e(x)$ and $k(x)$ because both the functions are dependednt on distance as well as time.

$F_e(x,t)$ should be replaced with the right hand side of the equation (24) i.e.

$$
F_e(x,t) = \frac{C_0}{d_0} \cdot V_{dc} \left(\frac{1}{2} \cdot \frac{V_{ac}^2}{V_{dc}} \cdot \sin \omega t^2 + V_{ac} \cdot \sin \omega t \right)
$$

k(x,t) should be replaced with the entire modified expression for stiffness function $K_e(x,t)$ found in equation (25)

$$
k(x,t) = K_e(x,t)
$$

APPENDIX B

MATHCAD CODE FOR THE NUMERICAL MODEL OF THE
CLAMPED-CLAMPED RESONATOR CIRCUIT

Numerical Model of the Clamped-Clamped Resonator Circuit (without loop)

$k0 := 1.505 \cdot 10^3$

$k1 := 2 \cdot 10^3$

$k2 := -8.0 \cdot 10^{15}$

$k3 := 1 \cdot 10^3$

$k4 := 1.1 \cdot 10^{30}$

$c0 := 0.185 \cdot 10^{-15}$

$d_0 := 0.330 \cdot 10^{-6}$

$m1 := 2.273 \cdot 10^{-13}$

$b := 3.083 \cdot 10^{-9}$

$Q := 1000 \cdot 10^3$

$c0 \cdot d_0 = 61.0500000000000 \times 10^{-24}$

$b = 0.000000003083$

$V\_dc := 5$

$V\_ac := 0.001$

$f := 12.5 \cdot 10^6$

$T0 := 1 \cdot 10^{-4}$

$\omega := 2 \cdot \pi \cdot f$ $\omega = 7.854 \times 10^7$

$t := 0$

Units Used:
k0 = N/m
k1 = N/m^2
k2 = N/m^3
k3 = N/m^4
k4 = N/m^5
c0 = F
d0 = m
b = Ns/m
m1 = kg
f = Hz
Q = unitless
V_dc = V
V_ac = V
R1 = ohm (not used here)
R2 = ohm

Negative sign of k2 indicates softening stiffness behavior
Positive sign of k4 indicates the hardening stiffness behavior.
In the original model k1 and k3 were ignored and assumed as zero because mechanical stiffness function k(x) is symmetric around x =0

N is kg*m/s^2
Did not change this unit here.

Not really using this quality factor Q in this model unless we find the motional resitsance Rm!

In this case, to ensure prominant resosnant frequency, the dc bias voltage must be between 0 and 30V, and ac bias voltage between 0 and 500 mV.
Note: The code will not run for zero bias voltages.

$$z0(t) := \left[2 \cdot \frac{c0}{\left(d_0\right)^2} \cdot \left[V\_dc^2 + V\_dc \cdot V\_ac \cdot \sin(\omega \cdot t) + \left(\frac{1}{2}\right) \cdot V\_ac^2 \cdot \sin(\omega \cdot t)^2 \right] \right]$$

$$z0(t) = 0.085$$

$$ke1(t) := k0 - z0(t)$$

$$ke1(t) = 1.505 \times 10^3$$

$$z1(t) := \left[3 \cdot \frac{c0}{\left(d_0\right)^3} \cdot \left[V\_dc \cdot V\_ac \cdot \sin(\omega \cdot t) + \left(\frac{1}{2}\right) \cdot V\_ac^2 \cdot \sin(\omega \cdot t)^2 \right] \right]$$

$$z1(t) = 0$$

$$ke2(t) := k1 - z1(t)$$

$$ke2(t) = 2 \times 10^3$$

$$z2(t) := \left[4 \cdot \frac{c0}{\left(d_0\right)^4} \cdot \left[V\_dc^2 + V\_dc \cdot V\_ac \cdot \sin(\omega \cdot t) + \left(\frac{1}{2}\right) \cdot V\_ac^2 \cdot \sin(\omega \cdot t)^2 \right] \right]$$

$$ke3(t) := k2 - z2(t)$$

$$ke3(t) = -8.002 \times 10^{15}$$

$$z3(t) := \left[5 \cdot \frac{c0}{\left(d_0\right)^5} \cdot \left[V\_dc \cdot V\_ac \cdot \sin(\omega \cdot t) + \left(\frac{1}{2}\right) \cdot V\_ac^2 \cdot \sin(\omega \cdot t)^2 \right] \right]$$

$$ke4(t) := k3 - z3(t)$$

$$z4(t) := \left[6 \cdot \frac{c0}{\left(d_0\right)^6} \cdot \left[V\_dc^2 + V\_dc \cdot V\_ac \cdot \sin(\omega \cdot t) + \left(\frac{1}{2}\right) \cdot V\_ac^2 \cdot \sin(\omega \cdot t)^2 \right] \right]$$

$$ke5(t) := k4 - z4(t)$$

$$x := 0$$

$$k(x, t) := ke1(t) + ke2(t) \cdot x + ke3(t) \cdot x^2 + ke4(t) \cdot x^3 + ke5(t) \cdot x^4$$

$$V\_rhs1(t) := V\_ac \cdot \sin(\omega \cdot t)$$

$$V\_rhs2(t) := \left(\frac{1}{2}\right) \cdot \frac{V\_ac^2}{V\_dc} \cdot \sin(\omega \cdot t)^2 \qquad V\_rhs2(t) = 0$$

$$V\_rhs(t) := V\_rhs1(t) + V\_rhs2(t) \qquad V\_rhs(t) = 0$$

$$\eta := \frac{c0}{d_0} \cdot V\_dc \qquad\qquad \eta = 2.803 \times 10^{-9}$$

$R2 := 50 \cdot 10^6$

$V1(t) := V\_dc + V\_ac \cdot \sin(2 \cdot \pi \cdot f \cdot t)$

$V2 := V\_dc$

$p := \begin{pmatrix} 0 \\ 0 \\ 0 \end{pmatrix}$

Here, p0 = displacement
p1 = velocity
p2 = current

$$Z(t, p) := \begin{bmatrix} p_1 \\ \dfrac{1}{m1} \cdot \left(-b \cdot p_1 - k(p_0, t) \cdot p_0 + \eta \cdot V\_rhs(t) \right) \\ \dfrac{1}{R2} \cdot \left[\omega \cdot V\_ac \cdot \cos(\omega \cdot t) - \dfrac{(V\_dc + V\_ac \cdot \sin(\omega \cdot t) - R2 \cdot p_2) \cdot p_1}{d_0 + p_0} - \dfrac{d_0 + p_0}{c0 \cdot d_0} \cdot p_2 \right] \end{bmatrix}$$

$B := \text{rkfixed}\left(p, 0, T0, 2^{17}, Z\right)$

$B =$

	0	1	2	3
0	0	0	0	0
1	7.629·10-10	0	2.817·10-10	1.15·10-12
2	1.526·10-9	0	1.125·10-9	2.204·10-12
3	2.289·10-9	0	2.523·10-9	3.167·10-12
4	3.052·10-9	0	4.465·10-9	4.041·10-12
5	3.815·10-9	0	6.938·10-9	4.829·10-12
6	4.578·10-9	0	9.923·10-9	5.535·10-12
7	5.341·10-9	0	1.34·10-8	6.161·10-12
8	6.104·10-9	0	1.733·10-8	6.709·10-12
9	6.866·10-9	0	2.17·10-8	7.182·10-12
10	7.629·10-9	0	2.647·10-8	7.582·10-12
11	8.392·10-9	0	3.16·10-8	7.911·10-12
12	9.155·10-9	0	3.706·10-8	8.172·10-12
13	9.918·10-9	0	4.28·10-8	8.367·10-12
14	1.068·10-8	0	4.877·10-8	8.498·10-12
15	1.144·10-8	0	5.493·10-8	...

$$B^{\langle 0 \rangle} =$$

	0
0	0
1	7.629·10-10
2	1.526·10-9
3	2.289·10-9
4	3.052·10-9
5	3.815·10-9
6	4.578·10-9
7	5.341·10-9
8	6.104·10-9
9	6.866·10-9
10	7.629·10-9
11	8.392·10-9
12	9.155·10-9
13	9.918·10-9
14	1.068·10-8
15	...

$$B^{\langle 1 \rangle} =$$

	0
0	0
1	0
2	0
3	0
4	0
5	0
6	0
7	0
8	0
9	0
10	0
11	0
12	0
13	0
14	0
15	...

$$B^{\langle 2 \rangle} =$$

	0
0	0
1	2.817·10-10
2	1.125·10-9
3	2.523·10-9
4	4.465·10-9
5	6.938·10-9
6	9.923·10-9
7	1.34·10-8
8	1.733·10-8
9	2.17·10-8
10	2.647·10-8
11	3.16·10-8
12	3.706·10-8
13	4.28·10-8
14	4.877·10-8
15	...

$$B^{\langle 3 \rangle} =$$

	0
0	0
1	1.15·10-12
2	2.204·10-12
3	3.167·10-12
4	4.041·10-12
5	4.829·10-12
6	5.535·10-12
7	6.161·10-12
8	6.709·10-12
9	7.182·10-12
10	7.582·10-12
11	7.911·10-12
12	8.172·10-12
13	8.367·10-12
14	8.498·10-12
15	...
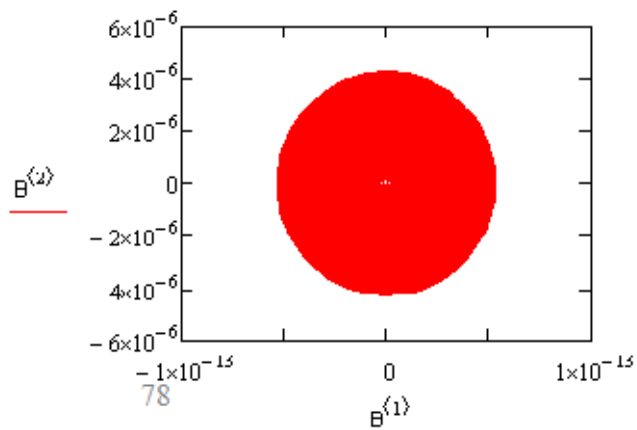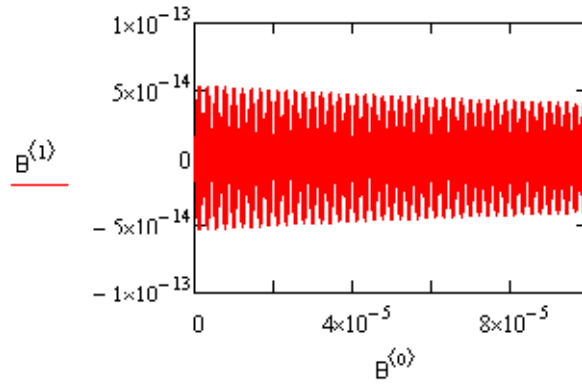
$$\text{length}\left(B^{\langle 3\rangle}\right) = 1.311\times 10^5$$

$$f = 1.25\times 10^7$$

$$v1 := \text{cfft}\left(B^{\langle 3\rangle}\right)$$

$$N0 := \text{length}(v1) \qquad N0 = 1.311\times 10^5$$

$$\Delta\omega := \frac{1}{T0} \qquad \Delta\omega = 1\times 10^4$$

$$\omega\text{max} := \Delta\omega \cdot \frac{N0}{2} \qquad \omega\text{max} = 6.554\times 10^8$$

$$f\text{max} := \omega\text{max} \qquad f\text{max} = 6.554\times 10^8$$

$$\Delta f := \Delta\omega \qquad n := 1\,..\,\frac{N0}{2}$$

$$\max\left(\left|\vec{v1}\right|\right) = 3.008\times 10^{-9}$$

Mechanical Model of the Clamped-Clamped Resonator Circuit (with loop)

$k0 := 1.505 \cdot 10^3$ $k1 := 2 \cdot 10^3$ $k2 := -8.0 \cdot 10^{15}$

$k3 := 1 \cdot 10^3$ $k4 := 1.1 \cdot 10^{30}$

$c0 := 0.185 \cdot 10^{-15}$

$d_0 := 0.330 \cdot 10^{-6}$

$c0 \cdot d_0 = 61.0500000000000 \cdot 10^{-24}$

$m1 := 2.273 \cdot 10^{-13}$

$b := 3.083 \cdot 10^{-9}$

$\qquad\qquad\qquad b = 0.000000003083$

$Q := 1000 \cdot 10^3$
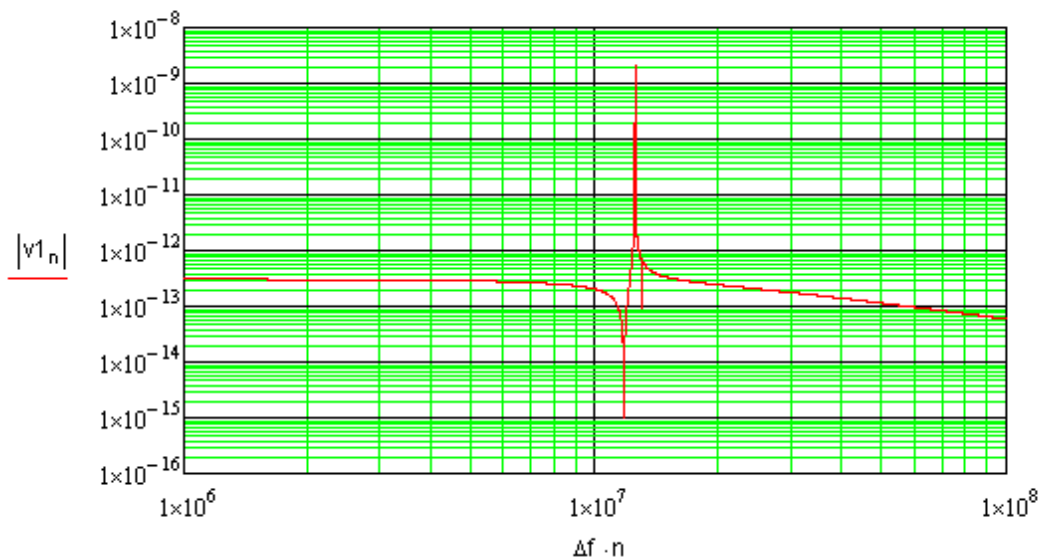
$V\_dc := 30$

$V\_ac := 0.2$

$f_r := \dfrac{1}{2 \cdot \pi} \sqrt{\dfrac{k0}{m1}}$

$\qquad\qquad f_r = 1.295 \times 10^7$

$f := 11.5 \cdot 10^6$ $T0 := 4 \cdot 10^{-4}$

$\omega := 2 \cdot \pi \cdot f$ $\omega = 7.226 \times 10^7$

$N_{pts} := 2^{17}$ $N_{pts} = 1.311 \times 10^5$

$\Delta\omega := \dfrac{1}{T0}$ $\Delta\omega = 2.5 \times 10^3$

$\omega max := \Delta\omega \cdot \dfrac{N_{pts}}{2}$ $\omega max = 1.638 \times 10^8$

$fmax := \omega max$ $fmax = 1.638 \times 10^8$

$\Delta f := \Delta\omega$

$t := 0$ $x := 0$

$f_{low} := 0.9 \cdot f_r$ $f_{high} := 1.1 \cdot f_r$ $incr := 0.001 \cdot f_r$

$\eta := \dfrac{c0}{d_0} \cdot V\_dc$ $R2 := 50 \cdot 10^6$ $V2 := V\_dc$

$\qquad\qquad \eta = 1.682 \times 10^{-8}$

Units Used:
k0 = N/m
k1 = N/m^2
k2 = N/m^3
k3 = N/m^4
k4 = N/m^5
c0 = F
d0 = m
b = Ns/m
m1 = kg
f = Hz
Q = unitless
V_dc = V
V_ac = V
R1 = ohm (not used here)
R2 = ohm

Negative sign of k2 indicates softening stiffness behavior
Positive sign of k4 indicates the hardening stiffness behavior.
In the original model k1 and k3 were ignored and assumed as zero because mechanical stiffness function k(x) is symmetric around x =0

N is kg*m/s^2
Did not change this unit here.
Not really using this quality factor Q in this model unless we find the
motional resistance Rm!

For prominant resonance, the dc bias voltage must be between 0 and 30V,
and the ac bias voltage should be between 0 and 5V
Note: The code will NOT run if the bias voltages are zero!

Here, p0 = displacement
p1 = velocity
p2 = current

$\text{result}\left(f_{low}, f_{high}, incr\right) := \Bigg|$ $s \leftarrow 0$

$\quad\Bigg|$ for $\ j \in f_{low}, f_{low} + incr \, .. \, f_{high}$

$\qquad\Bigg|\ z0(t) \leftarrow 2 \cdot \dfrac{c0}{\left(d_0\right)^2} \cdot \left[V\_dc^2 + V\_dc \cdot V\_ac \cdot \sin(2 \cdot \pi \cdot j \cdot t) + \left(\dfrac{1}{2}\right) \cdot V\_ac^2 \cdot \sin(2 \cdot \pi \cdot j \cdot t)^2\right]$

$\qquad\ ke1(t) \leftarrow k0 - z0(t)$

$\qquad\ z1(t) \leftarrow 3 \cdot \dfrac{c0}{\left(d_0\right)^3} \cdot \left[V\_dc \cdot V\_ac \cdot \sin(2 \cdot \pi \cdot j \cdot t) + \left(\dfrac{1}{2}\right) \cdot V\_ac^2 \cdot \sin(2 \cdot \pi \cdot j \cdot t)^2\right]$

$\qquad\ ke2(t) \leftarrow k1 - z1(t)$

$\qquad\ z2(t) \leftarrow 4 \cdot \dfrac{c0}{\left(d_0\right)^4} \cdot \left[V\_dc^2 + V\_dc \cdot V\_ac \cdot \sin(2 \cdot \pi \cdot j \cdot t) + \left(\dfrac{1}{2}\right) \cdot V\_ac^2 \cdot \sin(2 \cdot \pi \cdot j \cdot t)^2\right]$

$\qquad\ ke3(t) \leftarrow k2 - z2(t)$

$\qquad\ z3(t) \leftarrow 5 \cdot \dfrac{c0}{\left(d_0\right)^5} \cdot \left[V\_dc \cdot V\_ac \cdot \sin(2 \cdot \pi \cdot j \cdot t) + \left(\dfrac{1}{2}\right) \cdot V\_ac^2 \cdot \sin(2 \cdot \pi \cdot j \cdot t)^2\right]$

$\qquad\ ke4(t) \leftarrow k3 - z3(t)$

$\qquad\ z4(t) \leftarrow 6 \cdot \dfrac{c0}{\left(d_0\right)^6} \cdot \left[V\_dc^2 + V\_dc \cdot V\_ac \cdot \sin(2 \cdot \pi \cdot j \cdot t) + \left(\dfrac{1}{2}\right) \cdot V\_ac^2 \cdot \sin(2 \cdot \pi \cdot j \cdot t)^2\right]$

$\qquad\ ke5(t) \leftarrow k4 - z4(t)$

$\qquad\ k(x,t) \leftarrow ke1(t) + ke2(t) \cdot x + ke3(t) \cdot x^2 + ke4(t) \cdot x^3 + ke5(t) \cdot x^4$

$\qquad\ V\_rhs1(t) \leftarrow V\_ac \cdot \sin(2 \cdot \pi \cdot j \cdot t)$

$\qquad\ V\_rhs2(t) \leftarrow \left(\dfrac{1}{2}\right) \cdot \dfrac{V\_ac^2}{V\_dc} \cdot \sin(2 \cdot \pi \cdot j \cdot t)^2$

$\qquad\ V\_rhs(t) \leftarrow V\_rhs1(t) + V\_rhs2(t)$

$\qquad\ p \leftarrow \begin{pmatrix} 0 \\ 0 \\ 0 \end{pmatrix}$

$\qquad\ Z(t,p) \leftarrow \begin{bmatrix} p_1 \\[2mm] \dfrac{1}{m1} \cdot \left(-b \cdot p_1 - k\left(p_0, t\right) \cdot p_0 + \eta \cdot V\_rhs(t)\right) \\[2mm] \dfrac{1}{R2} \cdot \left[2\pi \cdot j \cdot V\_ac \cdot \cos(2\pi \cdot j \cdot t) - \dfrac{\left(V\_dc + V\_ac \cdot \sin(2 \cdot \pi \cdot j \cdot t) - R2 \cdot p_2\right) \cdot p_1}{d_0 + p_0} - \dfrac{d_0 + p_0}{c0 \cdot d_0} \cdot p_2\right] \end{bmatrix}$

$\qquad\ B \leftarrow \text{rkfixed}\left(p, 0, T0, N_{pts}, Z\right)$

$\qquad\ v1 \leftarrow \text{cfft}\left(B^{\langle 3 \rangle}\right)$

$\qquad\ spect_s \leftarrow 0$

$\qquad\ spect_s \leftarrow \left|\max(v1)\right|$

$\qquad\ \text{trace}\left(\text{"spect 2 \{0\} \{1\}"}, s, spect_s\right)$

$\qquad\ s \leftarrow s + 1$

$\quad\ spect$

$$y := \text{result}\left(f_{low}, f_{high}, incr\right)$$

$$n := 0, 1 .. \frac{\left(f_{high} - f_{low}\right)}{incr}$$

n =

0
1
2
3
4
5
6
7
8
9
10
11
12
13
14
...

y_n

n =
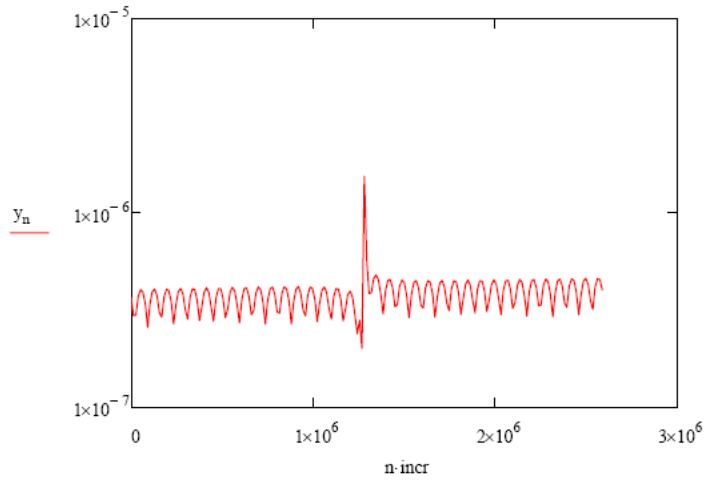
0
1
2
3
4
5
6
7
8
9
10
11
12
13
14
...

y =

	0
0	$3.672 \cdot 10^{-7}$
1	$2.973 \cdot 10^{-7}$
2	$2.989 \cdot 10^{-7}$
3	$3.731 \cdot 10^{-7}$
4	$4.039 \cdot 10^{-7}$
5	$3.924 \cdot 10^{-7}$
6	$3.406 \cdot 10^{-7}$
7	$2.584 \cdot 10^{-7}$
8	$3.412 \cdot 10^{-7}$
9	$3.936 \cdot 10^{-7}$
10	$4.056 \cdot 10^{-7}$
11	$3.75 \cdot 10^{-7}$
12	$3.075 \cdot 10^{-7}$
13	$2.916 \cdot 10^{-7}$
14	$3.709 \cdot 10^{-7}$
15	...

81

APPENDIX C

ADDITIONAL RESULTS FOR THE CURRENT AND S_{21} RESPONSE
OF THE CLAMPED-CLAMPED RESONATOR
NUMERICAL MODEL:

Table C.1 The resonant frequency and the S_{21} response with V_{ac} = 0.001 V and varying V_{dc}.

Vdc	Vac	i	f	S21
1	0.001	3.009E-09	1.24E+07	-38.226
5	0.001	3.008E-09	1.24E+07	-38.228
10	0.001	3.004E-09	1.24E+07	-38.226
20	0.001	2.989E-09	1.24E+07	-38.255
30	0.001	2.963E-09	1.24E+07	-38.226

Figure C.1 The current response with varying ac voltage when the dc bias was kept constant at 30 V.

Figure C.2 The current response with varying dc voltage when the ac bias was kept constant at 0.001V.

Table C.2 The resonant frequency and the S_{21} response with V_{ac} = 0.03V and varying V_{dc}.

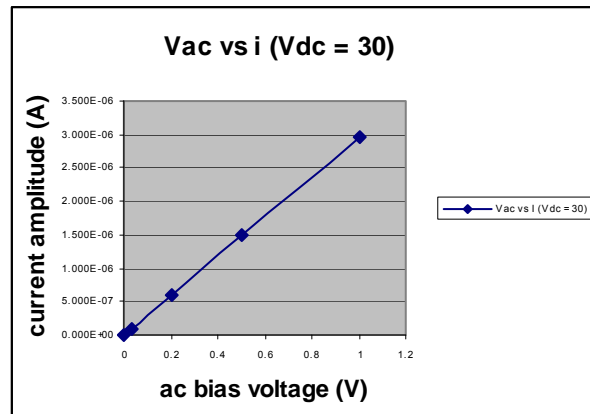| Vdc	Vac	i	f	S21
1	0.03	9.027E-08	1.24E+07	-38.226
5	0.03	9.023E-08	1.24E+07	-38.228
10	0.03	9.012E-08	1.24E+07	-38.233
20	0.03	8.967E-08	1.24E+07	-38.255
30	0.03	8.889E-08	1.24E+07	-38.293

Figure C.3 The current response with varying ac voltage when the
dc bias was kept constant at 20 V.

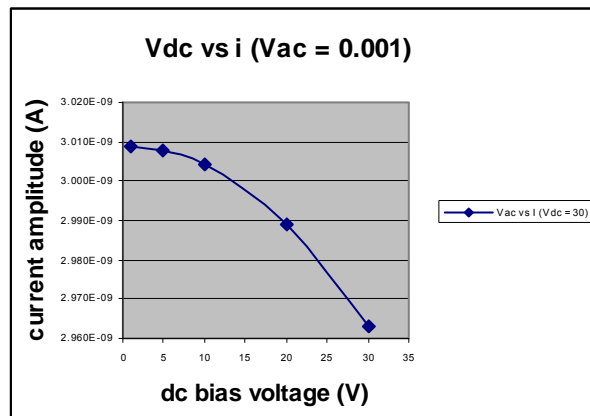

Figure C.4 The current response with varying dc voltage when the
ac bias was kept constant at 0.03V.

Table C.3 The resonant frequency and the S_{21} response with V_{ac} = 0.2V and varying V_{dc}.

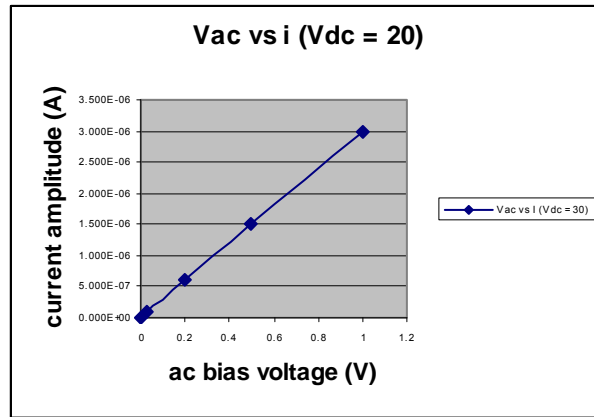| Vdc	Vac	i	f	S21
1	0.2	6.018E-07	1.24E+07	-38.226
5	0.2	6.016E-07	1.24E+07	-38.228
10	0.2	6.008E-07	1.24E+07	-38.233
20	0.2	5.978E-07	1.24E+07	-38.255
30	0.2	5.926E-07	1.24E+07	-38.293

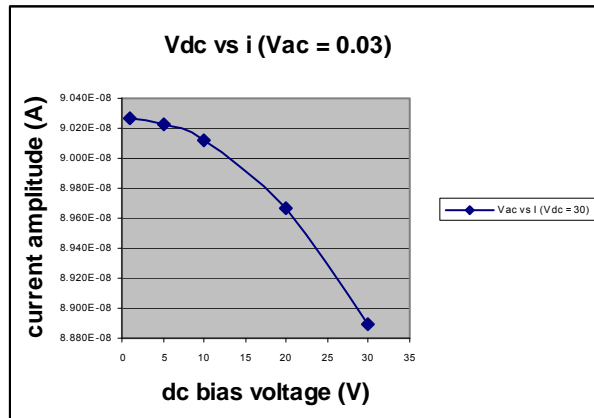Figure C.5 The current response with varying ac voltage when the dc bias was kept constant at 10 V.

Figure C.6 The current response with varying dc voltage when the ac bias was kept constant at 0.2V.

Table C.4 The resonant frequency and the S_{21} response with V_{ac} = 0.5V and varying V_{dc}.

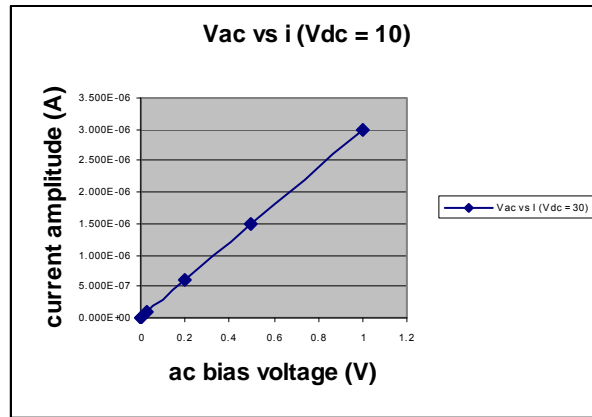| Vdc	Vac	i	f	S21
1	0.5	1.505E-06	1.24E+07	-38.225
5	0.5	1.504E-06	1.24E+07	-38.228
10	0.5	1.502E-06	1.24E+07	-38.233
20	0.5	1.494E-06	1.24E+07	-38.256
30	0.5	1.482E-06	1.24E+07	-38.292

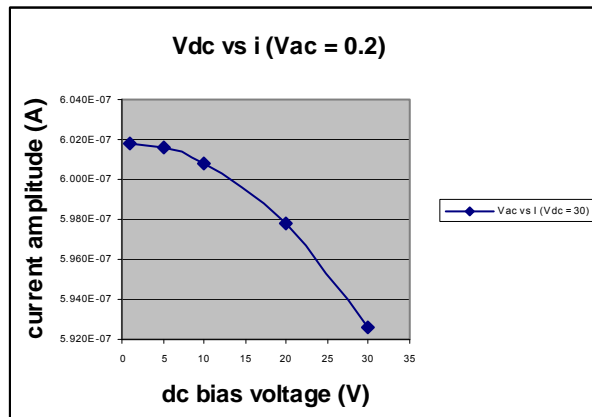Figure C.7 The current response with varying ac voltage when the dc bias was kept constant at 5 V.

Figure C.8 The current response with varying dc voltage when the ac bias was kept constant at 0.5V.

Table C.5 The resonant frequency and the S_{21} response with V_{ac} = 1 V and varying V_{dc}.

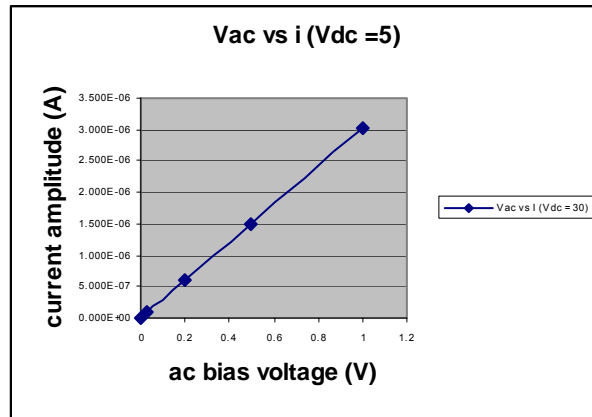| Vdc	Vac	i	f	S21
1	1	3.009E-06	1.24E+07	-38.226
5	1	3.008E-06	1.24E+07	-38.228
10	1	3.004E-06	1.24E+07	-38.233
20	1	2.989E-06	1.24E+07	-38.255
30	1	2.963E-06	1.24E+07	-38.293

Figure C.9 The current response with varying ac voltage when the
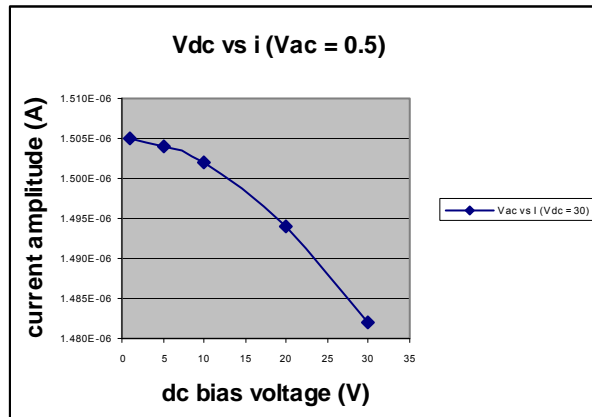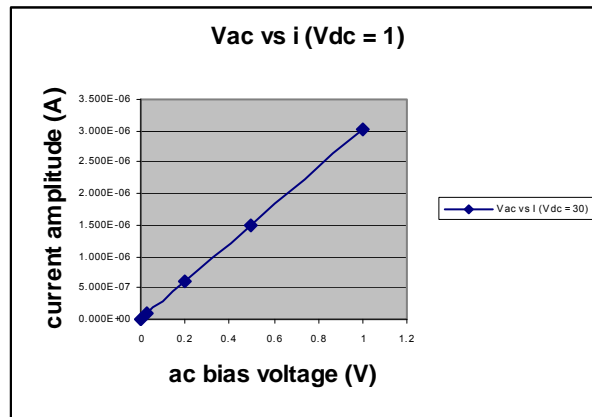dc bias was kept constant at 1 V.

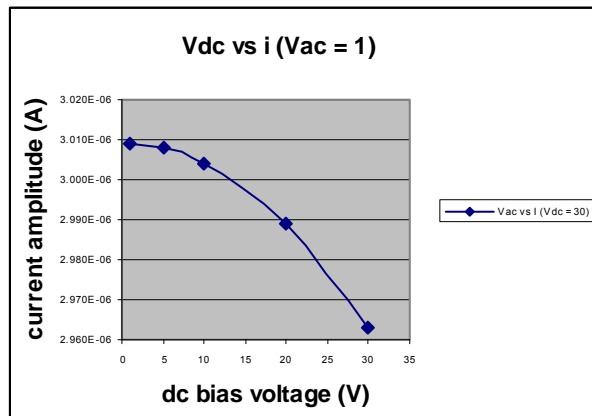Figure C.10 The current response with varying dc voltage when the
ac bias was kept constant at 1V.

REFERENCES

[1] S. Pacheco, P. Zurcher, S. Young, D. Weston and W. Dansker. "RF MEMS Resonator for CMOS Back End-Of-Line Integration", Freescale Semiconductor and Motorola, 5th Topical Meeting on Silicon Monolithic Integrated Circuits in RF Systems, 2004, pp. 203-206.

[2] V. Varadan, K. Vinoy and K. Jose, "RF MEMS and their Applications", John Wiley & Sons Ltd., Pennsylvania. West Sussex, England, 2003.

[3] H. Fujita, "Future of actuators and Microsystems", Sensors and Actuators A: Physical 56, 1996, pp. 105–111.

[4] H. Fujita, "Microactuators and Micromachines", Proceedings of the IEEE 86(8), 1998, pp. 1721–1732.

[5] W. Davis, and K. Agarwal, "Radio Frequency Circuit Design", John Wiley & Sons, Inc., 2001.

[6] L. Larson, "Microwave MEMS Technology for Next-generation Wireless Communications – invited paper", IEEE MTT-S International Symposium Digest, IEEE, Washington, DC, 1999, 1073–1076.

[7] H. Wu, K. Harsh, R. Irwin, W. Zhang, A. Michelson, and Y. Lee, "MEMS designed for tunable capacitors", IEEE MTTS Symposium Digest IEEE, Washington, DC, 1998, pp.129–130.

[8] R. Mestrom, R. Fey, J. Beck, K. Phan, and H. Nijmeijer, "Modeling the Dynamics of a MEMS resonator: Simulations and Experiments", Sensors and Actuators A 142, 2008, pp.306-315.

[9] V. Kaajakari, T. Mattila, A. Oja, and H. Seppä, "Nonlinear Limits for Single Crystal Silicon Microresonators", IEEE ASME J. Microelectromech. Syst.13, 2004, pp. 715–724.

[10] J. Bustillo, R. Howe, and R. Muller, "Surface Micromachining for Microelectromechanical Systems", Proceedings of the IEEE 86(8), 1998, pp. 1552–1574.

[11] H. Guckel, "High-aspect-ratio Micromachining via Deep X-ray Lithography", Proceedings of the IEEE 86(8), 1998, pp. 1586–1593.

[12] G. Kovacs, N. Maluf, and K. Petersen, "Bulk Micromachining of Silicon", Proceedings of the IEEE 86(8), 1998, pp. 1536–1551.

[13] H. De Los Santos, "RF MEMS Circuit Design for Wireless Communications", Artech House, Boston, MA, 2002.

[14] H. De Los Santos, "Introduction to Microelectromechanical (MEM) Microwave Systems", Artech House, Norwood, MA, 1999.

[15] E. Brown, "RF MEMS Switches for Reconfigurable Integrated Circuits", IEEE Transactions on Microwave Theory and Techniques 46, 1998, pp. 1868–1880.

[16] C. Goldsmith, S. Eshelman, and D. Dennston , "Performance of Low Loss RF MEMS Capacitive Switches", IEEE Microwave and Guided Wave Letters 8, 1998, pp. 269–271.

[17] G. Gonzalez, "Microwave Transistor Amplifiers, Analysis and Design", Englewood Cliffs, NJ: Prentice Hall, 1984.

[18] K. Gupta, R. Garg, and I. Bahl, "Microstrip Lines and Slot Lines", 2nd ed., Norwood, MA: Artech House, 1996.

[19] V. Milanovic, M. Gaitan, E. Bowen, and M. Zaghloul, "Micromachined Microwave Transmission Lines in CMOS Technology", IEEE Transactions: Microwave Theory and Techniques, Vol. 45, 1997 pp. 630-635.

[20] F. Schneider, and W. Heinrich, "Model of Thin-Film Microstrip Line for Circuit Design",. IEEE Transactions: Microwave Theory and Techniques, Vol. 49, 2001, pp. 104.110.

[21] N. Barker, and G. Rebeiz, "Distributed MEMS True-Time Delay Phase Shifters and Wide-Band Switches", IEEE Transactions: Microwave Theory and Techniques, Vol. 46, 1998, pp. 1881-1890.

[22] J. Muldavin, and G. Rebeiz, "High-Isolation CPW MEMS Shunt Switches.Part 1: Modeling",IEEE Transactions: Microwave Theory and Techniques, Vol. 48, 2000, pp. 1045-1052.

[23] T. Deng, "CAD Model for Coplanar Waveguide Synthesis". IEEE Transactions: Microwave Theory and Techniques, Vol. 44, 1996, pp. 1733 -1738.

[24] H. Krauss, C. Bostian, and F. Raab, "Solid State Radio Engineering", New York: John Wiley & Sons, 1980.

[25] W. Hayward, " Introduction to Radio Frequency Design", Englewood Cliffs, NJ: Prentice Hall, 1996.

[26] F. Ellinger, Radio Frequency Integrated Circuits and Technologies, Springer, Berlin, Germany, 2007.

[27] J. Rollett, "Stability and Power-Gain Invariants of Linear Twoports," IRE Transactions Circuit Theory, Vol. CT-9, pp. 29–32, 1962.

[28] D. Williams, "Damping of the Resonant Modes of a Rectangular Metal Package", IEEE Trans. Microwave Theory Tech., Vol. 37, 1989, pp. 253-256.

[29] P. Mezzanotte, M. Mongiardo, L. Roselli, and R. Sorrentino, "Analysis of Packaged Microwave Integrated Circuits by FDTD", IEEE Transactions: Microwave Theory and Techniques, Vol. 42, 1994, pp. 1796 -1801.

[30] S. Chaki, S. Andoh, Y. Sasaki, N. Tanino, and O. Ishihara, "Experimental Study on Spiral Inductors", 1995 IEEE MTT-S Digest, 1995, pp. 753–756.

[31] S. Ramo, J. Whinnery, and T. van Duzer, "Fields and Waves on Communication Electronics", 2nd ed., New York: John Wiley & Sons, 1984.

[32] F. Bannon III, J. Clark, and C. Nguyen, "High-Q HF Microelectromechanical Filters", IEEE Journal Solid-State Circuits, Vol. 35, 2000, pp. 512.526.

[33] K. Wang, A. Wong, and C. Nguyen, ".VHF Free-Free Beam High-Q Micromechanical Resonators,. ASME/IEEE J. Microelectromechanical Systems", Vol. 9, 2000, pp. 347-360.

[34] J. Clark, W. Hsu, and C. Nguyen, "High-Q VHF Micromechanical Contour-Mode Disk Resonators", 2000 IEEE Int. Electron Dev. Meeting, 2000, pp. 493-496.

[35] M. Stickel, G. Eleftheriades, and P. Kremer, " A High-Q Micromachined Silicon Cavity Resonator at Ka-Band,. Electron. Letter, Vol. 37, No. 7, 2001, pp. 433 - 435.

[36] C. Nguyen, "RF MEMS for Wireless Applications", Proceedings of the 60th Device Research Conference, 2002, pp. 9-12, 24-26.

[37] J.-B. Yoon, B.-K. Kim, C.-H. Han, E. Yoon, and C.-K. Kim, "Surface Micromachined Solenoid On-Si and On-Glass Inductors for RF Applications", IEEE Electron Device Letters, Vol. 20, 1999, pp. 487 – 489.

[38] A. Dec and K. Suyama, "A 1.9-GHz CMOS VCO with Micromachined Electromechanically Tunable Capacitors", IEEE Journal of Solid State Circuits, vol. 35 no. 8, 2000, pp.1231- 1237.

[39] C. Ahn, and M. Allen, "A Fully Integrated Surface Micromachined Microactuator with a Multilevel Meander Magnetic Core", IEEE Journal of Microelectromechanical Systems 2 no. 1, 1998, pp. 15–22.

[40] C. Ahn and M. Allen, "Micromachined planar inductors on silicon wafers for MEMS applications", IEEE Transactions on Industrial Electronics 45 no. 6, 1998, pp. 866–876.

[41] J. Yao, S. Park, and J. DeNatale, "High Tuning Ratio MEMS based Tunable Capacitors for RF Communications Applications", Proceedings of solid-state sensors and Actuators Workshop, IEEE, Washington, DC, 1998, pp. 124–127

[42] D. Peroulis, S. Pacheco, K. Sarabandi, and P. Katehi, "MEMS Devices for High Isolation Switching and Tunable Filtering", 2000 IEEE Int. Microwave Symposium., Phoenix, AZ, vol. 2, 2000, pp. 1217 – 1220.

[43] P. Zavracky, S. Majumdar, and N. McGruer, "Micromechanical switches fabricated using Nickel Surface Micromachining", Journal of Microelectromechanical Systems no. 1, 1997, pp. 3 – 9.

[44] J. Vig, and Arthur Ballato, "Frequency Control Devices", IEEE Transactions Ultrasonics, Ferroelectrics and Frequency Control, vol. 46 no. 6, 1999, pp.1558 – 1565.

[45] C. Nguyen, Vibrating RF MEMS for Next Generation Wireless Applications, 2004 IEEE Custom Integrated Circuits Conference, Orlando, Floria, 2004, pp. 257 – 264.

[46] K. Wang; A. Wong; and C. Nguyen, "VHF Free-free Beam High-Q Micromechanical Resonators", IEEE Journal of Microelectromechanical Systems vol. 9 no. 3, 2000, pp. 347 – 360.

[47] A. De Silva, C. Vaughan, D. Frear, L. Liu, S. Kuo, J. Foerstner, J. Drye, J. Abrokwah, H. Hughes, C. Amrine, C. Butler, S. Markgraf, H. Denton, and S. Springer, "Motorola MEMS Switch Technology for High Frequency Applications", Proceedings of the IEEE MEMS Conference, 2001, pp. 22–24.

[48] S. Young, D. Weston, B. Dauksher, D. Mancini1, S. Pacheco, P. Zurcher, and M. Miller, "A novel low temperature method to fabricate MEMS Resonators using PMGI as a Sacrificial Layer", 205th Meeting of The Electrochemical Society, 2004

[49] R. Mestrom, R. Fey, J. van Beek, K.L. Phan, and H. Nijmeijer, "Nonlinear Oscillations in MEMS Resonators", Proceedings of the Eurosensors XX Conference, Göteborg, Sweden, 2006.

[50] V. Kaajakari, T. Mattila, A. Lipsanen, and A. Oja, "Nonlinear Mechanical Effects in Silicon Longitudinal Mode Beam Resonators, Sensors and Actuators A 120, 2004, pp. 64–70.

[51] W. Weaver Jr., S. Timoshenko, and D. Young, "Vibration Problems in Engineering", 5th ed., Wiley, New York, 1990.

[52] J.Thomsen, "Vibrations and Stability; Order and Chaos", 2nd ed., McGraw-Hill Publishing Company, London, 2004.

[53] K. Kim, W. Sachse, "Nonlinear Elastic Equation of State of Solids Subjected to Uniaxial Homogeneous Loading", J. Mater. Sci. 35, 2000, pp. 3197–3205.

[54] T. Mattila, J. Kiiham¨aki, T. Lamminm¨aki, O. Jaakkola, P. Rantakari, A. Oja, H. Seppä, H. Kattelus, and I. Tittonen, " A 12MHz Micromechanical Bulk Acoustic Mode Oscillator", Sensors and Actuators A 101, 2002, pp. 1–9.

[55] J. Lopez, J. Verd, J. Teva, G. Murillo, J. Giner, F. Torres, A. Uranga, G. Abadal, and N. Barniol, "Integration of RF-MEMS Resonators on Submicrometric Commercial CMOS Technologies", Journal of Micromechanics and Microengineering, 2009.

[56] M. Demirci, and C. Nguyen, "Mechanically Corner-coupled Square Microresonator Array for Reduced Series Motional Resistance, 2006 Journal of Microelectromechanics Systems 15, 2006, pp. 1419 – 1436.

[57] E. Vittoz, M. Degrauwe, and S. Bitz, "High-performance Crystal Oscillator Circuits: Theory and Application, Journal of Solid-State Circuits 23, 1988, pp. 774–783

[58] T. Niels, S. Tonny, J. Henri, L. Rob, and E. Miko, "Stiction in Surface Micromachining, Journal of Micromechanics and Microengineering 6, 1996, pp. 385

[59] H. Nathanson, W. Newell, R. Wickstrom, and R. Davis Jr, "The Resonant Gate Transistor", IEEE Transactions of Electron.Devices 14, 1967, pp. 117–33

[60] W. Hsu, J. Clark, and C. Nguyen, "Q-optimized Lateral Free-free Beam Micromechanical Resonators", 2001 Proceedings of Transducers, 2001, pp 1110–1113.

[61] W. Hsu, and C. Nguyen, "Stiffness-compensated Temperature-insensitive Micromechanical Resonators", Proceedings of MEMS, 2002 pp 731–704

[62] W. Thomson, "Theory of Vibration with Applications", Stanley Thornes, Surrey, UK:, 1993.

[63] Nanofab, "The Facilities: The Electrical Test Station", The Nanotechnology and Research, http://www.uta.edu/engineering/nano/facilities.php

[64] M. Chitteboyina, "Integrated MEMS Microsensors", PhD. Dissertation, The University of Texas at Arlington, 2007.

[65] Freescale Semiconductor, "Heterojunction Bipolar Transistor Technology (InGaP HBT) Broadband High Linearity Amplifier Model: MMG3015NT1", Datasheet Document Rev. 1, 2008.

BIOGRAPHICAL INFORMATION

Najla Khan is a researcher in the Microsensor lab at the UT-Arlington Nanofabrication facility. She is currently completing her Master of Science in Electrical Engineering from UT Arlington. Prior to this degree, she has earned a Bachelor of Science in Computer Science and Engineering from the same university. Her diverse interests in both hardware and software fields give her a very unique blend of experience in simulation and modeling using physical and virtual components. She hopes to one day use her technical knowledge for the greater good of society, and is an active member of the Golden Key Honor Society, Institute of Electrical and Electronics Engineers (IEEE), Association for Computing Machinery (ACM), IEEE Society of Women Engineers (WIE), IEEE Communications Society and IEEE Solid State Circuits Society.